LATVIAN JOURNAL of PHYSICS and TECHNICAL SCIENCES

ISSN 0868 - 8257

4

(Vol. 54)

2017

Ind. pasūt. € 1,50 Indekss 2091
Org. € 15,00 Indekss 2092

SATURS

ENERĢĒTIKAS FIZIKĀLĀS UN TEHNISKĀS PROBLĒMAS

CIETVIELU FIZIKA

LIETIŠĶĀ FIZIKA

ELEKTRONIKA

Price to individual subscribers € 1.50/issue Index 2091
Price to collective subscribers € 15.00/issue Index 2092

CONTENTS

Индивид. заказ. Є 1,50 Индекс 2091
Орг. заказ. Є 15,00 Индекс 2092

СОДЕРЖАНИЕ

LATVIAN JOURNAL of PHYSICS and TECHNICAL SCIENCES

LATVIJAS FIZIKAS un TEHNISKO ZINĀTŅU ŽURNĀLS

ЛАТВИЙСКИЙ ФИЗИКО-ТЕХНИЧЕСКИЙ ЖУРНАЛ

Published six times a year since February 1964
Iznāk sešas reizes gadā kopš 1964. gada februāra
Выходит шесть раз в год с февраля 1964 года

4 (Vol. 54) • 2017

RĪGA

REDAKCIJAS KOLĒĢIJA

I. Oļeiņikova (galv. redaktore), A. Ozols, A. Mutule, J. Kalnačs, A. Siliņš, G. Klāvs, A. Šarakovskis, M. Rutkis, A. Kuzmins, Ē. Birks, S. Ezerniece (atbild. sekretāre)

KONSULTATĪVĀ PADOME

J. Vilemas (Lietuva), K. Švarcs (Vācija), J. Kapala (Polija), J. Melngailis (ASV), T. Jëskelainens (Somija), J. Savickis (Latvija), N. Zeltiņš (Latvija), Ā. Žīgurs (Latvija)

EDITORIAL BOARD

I. Oleinikova (Chief Editor), A. Ozols, A. Mutule, J. Kalnacs, A. Silins, G. Klavs, A. Sarakovskis, M. Rutkis, A. Kuzmins, E. Birks, S. Ezerniece (Managing Editor)

ADVISORY BOARD

Yu. Vilemas (Lithuania), K. Schwartz (Germany), J. Kapala (Poland), J. Melngailis (USA), T. Jeskelainens (Sweden), J. Savickis (Latvia), N. Zeltinsh (Latvia), A. Zigurs (Latvia)

Korektore: O. Ivanova
Maketētājs I. Begičevs

INDEKSĒTS (PUBLICĒTS) | INDEXED (PUBLISHED) IN

www.scopus.com
www.degruyter.com
EBSCO (Academic Search Complete, www.epnet.com), INSPEC (www.iee.org.com). VINITI (www.viniti.ru), Begell House Inc/ (EDC, www.edata-center.com).

Izdevējs: Fizikālās enerģētikas institūts
Reģistrācijas apliecība Nr. 0221
Redakcija: Krīvu iela 11, Rīga, LV-1006
Tel. 67551732, 67558694
e-pasts: ezerniec@edi.lv
Interneta adrese: www.fei-web.lv
Iespiests SIA “AstroPrint”

LATVIAN JOURNAL OF PHYSICS AND TECHNICAL SCIENCES
2017, N 4

DOI: 10.1515/lpts-2017-0022

PHYSICAL AND TECHNICAL ENERGY PROBLEMS

INVOLVEMENT OF INDIVIDUALS IN THE DEVELOPMENT OF TECHNICAL SOLUTIONS AND RULES OF MANAGEMENT FOR BUILDING RENOVATION PROJECTS: A CASE STUDY OF LATVIA

I.Pukite, A.Grekis, I. Geipele, N. Zeltins[1]
Riga Technical University,
Institute of Civil Engineering and Real Estate Economics,
6-210 Kalnciema Str. , Riga, LV-1048, LATVIA
E-mail: iveta.pukite@rtu.lv
[1] Institute of Physical Energetics
11 Krivu Str., Riga, LV-1006, LATVIA

In March 2016, the Latvian government approved a new support program for increasing energy efficiency in residential apartment buildings. For the support of renovation of apartment buildings in the period from 2016 to 2023, 166 470 588 EUR will be available.

Different persons, such as energy auditors, designers, architects, project managers and builders, will be involved in the process of planning, development and implementation of building renovation. At the development stage of the building renovation project, special attention should be devoted to the first stage – energy audit and technical project development. The problem arises due to the fact that each of these individuals, during the development of technical building documentation, does not work as a completely unified system.

The implementation of construction project planning and organisational management system is one of the most important factors to guarantee that the quality of building renovation project is ensured in accordance with the laws and regulatory standards.

The paper studies mutual cooperation, professionalism and the role of information feedback of personnel involved in the planning stage of building renovation, which is an essential prerequisite for the renovation process in order to achieve high quality of work and reduce the energy performance indicator.

The present research includes the analysis of different technical solutions and their impact on energy efficiency. Mutual harmonisation of technical specifications is also investigated.

Keywords: *building, energy efficiency, renovation, residential buildings, technical project*

1. INTRODUCTION

Each building has its own life cycle and it is important to extend it as long as possible. To extend the life cycle of buildings and ensure comfort of each tenant, it is necessary to provide the administered and managed property with high-quality management and maintenance services, properly organise the technical maintenance of the building, i.e., to perform daily maintenance of building elements and engineering structures as well as carry out timely renovation or rebuilding. Taking into account all the technical processes of management, the appropriate maintenance of buildings is ensured throughout their life cycle, i.e., comfort, improved safety and an opportunity to use the property according to one's own preferences and possibilities.

The administration of a residential apartment building is defined as a set of activities required for the maintenance of the residential building in order to ensure the proper operation of the building, as well as the maintenance of the land that is functionally necessary for ensuring the use of this property in accordance with the determined goal [2].

Management and maintenance of buildings are an organised and effective system of maintenance operations, which is set up to deal with problems related to the upkeep of a building [12]. By ensuring environmentally friendly maintenance and renovation of buildings, sustainable property development is implemented [14].

The renovation of residential buildings usually involves a variety of measures aiming at reducing energy and building maintenance bills, increasing safety and market value, and improving comfort and aesthetics [8].

Technical maintenance of buildings is a set of organisational and technical interrelated measures that protect the building, its elements and engineering systems from premature wear and tear, as well as ensure their use for their intended purpose throughout the entire service life.

To ensure high-quality preparation of documentation that would be a prerequisite for high-quality construction, it is required to establish close cooperation among all the parties involved. The problem arises due to the fact that each party involved does not work as a whole system when formulating recommendations and proposals to building inspection documentation.

The present article aims at exploring opportunities for cooperation among the parties involved in the renovation process in order to ensure high-quality implementation of residential building reconstruction. To achieve the aim, the following tasks are set: 1) to review the scientific literature on building design and renovation; 2) to identify the main requirements for implementation of building renovation projects using the EU Structural Funds; 3) to explore the role of mutual co-operation, professionalism of the parties involved as well as information feedback at the design stage of building renovation process; 4) to develop recommendations for the desired cooperation.

2. CONDITIONS FOR SUPPORT OF RESIDENTIAL BUILDING RENOVATION IN LATVIA

Since 2016, the active programme for renovation of residential buildings co-financed from EU Structural Funds has been launched in Latvia. Priority is given to

energy efficiency measures. The total available funding for these projects is 166.4 mln EUR. Based on the funding available, it is forecast that more than 1000 residential buildings could be renovated.

During the preparation and submission process of the energy efficiency project, it is necessary to take important decisions by the apartment owners' community and coordinate the technical documentation of the project and supplier selection with ALTUM, attract funding and agree with ALTUM on the type of aid and its amount. According to ALTUM data, as of 1 February 2017 only about 40 residential buildings received ALTUM positive opinion (approved projects) on the developed technical documentation. In turn, only 110 projects were submitted during the period from 1 August 2016 to 31 December 2016.

The main finding in this area is recognition that modernisation (renovation) of dwellings – houses – deals with juridical, social, ecological, technical – technological and economical aspects [9].

The main goal of energy efficiency measures – reduced energy consumption; energy efficiency is part of renovation processes, and one of the essential parts in this process is planning and design phases [11].

In the decision-making process, the main driving force is apartment owners. However, the administrator, who is considered to be a specialist in his field, is expected to submit professional proposals that are based on the opinions of the industry professionals and technical documentation.

Aside from technological advancements and efficiency improvements, the consumer is considered the single most important concept for understanding, managing and achieving necessary reductions and shifts in energy demand [13].

The renovation process of residential buildings is based on the three pillars: professionalism, educated owners of apartments and mutual trust. Only then it is possible to achieve good results and significantly increase the comfort of life and extend the life cycle of buildings, as well as successfully implement renovation related projects.

There is a large potential for energy savings that can be realised through energy efficiency improvement. As refurbishment offers an opportunity to take cost-effective measures and transforms them to resource efficient and environmentally sound ones, it costs much less than demolition and reconstruction [10].

Throughout this entire process, one of the most important stages is the preparation of technical documentation, i.e.:

1. Building energy certificate developed by the independent expert (energy auditor) in the field of energy performance of buildings.
2. The technical inspection report drawn up by the building specialists.
3. Development of building control estimate. Preparation of preliminary construction cost estimates based on construction volume.
4. Building design prepared by building specialists or proof of building facade, work organisation project, including protection against lightning.

Thus, it can be concluded that the development of technical documentation is one of the essential stages that further will be the basis for a successful renovation project of residential buildings.

3. DISCUSSION AND RESULTS

In Latvia, the construction of buildings is regulated by the Construction Law, the Law on the Energy Performance of Buildings as well as other regulatory documents (regulations of the Cabinet of Ministers, standards, etc.). When developing the technical documentation of building renovation, the procedures and conditions stipulated in laws and regulations are taken into account. The problem arises when each of the parties involved acts independently of each other, without mutual cooperation. On the one hand, each party complies with the regulatory requirements; on the other hand, these requirements are not always clearly defined by the legislation or processes lack mutual cooperation; as a result, technical projects do not meet the common requirements, which are necessary for the project to be accepted by the responsible body and co-financing allocated from the EU funds.

For example, developing the building design, one of the components of the technical documentation is building energy performance assessment if it is stipulated by the Law on the Energy Performance of Buildings. In turn, in compliance with these rules, if the works are implemented according to the simplified renovation procedure, the energy performance assessment is not obligatory [7]. By contrast, Article 7 of the Law on the Energy Performance of Buildings states that the energy certification of buildings shall be carried out for the designed, reconstructed or renovated building in order to be accepted into service or to be sold [Law on the Energy Performance of Buildings]. On the basis of the given laws and regulations, it can be concluded that there is no mutual compatibility between these two legal instruments. On the one hand, an assessment may not be prepared; on the other hand, the energy performance assessment shall be submitted in order to complete the construction works.

At present, the Latvian legislation does not have a unified definition of a building design. According to Article 1 of the Construction Law, a building design is an aggregate of graphic and text documents necessary for the implementation of a construction conception [4]. The definition of the term does not include “simplified renovation”. However, the General Construction Regulations provide a set of processes that are related to simplified renovation. According to the General Construction Regulations, simplified renovation is the renovation of the structure or a part thereof without affecting the loadbearing building structures, the facade of the building and common engineering and communication systems, performing functional or technical improvements [6].

The four main parties are involved in the building renovation process: the energy auditor, construction specialist, who carries out technical inspection of the building, designer and builder.

The energy auditor, preparing the calculation of energy performance of the building, gives his vision of the expected heat savings. The designer does not necessarily take into account the desired or projected heat savings if the energy auditor’s report is unavailable. Therefore, a building design may not take into account the relevant thermal indicators and one of the indicators is the heat transfer coefficient U, which is the key parameter used to determine thermal insulation of the building.

It often does not also take into account the specific thermal conductivity or lambda value (λ), which indicates the amount of heat that is conducted in unchanging conditions through the material per unit area in thickness of a unit per unit of time when there is the difference in temperature between the opposite surfaces. The specific thermal conductivity of the material is determined using EN standards. Both of these indicators, one of which (lambda) is applied to the materials, and the other U value – to the whole structure, are one of the most important energy efficiency indicators.

According to the building standards, another important survey is technical inspection of a building. Performing technical inspection of a building, experts identify and assess the technical condition of a building, its parts, as well as built-in construction products and engineering systems. Based on the technical inspection, the measures for the improvement of building condition are designed in accordance with the real situation, rather than general assumptions.

Prior to the commencement of construction, at the final stage, the building design or building facade certification card is prepared.

The most important measures to consider are as follows:

1. to describe how air permeability will be ensured in the building in accordance with the requirements of the building standards;
2. to describe the insulating material insertion technology, as well as quality and control criteria;
3. to calculate water vapour permeability of building elements for the outer structure (in accordance with requirements of the building standards);
4. to develop the detailed assembly of the following locations according to the requirements of the building standards (U-value, thermal bridges, air permeability): window connection to: window sills, side edge, upper edge; base assembly; parapet assembly; exterior wall; roof; 1st-storey floor.

In specifying the construction elements to be utilised in the building, the building design shall evaluate the thermal lag thereof, as well as select the most appropriate combination of the massive and thermal insulating layers [5].

There are a number of approaches used in the building designs by construction specialists. For example, incorporating insulation materials in the design, the following approaches are followed:

- ETAG 004 – Guideline for European Technical Approval of External Thermal Insulation Composite Systems with Rendering. ETAG 004 regulations serve as a basis.
- The personal experience, taking into account the forecasted U-value.
- The parameters envisaged in the building design by the energy auditor.
- The Construction Standard "Thermotechnics of Building Envelopes", which regulates the normative values and determines the heat transfer coefficient.
- The regulations of the Construction Standard and the calculation of energy performance, as well as it is practically evaluated what could be technically accomplished in the building in real life.

ETAG 004 system is commonly used in Latvia. This set of technical require-

ments ensures the compatibility of insulation system products and high quality of the final result (long service life, high acoustic and thermal characteristics, etc.). ETAG 004 envisages that the service life of the insulation system should be no less than 25 years.

At present, there is increasing interest in ventilated facades, which will be regulated by ETAG 034-1 "Ventilated Cladding Kits Comprising Cladding Components and Associated Fixings". However, since in Latvia these rules are not obligatory, they are being introduced on a voluntary basis. Consequently, there is little experience in the application of the system in Latvia. In order to introduce ETAG requirements, it is necessary to involve many specialists; and it is also necessary to envisage the compatibility of many materials, including screws, fasteners, etc. As a result, at present none of the companies have entered into the certification process of these provisions, the implementation of which will place the responsibility for its compliance with ETAG requirements.

Each of these approaches has its advantages and drawbacks. At present, due to different laws and regulations, often the parties adhere to the regulations relating to their operation. As can be seen in Fig. 1, the designer follows the Construction Law, while the energy auditor – the Law on the Energy Performance of Buildings. In order to achieve the desired result, during the development process of technical documentation the designer should cooperate with the energy auditor. This would ensure that the parties involved take into account the provisions of the Construction Standard, the energy auditor's calculations of thermal insulation material requirements, the designer's calculations, which are based on both the Construction Standard and practical experience, as well as aligned with the customer's wishes and possibilities.

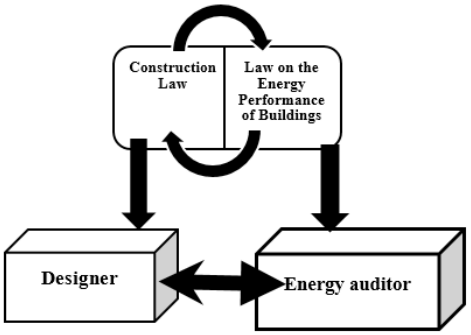

Fig. 1. Mutual cooperation and feedback between a designer and energy auditor [made by the authors].

If the designer and energy auditor do not develop mutual cooperation, problems may arise in the construction process. The constructor performs his work according to the building design, rather than the energy performance certificate. Thus, if the building design does not include, for example, lambda, the constructor ensures the necessary amount, insulation thickness according to the design, but the requirements of Latvian Construction Standard LBN 002-15 "Thermotechnics of Building Envelopes" are not met.

Within the technical documentation and renovation projects, high qualification of employees is one of the most important factors in order to make investment

in the improvement of energy efficiency and the use of renewable energy resources economically justified and achieve a decrease in energy and resource consumption and costs [1].

Assessing the residential building renovation projects, ALTUM has identified the following shortcomings:

1. Opinion on building technical inspection:

a. the building technical inspection does not provide all the necessary information according to construction standards;
b. there are no recommendations: for crack prevention or elimination, for installation of vertical and horizontal waterproofing, for building rainwater system restoration or installation;
c. there are no solutions proposed for prevention of the pre-emergency
d. separate parts of the building are not examined at all, for example, the internal engineering systems and equipment, for which the building design documentation, lightning protection system are prepared;
e. by condition of the main framework; exploring photos and reading the accompanying description, the mismatch or incomplete description of the situation is identified;
f. the natural air supply system is not examined; therefore, there are no proposals for its renovation or modernisation;
g. information differs from that in the energy audit concerning part of the building and its structure thickness;
h. the structure is assumed to be deteriorated without any justification, situation description and explanation;
i. the specialist who carries out the examination process does not have either a valid certificate or the right to carry out this type of work.

2. Assessment of building energy performance:

a. building energy certificate is not registered in the Construction Information System;
b. there is no calculation submitted, in which the rate of heat loss of building envelope is compared with the standard rate of heat loss, no calculation of projected savings submitted, which shows the air exchange in the building (which cannot be less than the air exchange before carrying out energy efficiency measures), as well as substantiates the way according to which savings are obtained, taking into account the expected air exchange after carrying out energy efficiency measures, the incoming and outgoing air t^0 and other parameters;
c. errors in heat balance calculations for heating after carrying out energy efficiency measures, inaccurate calculations of energy efficiency measures.

3. Building design or simplified renovation card:

a. the proposals specified in the technical inspection or energy performance

assessment are not taken into account, for example, wall joint crack sealing, reinforcement of masonry pilasters, installation solution of loggia glazing;

b. the proposals of building design do not comply with the findings of technical inspection, for example, the building design gives the description and drawing of the construction part for restoration, but the technical inspection does not even mention that it is necessary to develop an appropriate solution;
c. the building inspection is not carried out at the same time with the development of building design; the difference can take even 2 years;
d. to solve the existing problems, it is not enough just to involve in the project professional building specialists, energy auditors and designers. An important role is played by mutual cooperation, feedback creation. It can be stated that it is necessary to create the information reception and transmission model, within which all parties participate in the building renovation process at all its stages of development, and the wishes of the customers and their facilities are taken into account as well as the design work in accordance with the findings of the inspection.

The possible cooperation model is illustrated in Fig. 2.

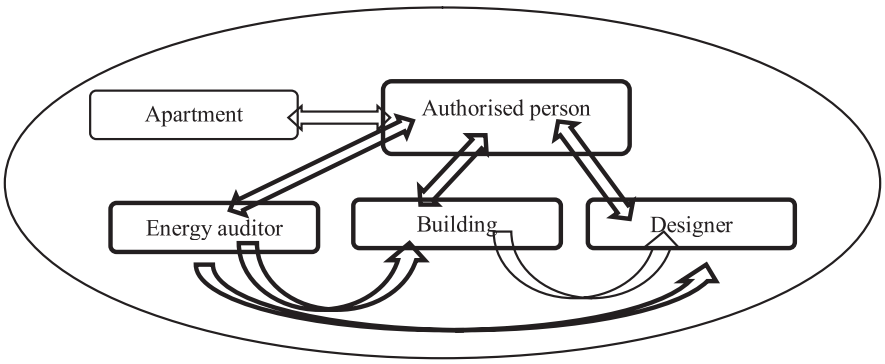

Fig. 2. Cooperation model for information sharing [made by the authors].

The model demonstrated in Fig. 2 would ensure full exchange of information. As a result, the designer would be aware of the reasons – why some of the measures are included in the energy performance report or technical inspection, as well as the solutions would be proposed. If there is no cooperation, often the building design does not include specific things that the apartment owners would be willing to include, but as they are not professionals in the field of project development, they would not notice their absence. The customers (owners or their authorised persons) are not professionals; therefore, they cannot always assess the standards, insulation thickness, U values, volumes incorporated in the projects.

As a result, the project sponsor does not approve the building design because it should be improved and, thus, time is wasted and the launch of the reconstruction works can be postponed. Each of the parties involved in the design development

system has its advantages and disadvantages.

The Positive and Negative Features of the Parties Involved in the Project Development Stage are follows:

Apartment owner. *Positive Features:* the decision has been made to restore the building; there is desire to restore the property; there is desire to listen to professionals and authorise the specialist to act on his behalf. *Negative Features:* the decision has been made to restore the building; there is desire to restore the property; there is desire to listen to professionals and authorise the specialist to act on his behalf.

Authorised person of apartment owners. *Positive Features:* there is understanding of project management; takes part in seminars organised by financial institutions on fundraising requirements: technical documentation, project application, legal questions; a vote of confidence received from the apartment owners the mandate to organise the project development and management. *Negative Features:* no technical knowledge and no professional experience.

Energy auditor. *Positive Features:* there is professional knowledge of energy efficiency issues and the certificate to work in his own industry. *Negative Features:* works only within his own competence; participates also in other projects; without extra remuneration is not motivated to participate in discussions with the customer and without specially organised initiatives does not cooperate with a building specialist and designer.

Building specialist. *Positive Features:* there is professional knowledge of technical inspection of structures and the certificate to work in his own industry. *Negative Features:* there is the certificate to work in his own industry; participates also in other projects; without extra remuneration is not motivated to participate in discussions with the customer and without specially organised initiatives does not cooperate with an energy auditor and designer.

Designer. *Positive Features:* there is professional knowledge of construction design and the certificate to work in his own industry. *Negative Features:* there is the certificate to work in his own industry: participates also in other projects; without extra remuneration is not motivated to participate in discussions with the customer and without specially organised initiatives does not cooperate with an energy auditor and building specialist.

Having examined the positive and negative features indicated in Table 2, it can be stated that the most important factor is a lack of information and cooperation. In real practice, developing the projects:

1. There are no meetings held on the drawing up of documents.
2. The specialist works as an individual rather than a single system.
3. When the project is submitted to the financial institution and the opinion on the need of adjustment is received – there are problems with communication because specialists have already been involved in other projects.
4. At the beginning of procurement, an authorised person or an apartment owner remains alone as other specialists no longer participate at this stage.

Taking into account the above-mentioned problems, it can be stated that there

is a need for a person who performs duties related to the organisation of cooperation. Such a person can be either a company that fully ensures the development and implementation stages of the project, or the project manager chosen by owners or their authorised persons.

To ensure the high-quality development of the project technical documentation, a project manager informs the parties involved about project progress, the cooperation structure, participates in training activities organised by financial institutions, uses specialised computer programs and electronic communication means to provide information, ensure feedback and documentation process, performs verification of submitted documents, completes the project application form, as well as other documents and draws up different types of administrative documents.

4. CONCLUSIONS

1. The authority, which receives the project proposals and gives the final opinion on the funding allocated, should provide technical advice to reduce the risks at the preparation and implementation stages of the energy efficiency improvement project.
2. During the building technical inspection, the customer and the designer receive information on the bearing capacity of the structure, the main thermal bridges and parts of the structure through which the greatest heat losses occur, as well as receive the recommendations on other essential works, which would extend the lifetime of the building and improve energy efficiency.
3. Due to poor cooperation, the technical documentation provides information on the building and its structure thickness that differs from that in the technical inspection and energy audit report. Consequently, the building design includes the measures which do not comply with the findings indicated in the inspection; or, on the contrary, the building design does not include measures prescribed by the building specialist or energy auditor.
4. High quality building inspection improves the development of technical solutions in the building design and reduces the chances that during the project there will be unexpected expenses (non-eligible costs).
5. To ensure the development of technical documentation according to customer preferences and in compliance with regulatory framework, it is necessary to choose an authorised person, who ensures project management and monitors the implementation of all project development stages. The key to successful project management is a specialist – project manager who has the technical knowledge, the ability to make economically justified calculations, as well as experience in building renovation management.

REFERENCES

1. Geipele, S., & Auzins, A. (2015). The development of housing sector and residential real estate market after economic recession in Latvia. *Baltic Journal of Real Estate Econom-*

ics and Construction Management, 3, 103–119. ISSN (Online) 2255-9671. DOI: https://doi.org/10.1515/bjreecm-2015-0011

2. Geipele, S., Geipele, I., Slava, D., & Stamure, I. (2012). Social, economic and legal problems of housing management in Latvia. In 7th International Scientific Conference on Business and Management-2012, 10–11 May 2012 (pp. 631–638). Lithuania, Vilnius. ISSN 2029-4441 print / ISSN 2029-929X online. DOI: 10.3846/bm.2012.082
3. Legislation of the Republic of Latvia. (2016). Darbības programmas "Izaugsme un nodarbinātība" 4.2.1. specifiskā atbalsta mērķa "Veicināt energoefektivitātes paaugstināšanu valsts un dzīvojamās ēkās" īstenošanas noteikumi [Implementing rule of the Operational Programme "Growth and Employment" 4.2.1. the specific objective of the support "Promote energy efficiency investments in the public and residential buildings"]. Retrieved 8 November 2016, from http://likumi.lv/ta/id/281323-darbibas-programmas-izaugsme-un-nodarbinatiba-4-2-1-specifiska-atbalsta-merka-veicinat-energoefektivitates-paaugstinasanu
4. Legislation of the Republic of Latvia. (2013). Būvniecības likums. [Construction Law]. Retrieved 10 March 2017, from https://likumi.lv/doc.php?id=258572
5. Legislation of the Republic of Latvia. (2015). Ministru kabineta noteikumi Nr.339 Latvijas būvnormatīva LBN 002-15 "Ēku norobežojošo konstrukciju siltumtehnika". [Regulations regarding Latvian Construction Standard LBN 002-15 "Thermotechnics of Building Envelopes"]. Retrieved 10 March 2017, from https://likumi.lv/ta/id/275015-noteikumi-par-latvijas-buvnormativu-lbn-002-15-eku-norobezojoso-konstrukciju-siltumtehnika
6. Legislation of the Republic of Latvia. (2014). Ministru kabineta noteikumi Nr.529 Ēku būvnoteikumi. [General Construction Regulations]. Retrieved 5 March 2017, from https://likumi.lv/doc.php?id=269164
7. Legislation of the Republic of Latvia. (2013). Ēku energoefektivitātes likums [Law on the Energy Performance of Buildings]. Retrieved 15 March 2017, from https://likumi.lv/doc.php?id=253635
8. Martinaitis, V., Kazakevičius, E., & Vitkauskas, A. (2005). A two-factor method for appraising building renovation building and energy efficiency improvement projects. *Energy Policy, 35*(1). 192–201. ISSN: 0301-4215. DOI: http://doi.org/10.1016/j.enpol.2005.11.003
9. Miniotaite, R. (2015). Rational solutions for the modernization of apartment houses. In 8th International Structural Engineering and Construction Conference: Implementing Innovative Ideas in Structural Engineering and Project Management, ISEC 2015, 23–28 November 2015. Sydney, Australia. Code 118317.
10. Ouyang, J., & Hoakao, K. (2011). Establishment of the methodology to guide energy – Efficiency renovation of existing residential buildings in China. In International Conference on Computer Distributed Control and Intelligent Environmental Monitoring, 19 – 20 February 2011 (pp. 2203–2210). DOI: http://dx.doi.org/10.1016/j.enbuild.2011.05.005
11. Palm, J., & Reindl, K. (2016). Understanding energy efficiency in Swedish residential building renovation: A practice theory approach. *Energy Research & Social Science, 11*, 247–255. ISSN: 2214-6296. DOI: http://doi.org/10.1016/j.erss.2015.11.006
12. Puķīte, I., & Geipele, I. (2017). Different approaches to building management and maintenance meaning explanation. *Procedia Engineering, 172*, 905–912. ISSN 1877-7058. DOI: https://doi.org/10.1016/j.proeng.2017.02.099
13. Strengers, Y., Nicholls, L., & Maller, C. (2016). Curious energy consumers: Humans and nonhumans in assemblages of household practice. *Journal of Consumer Culture, 16*(3), 761–780. DOI: 10.1177/1469540514536194

14. Štaube, T., Leemeijer, B., Geipele, S., Kauškale, L., Geipele, I., & Jansen, J. (2016). Economic and financial rationale for age-friendly housing. *Journal of Financial Management of Property and Construction*, *21*(2), 99–121. ISSN 1366-4387. DOI: http://dx.doi.org/10.1108/JFMPC-05-2015-0015

TEHNISKO RISINĀJUMU IZSTRĀDĒ IESAISTĪTĀS PERSONAS UN RISINĀŠANAS PRINCIPU VADĪBA ĒKU ATJAUNOŠANAS PROJEKTOS: LATVIJAS PIEREDZE

I.Puķīte, A.Greķis, I.Geipele, N.Zeltiņš

K o p s a v i l k u m s

Ēku atjaunošanas procesa plānošanā, attīstībā un īstenošanā ir iesaistītas dažāda tipa personas, energoauditori, projektētāji, arhitekti, projektu vadītāji un būvnieki. Piedaloties ēku atjaunošanas projekta attīstības posmā, liela vērība jāveltī tās pirmajai stadijai, – energoauditam un tehniskā projekta izstrādei. Problēma rodas apstākli, ka katra no šīm personām, izstrādājot ēku tehniskās risināšanas dokumentāciju, nedarbojas kā vienota vesela sistēma.

Būvniecības projektu plānošanas, īstenošanas un pārvaldības organizatoriskās sistēmas ieviešana ir viens no būtiskiem faktoriem, lai ēku atjaunošanas projektu kvalitāte tiktu nodrošināta atbilstoši tiesību aktu un standartu regulējumam.

Rakstā tiek pētīta ēku atjaunošanas projektēšanas stadijā iesaistīto pušu savstarpējās sadarbības, profesionalitātes un informācijas atgriezeniskās saites loma, kas ir būtisks priekšnoteikums, lai atjaunošanas procesa gaitā tiktu sasniegta augsta darbu kvalitāte un plānotais samazinātais energoefektivitātes rādītājs. Izmantojot kvalitatīvās metodes, tiek veikta problēmas analīze, kas raksturīga dzīvojamo ēku atjaunošanas projektu izstrādes laikā, kā arī tiek meklēts risinājums šo tehnisko projektu kvalitatīvai attīstībai.

06.06.2017.

LATVIAN JOURNAL OF PHYSICS AND TECHNICAL SCIENCES
2017, N 4

DOI: 10.1515/lpts-2017-0023

DIGITAL CONTROL SYSTEM OF TWO-MOTOR AC ELECTRICAL DRIVE BUILT BY PRINCIPLES OF HARLAND

J.N. Dochviri, G.R. Turmanidze
Georgian Technical University, Tbilisi (Georgia)
E-mail:jumber_dochviri@yahoo.com

In the paper, optimization of scalar control system of two-motor electrical ac drive with individual regulators of speed is investigated. Structural scheme of the drive is constructed via electromagnetic process agreement taking into account elasticitic shaft. The expressions for the optimal parameters of digital regulators for stator currents of the motors and speed of the drive are given. Modelling results obtained on the computer are given. The considered system of ac drive provides optimal dynamic character as well as automatic distribution of loading between the motors.

Key words: *digital control, optimisation of dynamics, proportional distribution of loading two-motor ac electrical drive.*

1.INTRODUCTION

Recently, due to the well-known advantages of an ac motor in comparison with a dc motor in the practice of drives, it is topical to use a frequency-controlled asynchronous electric drive. However, on large precision-controlled technological machines, including paper-making machines, thyristor dc electric drives are still mainly used devices, as they are simpler and more reliable [1], [2]. Frequency, i.e. vector controlled ac drives on these machines (as on other powerful machines) are seldom used since they are a too complex and more unreliable control system [3], [4]. Presses of mechanisms of the paper-making machines have large inertial masses and action with a constant static moment ($M_{ST} = const$); therefore, it is possible for them to use a frequency controllable electric drive with a simplified two-circuit (from the speed and the current) scalar control system. This is acceptable due to $U/f = const$, i.e. when, the induction motor works with a constant magnetic flux ($\Phi = const$) and a constant torque ($M = const$).

Moreover, it is known that modern presses of paper machines on each working shaft have individual electric motors. Therefore, for these mechanisms we will investigate in the paper the following simplified control system given in Fig. 1.

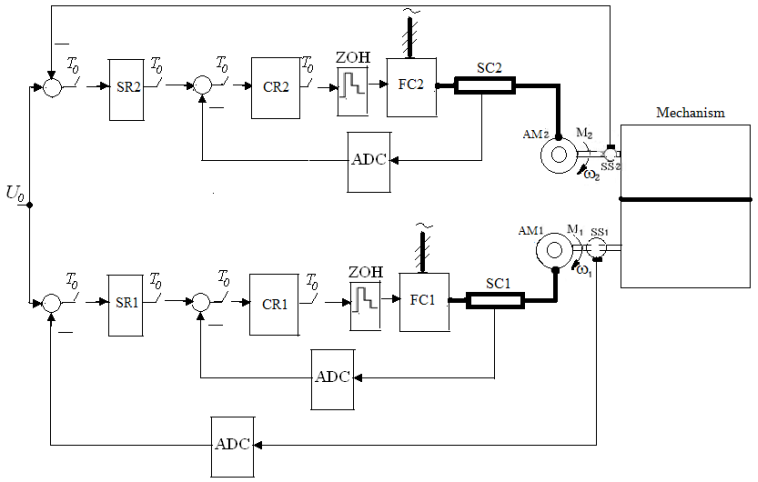

Fig.1. Functional scheme of a two-motor frequency control drive.

In Fig. 1 the following notations are used: U_0 is input signal; SR1, SR2, CR1 and CR2 are digital regulators of speed and stator currents of the motors; FC1 and FC2 are converters of frequency; AM1 and AM2 are three-phase asynchronous electric motors; ZOH is zero order holds; ADC denote analog-to-digital converter of signals; SS1 and SS2 are sensors of speeds of electric motors; CT1 and CT2 are sensors of stator currents of the motors; T_0 denotes sampling time of signals.

2. EQUATIONS OF DYNAMICS OF THE DRIVE

To study the dynamic properties of the introduced system of electric drive and to build its structural scheme, we consider equations of movement of the motors in the well-established form of relative increments of variables:

$$K_{AM.i}\Delta f^* - \frac{\Delta\nu_i}{\delta_{B.i}} - \Delta\mu_{Ei} = T_i \frac{d(\Delta\nu_i)}{dt}, i = 1;2 \qquad (1)$$

where: $\Delta f^* = \frac{\Delta f}{f_B}, \Delta\mu_{Ei} = \frac{\Delta M_{E.i}}{M_{ST.iB}}, \Delta\nu_i = \frac{\Delta\omega_i}{\omega_B}$ are relative increments of variables of frequency of the input voltages of the motors, of elastic moments of the shafts and of angle speed of the motors; $K_{AM.i} = (1+\delta_{B.i})/\delta_{B.i}$ are coefficients of the transducers of the motors; $\delta_{B.i} = \Delta\omega_{B.i}/\omega_B$ are relative speed drops of the motors; $\Delta\omega_{B.i} = M_{ST.B.i} \cdot r'_{2.i} / c^2_{AM.i}; c_{AMi} = U_{NOM}/\omega_{0NOM}; c_{AMi} = U_{NOM}/\omega_{0NOM}; T_i = J_i\omega_B / M_{ST.B.i}$ are mechanical time constants of the motors.

$U/f = const$, we have $\Delta f^* = \Delta\upsilon$, where $\Delta\upsilon = \frac{\Delta U}{U_B}$ are relative increments of stator voltages. Then equation (1) for the first motor can be written as follows:

$$K_{AM.1} \cdot \Delta\upsilon_1 - \frac{\Delta\nu_1}{\delta_{B\,1}} - \Delta\mu_{E.1} = T_1 \cdot \frac{d(\Delta\nu_1)}{dt}, \tag{2}$$

Similarly to equation (2), it is possible to write its movement for the second motor:

$$K_{AM.2} \cdot \Delta\upsilon - \frac{\Delta\nu_2}{\delta_{B.2}} - \Delta\mu_{E.2} = T_2 \frac{d(\Delta\nu_2)}{dt}. \tag{3}$$

The equation of movement of the press mechanism of the paper-making machine will have the following form:

$$\sum_{i=1}^{2} K_{Li}\Delta\mu_{Ei} - \Delta\mu_{ST} = T_M \cdot \frac{d\Delta\nu_M}{dt}, \tag{4}$$

where $K_{L1} = \frac{M_{ST1}}{M_{ST}}$, $K_{L2} = \frac{M_{ST2}}{M_{ST}}$ are coefficients of the loadings of the motors; $T_M = J_M \omega_B / M_{ST}$ is mechanical time constant of the mechanism.

If we take into consideration electromagnetic transient processes in the power electrical parts of the system (FC1-AM1 and FC2-AM2) with equivalent electromagnetic time constants $T_{E.i} = (\omega_0 \cdot s_{k.i})^{-1}, i = 1;2$, also with time constants of the control systems FC1 and FC2 ($T_{FC.i}, i = 1;2$), then the system of differential equations of the whole power electromechanical part of the drive in relative increments of variables will have the following form:

$$\begin{cases} \Delta\mu_i - \Delta\mu_{Ei}\dfrac{d(\Delta\nu_1)}{dt} = \dfrac{1}{T_i} \cdot \dfrac{d(\Delta\nu_i)}{dt}, \Delta\mu_i = K_{AM.i}\Delta\upsilon_i - \dfrac{\Delta\nu_i}{\delta_{B.i}}; \\ \sum\limits_{i=1}^{2} K_{L.i}\Delta\mu_{E.i} - \Delta\mu_{ST} = \dfrac{1}{T_M} \cdot \dfrac{d(\Delta\nu_M)}{dt}; \\ \Delta\mu_{Ei} = \dfrac{1}{T_{ci}} \cdot \int (\Delta\nu_i - \Delta\nu_M)dt + \dfrac{T_{di}}{T_{ci}} \cdot (\Delta\nu_i - \Delta\nu_M); \\ T_{Ei}\dfrac{d\Delta\mu_i^{'}}{dt} + \Delta\mu_i^{'} = K_{AM.i} \cdot \Delta\upsilon_i; \\ T_{FC.i}\dfrac{d\Delta\upsilon_i}{dt} + \Delta\upsilon_i = K_{FC.i} \cdot \Delta\upsilon_{CR.i}, i = 1;2 \end{cases} \tag{5}$$

where $\Delta\mu_i', \Delta\nu_M, \Delta\upsilon_{CR}$ are relative increments of the moment torque, angular speed of mechanism and output voltage of current regulator (CR); T_{di} and T_{ci} are time constants characterising elasticity and viscosity of mechanical transmission [3]; $K_{FC.i} = K_{FC.i}^{'} \cdot \alpha_{FC}$, $i = 1;2$ are transmission coefficients of frequency converters

by representation in the form of relative increments; $K'_{FC.i} = \Delta E_{FC.B.i} / \Delta U_{CR.B.i}$ are coefficients of transmission of frequency converters; $\alpha_{FC}=U_{0.B}/E_{FCB}$ is matching coefficient by the representation of equations in the form of relative increments.

Using operational form for the systems of differential equations (5) we can build a detailed structural scheme of the drive (see Fig. 2).

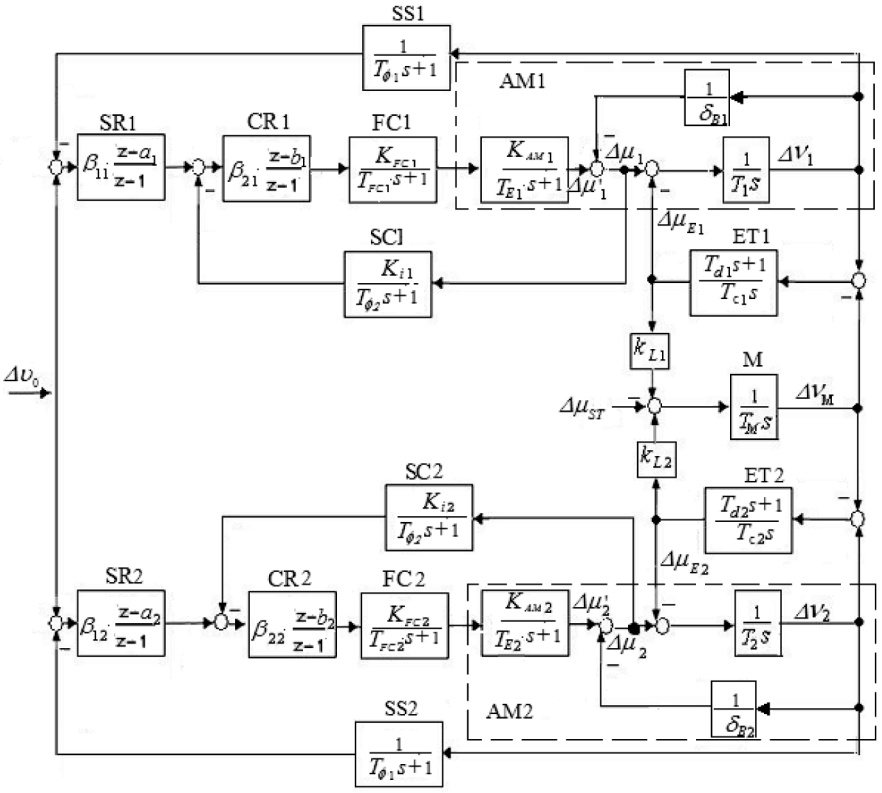

Fig.2. Structural scheme of the two-motor asynchronous electric drive.

In Fig. 2 the following notations are used: dynamic gains β_{11}, β_{12}, β_{21}, β_{22} and constants (a_1, a_2 and b_1, b_2) of the controllers, which depend on T_{Ei}, T_1, T_2, T_M and T_0; $T_{\phi 1}$ and $T_{\phi 2}$ are time constants of filters after sensors of the speed and currents; $K_{iq} = K_{iq}' \cdot \alpha_q$ are coefficients of transition of current sensors; $K_{iq}' = U_{SC.,q.B} / I_{AM.,q.B}$; $\alpha_q = I_{AM.,q.B} / U_{0.B}$, $q = 1;2$.

In this scheme transfer functions of digital controllers (PI-type) are written via z-operators, where $z = 1 + T_0 \cdot s$ and $s = d / dt$ denote Laplace operator.

3. OPTIMISATION AND MODELLING OF THE SYSTEM

To study characteristics of the system under consideration, the computer model was examined in the Matlab source (see Fig. 3). The following numerical values of the scheme are used: $T_{E1} = 0.1$, sec.; $T_{\phi 1} = 0.002$, sec.; $K_{FC1} = 10$; $T_{FC1} = 0.01$, sec.; $T_{E2} = 0.07$, sec. ; $T_{\phi 2} = 0.02$, sec.; $K_{FC2} = 10$; $T_{FC2} = 0.01$, sec. ; $T_M = 10$, sec.

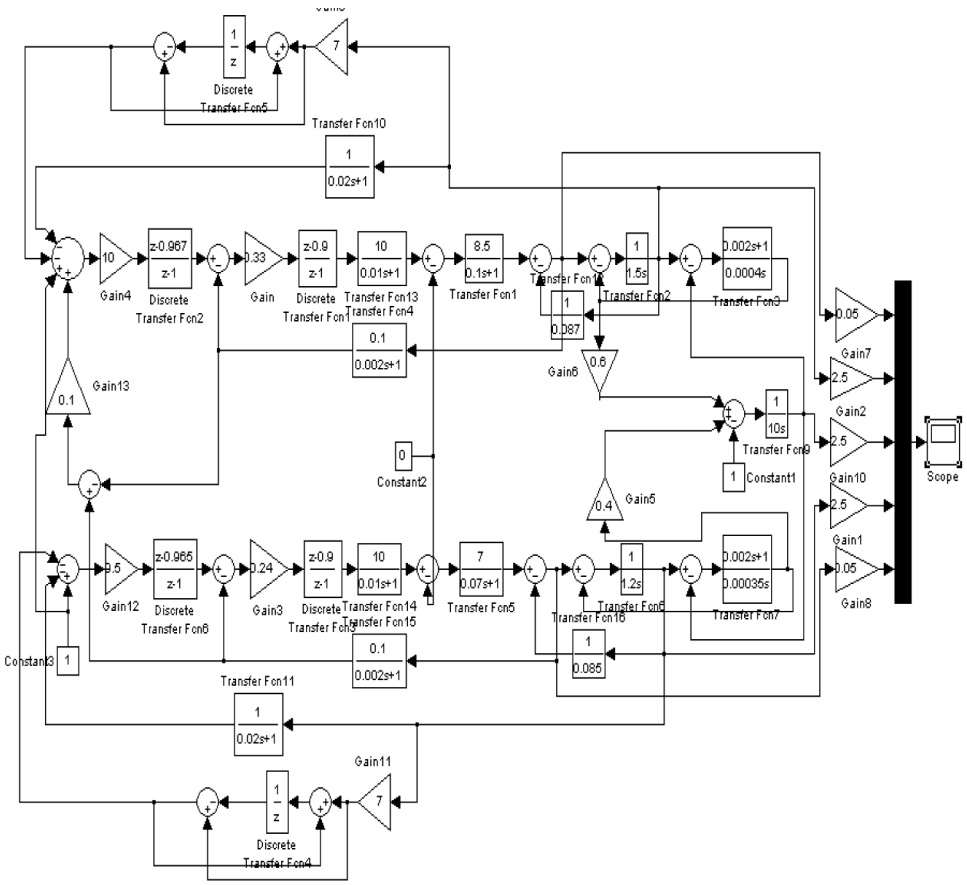

Fig.3. Computer scheme of two-motor frequency electric drive.

In the process of computer simulations of the drive system (Fig. 3) it has been established that in the current circuits ($\Delta\iota_i = \Delta\mu_i, i = 1;2$) influence of internal feedbacks of the motors through coefficients 1/0.087 and 1/0.085 from the speed ($\Delta\nu_1$ and $\Delta\nu_2$) is negligible.

Consequently, tuning of regulators (CR1 and CR2) can be done due to conditions of "module optima" [2], [3]. In this case, parameters of CR1 were obtained according to the formulas:

$$\beta_{21} = \frac{T_{E1}}{2 \cdot k_{i1} \cdot k_{FC1} \cdot k_{AM1} \cdot T_{\Sigma 2}}; \quad \tau_{21} = T_{E1}, \tag{6}$$

where $T_{\Sigma 2} = T_{FC1} + T_{\phi 2} = 0.012$, sec.; $\beta_{21} = 0.24$; $\tau_{21} = 0.1$, sec. In the digital performance of regulator CR1 we should present its transfer function in the z-transformed form ($z = 1 + T_0 \cdot s$, [5], [6]), i.e., as follows:

$$W_{CR1}(z) = \beta_{21} \cdot \frac{z - b_1}{z - 1} = 0.24 \cdot \frac{z - 0.9}{z - 1}. \tag{7}$$

Similarly to CR1, we can find parameters of CR2:

$$\beta_{22} = 0.24; b_2 = 0.9\,. \tag{8}$$

Tuning of speed regulators (SR1 and SR2) can be done according to "Symmetric Optima", we have:

$$\beta_{11} = \frac{k_{i1} \cdot (T_1 + T_2)}{3.5 \cdot T_{\Sigma 1}};\ \ \tau_{11} = 10 \cdot T_{\Sigma 1}\,, \tag{9}$$

where $T_{\Sigma 1} = T_{\phi 1} + T_{\Sigma 2} = 0.02 + 0.012 = 0.032$ sec. As a result of calculations, we obtain: $\beta_{11} = 10;\ \tau_{11} = 0.3$ sec. In the digital performance of regulator SR1, its transfer function will have the following form:

$$W_{SR1}(z) = \beta_{11} \cdot \frac{z - a_1}{z - 1} = 10 \cdot \frac{z - 0.967}{z - 1}\,. \tag{10}$$

Similarly, we obtain parameters of SR2: $\beta_{12} = 9.5;\ a_2 = 0.965.$

Investigations of dynamics on the computer showed that without the introduction of flexible feedbacks on the speed of the motors to the inputs SR1 and SR2, the transient processes were unacceptably strongly oscillating (corresponding curves are not given).

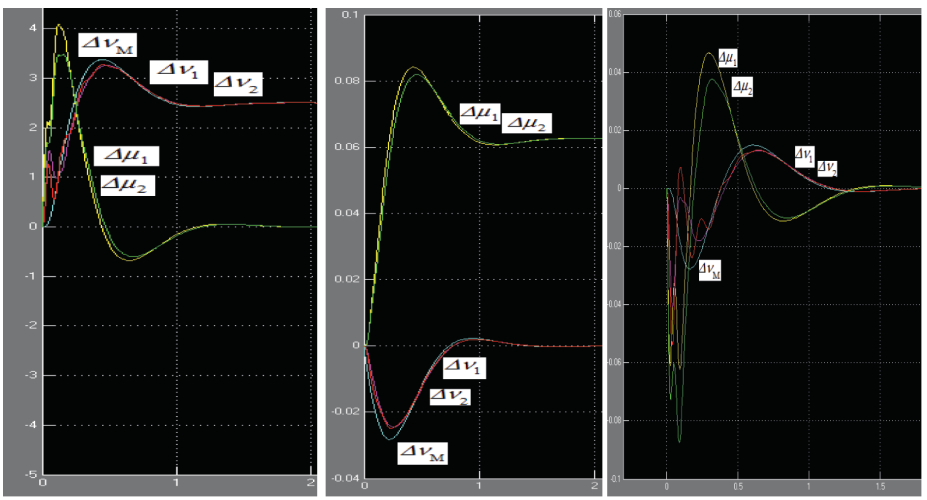

a) b) c)

Fig.4. Curves of transient processes with correction under control action (a), at the load (b), with a step change voltage in the circuit (c).

After introducing SR1 and SR2 to the inputs of flexible feedback with the transfer function

$$W_1(s) = \frac{0.035 \cdot s}{0.005 \cdot s + 1} \Rightarrow W_1(z) = \frac{7 \cdot (z - 1)}{z + 1} \tag{11}$$

dynamic characteristics were significantly improved as for input step type signal $\Delta \upsilon_0$ (Fig. 4a), as well as for loading step type signal $\Delta \mu_{ST}$ (Fig. 4b), also for stepwise voltage changing $\Delta \upsilon_S$ (Fig. 4c). Moreover, this system provides exact distribution of loading between the motors, since in the non-zero loading mode the condition $\Delta \mu_1 = \Delta \mu_2$ is satisfied (Fig. 4b).

4. CONCLUSIONS

1. For modern presses of paper-making machines, a simplified control system has been developed for a two-motor frequency-controlled ac electric drive with individual speed regulators and stator motor currents.
2. A mathematical model of the dynamics of the electric drive system has been obtained. As a result of the frequency analysis of the drive system object, expressions to determine the optimum parameters of digital regulators have been given. By modelling such kind of ac drive system on a computer transient characteristics are obtained, which are similar to dc thyristor drive ones with elastic links.
3. The proposed control scheme for a two-motor frequency drive provides an automatic load distribution between the motors by means of cross-links.

REFERENCES

4. Leonhard, W. (2001). *Control of Electrical Drives*. Berlin: Springer.
5. Raatz, E. (1981). Regelung von Antrieben mit Elastischer Verbindung zur Arbeitsmaschinen. *ENZ, A92, №4, 211-216.*
6. Dochviri, J. (2006). The Optimization of Transients in Multimotor Thyristor Electric Drives with Elastic Links for The Press Mechanisms of Continuous Technological Machines. *Russian Electrical Technology, R. A. Sci., (2), 34-42.*
7. Sokolovskii, G., et.al. (2002). Possibility of Simplification of the Mathematical Model of AC Drive by Construction of a Speed Control System. *J. Transactions of LETI, ser. Electrical Technology, Saint-Petersburg, (1), 3-7.*
8. Ogata, K. (1994). *Discrete-Time Control Systems*. Upper Saddle River, N.J.: Prentice Hall.
9. Antoniou, A. (1993). *Digital Filters: Analysis, Design and Applications.* New York: McGraw-Hill.
10. Dochviri, J., Khachapuridze, O. & Beradze, N. Digital Filter for Electrical Drive with Elastic Shaft. *American Journal of Electrical and Electronic Engineering, 3(5), 112-116.*

DIVDZINĒJU MAIŅSTRĀVAS ELEKTROPIEDZIŅAS DIGITĀLĀ VADĪBAS SISTĒMA, KAS UZBŪVĒTA PĒC HARLANDA PRINCIPIEM

J.N. Dochviri, G.R. Turmanidze

K o p s a v i l k u m s

Darbā tiek pētīta divdzinēju maiņstrāvas elektropiedziņas ar frekvences regulēšanu vienkāršotās skalārās vadības sistēmas dinamika. Piedziņas matemātiskais modelis tiek veidots, izmantojot elektromagnētisko procesu, ņemot vērā pārnesumu elastību. Rakstā sniegti vienādojumi, lai noteiktu digitālu regulatoru optimālos parametrus dzinēju statora strāvai un piedziņas ātrumam. Darbā arī atspoguļoti simulācijas rezultāti, kas iegūti Matlab. Konstatēts, ka piedziņas sistēma nodrošina optimālu dinamisko raksturu, kā arī precīzu slodzes sadali starp dzinējiem.

02.05.2017.

LATVIAN JOURNAL OF PHYSICS AND TECHNICAL SCIENCES
2017, N 4

DOI: 10.1515/lpts-2017-0024

MEASUREMENTS OF WAVE POWER IN WAVE ENERGY CONVERTER EFFECTIVENESS EVALUATION

J. Berins[1], J. Berins[2], A. Kalnacs[3]
[1] Faculty of Automation and Computer Engineering, Riga Technical University
1 Kalku Str., Riga, LV-1658, LATVIA
[2] Faculty of Power and Electrical Engineering, Riga Technical University
1 Kalku Str., Riga, LV-1658, LATVIA
[3]Institute of Physical Energetics
11 Krivu Str., Riga, LV-1006, LATVIA

The article is devoted to the technical solution of alternative budget measuring equipment of the water surface gravity wave oscillation and the theoretical justification of the calculated oscillation power. This solution combines technologies such as lasers, WEB-camera image digital processing, interpolation of defined function at irregular intervals, volatility of discrete Fourier transformation for calculating the spectrum.

Keywords: *discrete Fourier transformation, effectiveness, function interpolation, image processing, laser beam, spectrum, wave energy converter, wave height, wave power.*

1. INTRODUCTION

In the project "Operation Research of a Twisting and Rotating Wave Energy Conversion Plant", the objective was to assess the efficiency of dynamic systems of the energy receiver and converters in an environment such as waves. Resulting analysis showed that this could be achieved through specific measurement of time and space that fully characterised the environment without destroying it; it was both complex and at the same time within the project budget. This project phase resulted in technical measuring equipment for which there were other applications, such as level sensors of converters for adequate management development to ensure active wave energy capture systems. The draft of the proposed technical solution is based on the conservation of energy and the dynamic potential and kinetic energy balance of the surface wave in the gravitational field. Fixing the water surface elevation changes, characterised by the fluid potential energy during the time of change; it is possible to quantify the corresponding kinetic energy changes as well as the total energy of the system. It is a dynamic system so that the process of various measuring steps necessitates automation.

2. LASER MEASURE STRUCTURE

As a solution we used a laser height gauge, the web camera (the camera) image projected on the screen – float (at a certain angle) by the incident laser beam (beam) created light contrast "point" (Fig. 1). If the float is placed in the liquid, which is subject to wave type fluctuations, the vertical distance from the ray source will change and the image on camera will show the point horizontal offset. Fixing certain parameters in such a system, it is possible to solve the problem in an alternative way: measuring the point shift, it is possible to calculate the absolute distance of the surface or the relative deviation from the steady state.

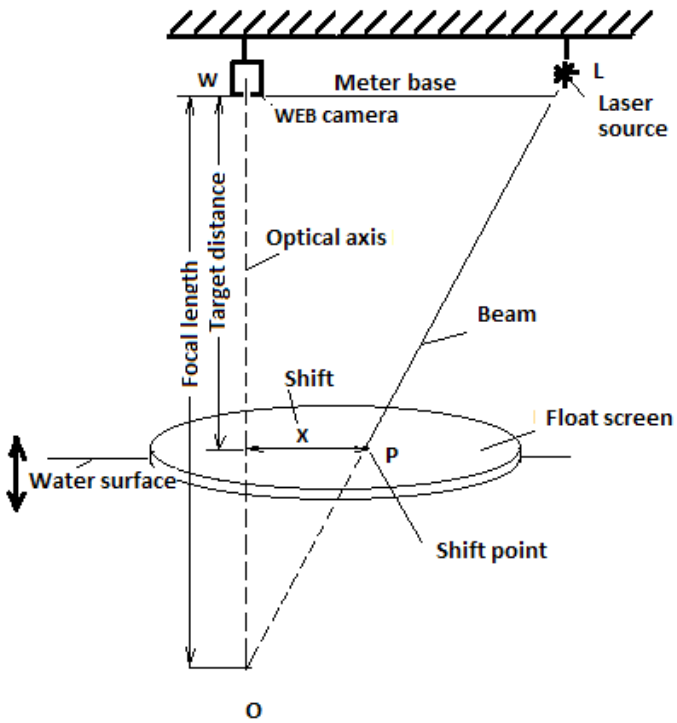

Fig. 1. Laser meter scheme.

This solution is functional and simple. In laboratory conditions, it promises to be sufficiently accurate.

3. OPTICAL SHEMATIC

Optical scheme (Fig. 2) space has two measurement dimensions consisting of vertically downward right-angled triangle whose hypotenuse LO is formed by a laser beam. Shorter cathetus WL with a narrow angle near the apex is formed by ray source L and camera W, whose lens centre is placed at the apex of the right-angled triangle. The central optical axis (the "axis") is WO. The straight edge of the camera centre to beam WL is base distance from camera to the laser source.

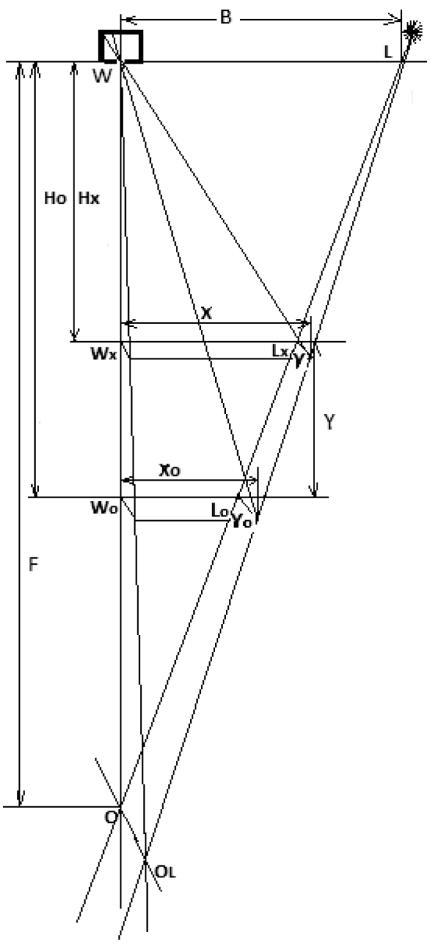

Fig. 2. Laser measure optical schematic.

The third dimension is used in beam LO shift OO_L from the measurement plane control and the vertical distance correction, if necessary. Thus, the float vertical distance between the triangle WLO apex O is expressed by two similar triangles W_0L_0O and WLO side ratios (Formula 1). In gauge terms, its looks like (Formula 2):

$$\frac{WO}{WL} = \frac{WxO}{WxLx}, \tag{1}$$

$$F - H_X = \frac{F}{B} \cdot X, \tag{2}$$

where H_x – the distance between the camera and the water level;

F – laser gauge focal distance;

B – laser gauge base distance;

X – laser beam shift from optical axis on float screen in millimetre.

The elevation Y measurement from zero water level *Wo*:

$$Y = H_0 - F \cdot (1 - \frac{X}{B}) \tag{3}$$

where, H_0 – the distance between the camera and the zero (no waves) water level *Wo*.

4. PIXEL LINEAR SIZE PROBLEM

The picture and images in the camera consist of pixels (dots). In an ordinary camera, there are 640x480 pixels. This is known as the standard VGA image resolution. Evaluation of the distance between two points in the camera image is not possible to detect in a different way than in these units. At the same time, it should be taken into account that the pixel is an angular unit. Every distance from camera corresponds to a different pixel linear dimension. In household applications, this is not critical, but in this case, it is necessary to know the camera pixel linear dimensions and to follow the changes in different distances from the camera lens (lens centre W). This means that given that the camera axis coordinates of the images in the camera are $x = 320$; $y = 240$, connection (3) expressing straight shift edge X in its linear dimensions has observable shift point coordinates. Thus, we obtain:

$$X = (x - 320) \cdot p_{X0} \cdot (\frac{1 + (x - x_0)}{H_0}), \tag{4}$$

where x – laser beam shift camera image from optical axis on float screen in pixels on the water level;

x_0 – the same on zero water level *Wo*;

p_{x0} – the pixel linear horizontal size at level H_0.

5. CALIBRATION

Constructive differences of various cameras and even one manufacturer's camera model or the influence of shifts can vary the pixel corresponding linear dimensions. After production the base measurement of B (cut-off) sizes may vary as the beam angle relative to the camera's optical axis can also vary. In this case, we chose a solution where in the manufacture of the equipment mechanical parts precision was not important. Numerical constants, which are necessary for processing the results of measurements, are obtained by calibrating equipment under laboratory conditions. The numerical values of linear distance are fixed in laboratory conditions. Distance Y and the shift X are calculated in (3) and (4). Unknown values are B and $p_{X0.}$ To obtain the determined solution, we need two independent equation systems, which means that it is necessary to fix system parameters in 2 different distance measurements.

A technical solution is that the beams and the optical axis angle depend on measuring conditions as soon as focal length F is variable and this measurement ad-

justment is made at the beginning of each measurement session, recording the shift from X_0 at a distance of H_0 (zero water level W_0).

The camera image has a fixed coordinate's window whose shift point should "hit". This is done to reduce image processing time and reduce the glare of different types of noise in the system.

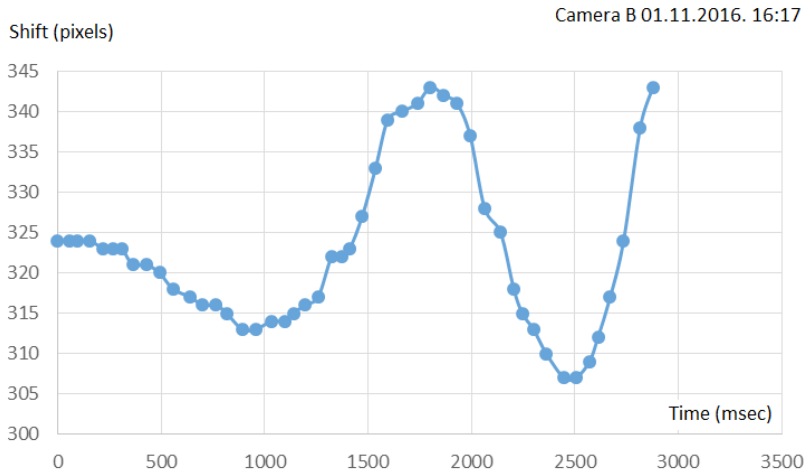

Fig.3. Graphical representation of B camera source data example.

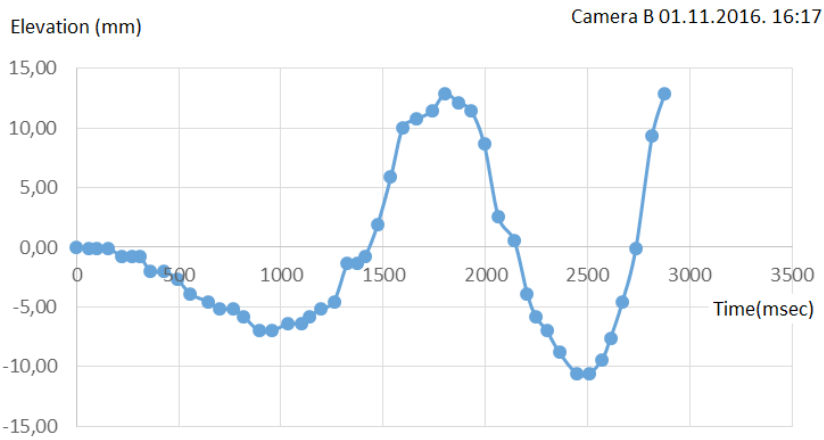

Fig. 4. Processed source data P_{X0} = 0.31mm B = 166.17mm.

6. MEASUREMENT PROCESSING

In measurement processing, we started with image processing: average shift point coordinate calculation, or the centre of the gravity coordinates and their fixation (in pixels) of the result file were synchronised with the time of the relative and absolute measurement of experimental sessions (in microseconds). As a result, we obtained source data. Example of source data sequence is shown in Fig. 3.

These data sequences are sufficient to be able to draw conclusions about waveform levels or offsets, but not "convenient" for the use of different analysis tools, further analysis of volatility, including components of the energy evaluation. The problem is the fact that in the processing of the data, we chose a universal computer, which runs the OS MS Windows 7. It has a number of advantages: user interface, device driver (connection interfaces and management programs), wide transmission spectrum of possibilities, data processing, storage and storage options. However, at the same time the prior complex process breaks in this case do not guarantee equal intervals between measurements, which leads to the next processing step based on intermittent time interval data replacement with as close as possible and smooth data substitution function $f = z\ (t)$, which provides realistic function values at any point in time.

7. INTERPOLATION SEGMENT AND INTERPOLATION WINDOW

Variable interpolation problem solutions were widely used in the past. There are a whole range of mathematical tools to solve this problem. The problem is the great number of variable defined points (several thousand). We introduced the "interpolation window" (Fig 5) and "interpolation segment" concepts. The interpolation segment has a final number of sequential time series data ($t_i\, Y_i$,) which are the subject of further analysis. The interpolation window has fixed number N of interpolation segment data, which allows using polynomial interpolation to get smooth curve approximation for incoming data. The interpolation process is carried out in two stages. In the first phase, using regression analysis with Excel LINEST array function polynomial modification, interpolation window "slides" (Fig. 5) over the interpolation segment. The N-th order polynomial coefficient value vector $K_{i,1}$: $K_{i,N+1}$ is calculated for substitution function expression for each window (5).

$$K_{i,1} : K_{i,N+1} = LINEST\left(Y_i : Y_{i+N}, t_i : t_{i+N}, pol\_order = N\right), \tag{5}$$

where Y_i:Y_{i+N} current interpolation window data set;
t_i:t_{i+N} current interpolation window time set.

The interpolation window is shifted by one step *(i+1)* and the polynomial coefficient calculations are repeated until the entire interpolation segment is thus treated ($i=1, \ldots, i_{max-N+1}$). The next step is to define a regular iteration step value Δt, choice of its number j_{max} and the selection of corresponding coefficient vector from an array of choice of features for substitution function $z\ (t_j)$ value calculation. To determine the irregular time interval, which corresponds to the current time t_j iteration value, $z(t_j)$ – function (8) built-in Excel tool *MATCH* based selective filter is used (6). For the $K_{i,1}$:$K_{i,N+1}$ vector addressing in the polynomial coefficient array an indirect addressing function *INDIRECT* (7) is used.

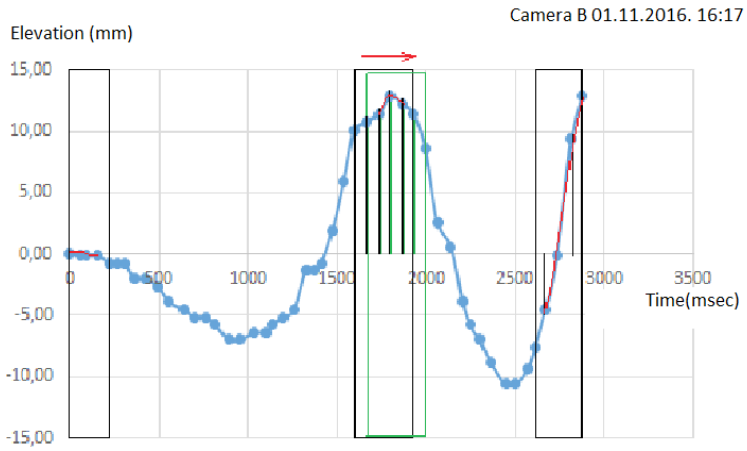

Fig. 5. Example of segment interpolated function with a sliding interpolation window.

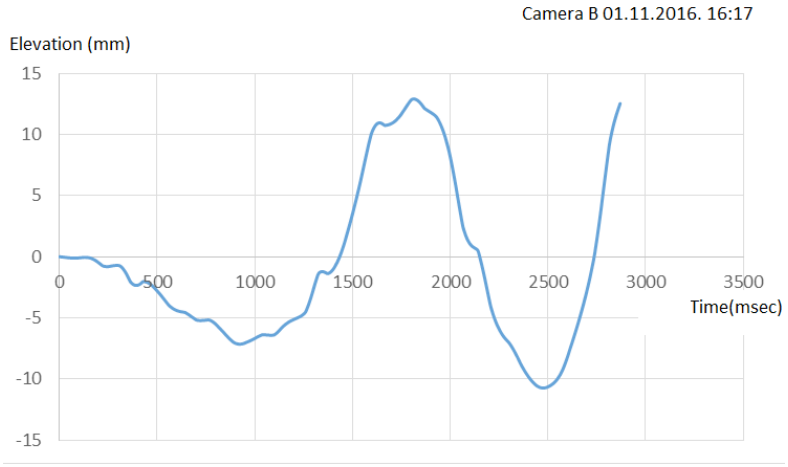

Fig. 6. Example of a smooth segment interpolated function with a regular iteration step Δt =7ms.

$$m = MATCH\left(t_j, t_i : t_{i\max}\right) \tag{6}$$

$$K_{j,1} : K_{j,N+1} = INDIRECT(array\ of\ coeficients[1:N, i:(i_{\max} - N + 1)], (m + D_m)), \tag{7}$$

where m – specific time interval fit number;

D_m – interpolation window interval shift for prevention curve distortions on interval borders.

As a result, we can obtain data substitution values (8) in any point of interpolation segment time

$$z(tj) = K_{j,1} \cdot t^N + K_{j,2} \cdot t^{N-1} + \ldots + K_{j,N} \cdot t + K_{j,N+1}, \tag{8}$$

for $j=1, \ldots, j_{max}$

8. DISCRETE FOURIER TRANSFORMATION

The next step in our wave analysis is irregular and unlinear oscillation split into various frequency sine wave components (9), [1].

The transformation result is a complex variable function (9) providing information about the relative contribution to the wave by each discrete frequency $k \cdot \Delta f$, for $j_{max}/2$ number of frequencies (regarding Nyquist criterion).

$$F(k \cdot \Delta f) = \sum_{j-1=0}^{j\,\max-1} z(j \cdot \Delta t) \cdot e^{-i(2\pi k \Delta f)\cdot(j-1)\Delta t}, \tag{9}$$

for k= 0, 1, 2, ...,j_{max-1}.

where k – discrete sine wave frequency number;

Δf – frequency resolution;

T – total sampling time or interpolation segment;

J_{max} – total number of discrete data points taken for analysis;

Δt – sampling time step value.

To obtain adequate results, we have to reduce unphysical error in the FFT called leakage. It is subject to follow certain conditions [1].

1. In principle, if an infinite number of discrete data points are taken, leakage would not be a problem. However, any real data acquisition system performing FFTs uses a finite number of discrete data points (in our case around 1000 points);
2. Time domain segment T for FFT application must be at least three oscillation periods (in practice at least 4 oscillation periods are used).
3.

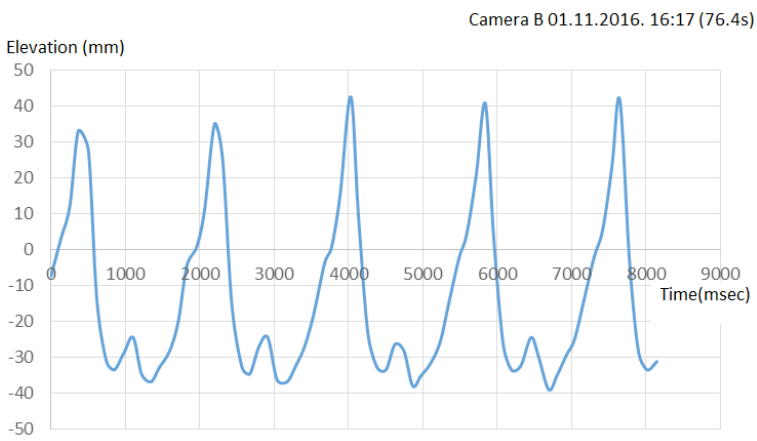

Fig. 7. Example of water wave time domain segment in measurement session, Camera B 16:17 01.11.2016.

To obtain the spectrum of normalized amplitude $A(m)$ of discrete sine wave m frequency $f(m)$, we used expression (10). To perform FFT, the number of analysing

function initial values has to be power of 2 (two) (16, 64, 128, 256, ...) to the argument, whose step must be constant (in practice, the number of initial values 1024 is used).

$$A(k) = \frac{IMABS\left(supplied\ complex\ variable(k)\right)}{512}, \tag{10}$$

where $$f(k) = k \cdot \frac{1}{T}. \tag{11}$$

The phase shift angle radians of oscillation frequency component θ (*k)* are available from the expression:

$$\theta(k) = IMARGUMENT\left(supplied\ complex\ variable(k)\right) \tag{12}$$

Thus, we have a visible picture of the constituent components of the oscillation (the amplitude and frequency known) (Fig. 8).

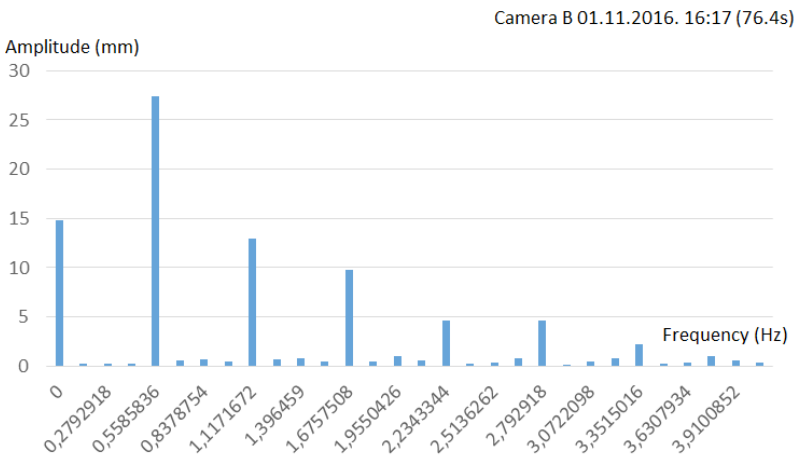

Fig. 8. Harmonic amplitude spectra after discrete Fourier transformation.

Using linear wave theory basic equation [4, p.408] we can calculate the average energy and power of each frequency *f(k)* component (harmonic) in this time segment:

$$E(k) = E_k(k) + E_p(k) = \frac{\rho g A^2(k)}{2} \tag{13}$$

and $$N(k) = E(k) \cdot C(k) = \frac{\rho g^2 A^2(k)}{4\pi f(k)}, \tag{14}$$

where k – discrete sine wave frequency number;
$A(k)$ – wave k-harmonic amplitude;
$f(k)$ – wave k-harmonic frequency;
ρ – water density;

g – gravitational constant;
Ek(k) – overage wave *k*- frequency harmonic kinetic energy*;*
Ep(k) – overage wave *k*- frequency harmonic potential energy*;*
E(k) – overage wave k- frequency harmonic energy*;*
N(k) – overage wave k- frequency harmonic power.

The last expression is applicable when for determination of the wavelength λ and the wave phase velocity C we can use the deep-water wave regularities (15,16), [2]:

$$\lambda = \lambda_0 = \frac{g \cdot T^2}{2\pi}, \tag{15}$$

$$C = C_0 = \frac{\lambda_0}{T} = \frac{g \cdot T}{2\pi}, \tag{16}$$

where λ_0 – wavelength in deep water;
C_0 – wave phase speed in deep water;
h – the water depth.

That is true if the conditions are met $h \geq \frac{\lambda_0}{4}$. (17)

If the condition is not met and $h < \frac{\lambda_0}{4}$, (18)

then assuming that there is not force of a deep-sea formula because although the wave height changes can be measured, the wave phase velocity C changes and should be calculated using equation (19) and for wave power calculation a correction $tanh\ (kh)$ should be applied for waveform at transition depth [2, p. 4]

$$C = C0\ \cdot tanh\ (lh), \tag{19}$$

where

l – wave number: $l\ = \frac{2\pi}{\lambda}$. (20)

An intermediate water wave length is

$$\lambda = C \cdot T = \frac{gT^2}{2\pi} \cdot tanh\left(\frac{2\pi h}{\lambda}\right). \tag{21}$$

It means, we have a transcendental equation (21), which is the reason why in practice for the adjustment we used graphics techniques [3, Fig. 2.2], which reflect the relative wave parameters $\frac{C}{C0}$ and $\frac{\lambda}{\lambda_0}$ as a function of depth and conditional deep-water wavelength relationship $\frac{h}{\lambda_0}$.

9. ENERGY SPECTRUM

Expression (14) allows getting an idea of the aggregate wave power (22) discrete frequency distribution (Fig. 9).

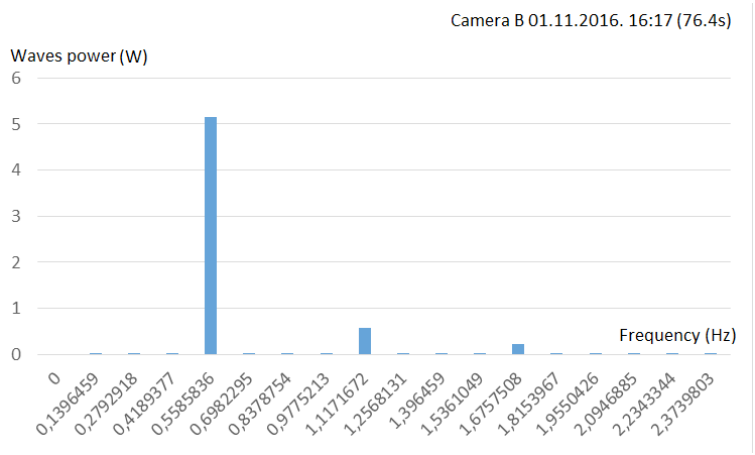

Fig. 9. Wave kinetic energy and average power frequency spectrum.

The total wave mean power N_{sum} of the plane wave, which is fitted with a laser measure gauge, is calculated as a sum of wave harmonic powers:

$$N_{sum} = \sum_{k=1}^{k_{sum}} N(k), \tag{22}$$

where k – wave harmonic number;

k_{sum} – upper frequency number value of wave harmonic sum range.

Figure 9 shows that to get wave power evaluation it is not necessary to sum all $j_{max}/2$ frequency harmonic powers. For present wave flume application above 2.8 Hz frequency power sum increase is practically zero (less than 0.2 %). Therefore, we can define wave harmonic frequency number limit or sum number range k_{sum}=20 (f(20)=2.8Hz).

10. THE SENSOR LOCATION

Locating wave environment “laser meter”, which can carry out the measurements and measure the oscillation amplitude and power management, should be based on a few considerations:

1. All of the aforementioned considerations are partly based on the assumption that the wave propagation direction is known because without additional conditions the practical wave propagation direction of point sensors cannot be determined. Conclusion – Lasers should be deployed in pairs. This theoretically makes it possible to experimentally determine the direction of wave propagation and wave phase speed, which is necessary for the calculation of wave power.

2. If foreign objects are inserted into the wave path dynamic system as a component, for example, with the object of wave energy absorption and conversion to another form of energy, in order to evaluate these devices it is necessary to obtain data on what part of the wave energy is consumed/ stifled. Conclusion – one detector should be placed in front of the equipment and the other – behind it.
3. Any foreign body will reflect part of the wave energy. This process affects the transformed energy balance / ratio. If this process is going to control the open water area, the receiver should be installed at a distance of two meters. A single detector and a fixed control measurement session without a receiver would suffice in a wave bath.

11. TESTING

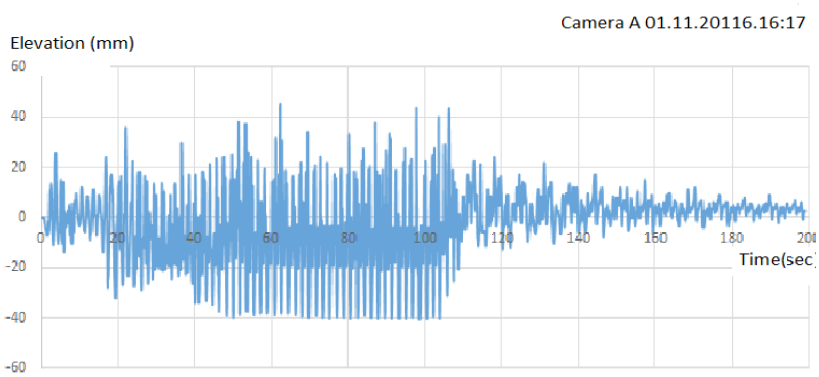

Fig. 10. Waves in a "no object" wave tank 1.95 m away from the wave generator.

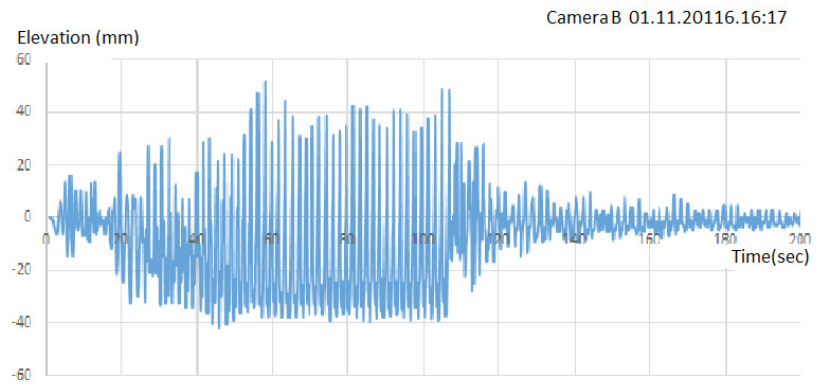

Fig. 11. Waves in a "no object" wave tank 3 m away from the A sensor and 1.98 m from the wave absorber.

On the basis of these considerations, in a wave bath 3 m away from each other, on both sides of the potential wave converter, 1.95 m away from the wave generator and 1.97 m from the wave absorber, we installed two calibrated measuring detectors (A, B). To test the wave tank unit, as regards to converter measurement, a test session without a converter was initiated (in a wave tank containing no alien object). The corresponding measurements are shown in Figs. 10 and 11.

12. CONCLUSIONS

The developed method allows for automated and efficient recording of wave surface elevation time function characterising data and saves them for further processing.

It allows keeping records of wave energy, power and determination of the changes between certain measure wave planes.

The chosen two laser measure configuration allows the receiver – wave tank system – to detect wave phenomena, such as resonance, standing waves, wave absorption, reflection, dispersion, and refraction.

Addressing the fluid wave energy receiver absorption determination, the project "Operation Research of a Twisting and Rotating Wave Energy Conversion Plant" within the framework of the solution chosen has been practically implemented (equipment and software have been developed for necessary measurements) and tested in real experimental conditions.

REFERENCES

1. Cimbala, J.M. (2010). *Fourier Transforms, DFTs, and FFTs*. Pensilvania, US: Penn State University. Available at http://www.mne.psu.edu/cimbala/me345/Lectures/Fourier_Transforms_DFTs_FFTs.pdf
2. Secretariat of the World Meteorological Organization. (1998). *Guide to Wave Analysis and Forecasting* (2nd ed.). Geneva, Switzerland, WMO-No. 702. Available at https://www.wmo.int/pages/prog/amp/mmop/documents/WMO%20No%20702/WMO702.pdf.
3. McCormic, M.E. (1981). *Ocean Vawe Energy Conversion*. New York, US: Wiley.
4. Twidell J., & Weir, T. (2006) *Renewable Energy Resources* (2nd ed.). London, UK: Taylor & Francis.

JAUDAS MĒRĪŠANA VIĻŅU ENERĢIJAS PĀRVEIDOTĀJU EFEKTIVITĀTES NOTEIKŠANAI

J. Beriņš, J. Beriņš, A. Kalnačs

K o p s a v i l k u m s

Raksts ir veltīts ūdens gravitācijas viļņu virsmas svārstību alternatīvas mērīšanas budžeta iekārtas tehniskā risinājuma un šo svārstību jaudas aprēķina teorētiskajam pamatojumam. Šis risinājums ietver tādas tehnoloģijas kā lāzera stars, WEB-kameras attēla ciparu apstrāde, neregulāros intervālos definēta funkcijas interpolācija, diskrētā Furjē transformācija svārstību harmoniku amplitūdu un jaudu frekvenču spektra aprēķināšanai.

12.04.2017.

LATVIAN JOURNAL OF PHYSICS AND TECHNICAL SCIENCES
2017, N 4

DOI: 10.1515/lpts-2017-0025

SOLID STATE PHYSICS

NITROGEN ADSORPTION ON GRAPHENE SPONGES SYNTHESIZED BY ANNEALING A MIXTURE OF NICKEL AND CARBON POWDERS

V. Grehov[1], J. Kalnacs[1], A. Mishnev[2], K. Kundzins[3]
[1]Institute of Physical Energetics,
11 Krīvu Str., Riga, LV-1006, LATVIA
[2]Latvian Institute of Organic Synthesis,
21 Aizkraukles Str., Riga, LV-1006, LATVIA
[3]Institute of Solid State Physics, University of Latvia,
8 Kengaraga Str., Riga, LV-1063, LATVIA

Adsorption by graphene sponge (GS) manufactured by annealing nickel-carbon powder mixture in inert atmosphere has been studied. By determining the specific surface area (SSA) for the GS sample, it has been found that Brunauer, Emmett, Teller method (BET) of approximation of experimental isotherms gives wrong results in the pressure range of 0.025–0.12 because adsorption in this pressure region is affected by walls of ampoule. Real SSA value has been found by subtracting pore effect method (SPE) or by BET approximation in a low range of relative pressure of 0.0004–0.002.

Keywords: *graphene sponge, nitrogen adsorption, specific surface area, BET approximation.*

1. INTRODUCTION

The study is dedicated to the adsorption properties of new graphenic material graphene sponge (GS) developed by the authors [1] by annealing nickel-carbon powder mixture in inert atmosphere.

Many studies have been devoted to the adsorption properties of carbon materials [2], [3]. It can be explained by a variety of morphological properties of carbon materials known as activated carbons, carbon blacks and carbon nanotubes, cones, fibres, bulbs, graphenes, graphene aerogels, foams and sponges [4], [5].

Graphene, 2D carbon allotrope, has drawn significant interest among scientists due to intriguing properties since 2004 [6]. In recent years, the assembly of graphene into macroscopic (3D) structures has attracted intensive interest because the use of 3D graphene is one of the most effective ways of applying the unique properties of 2D graphene nanosheets in practice [4], [7]. Graphene 3D structures consist of flexible graphene nanosheets, which are interconnected into porous networks.

Several different names have been used for such structures, namely, graphene foam, sponge, aerogel and monolith. Among the attractive applications, graphene sponges have been used as adsorbents for various pollutants [5]. For instance, less than 3.5 kg graphenic carbon foam can absorb 1 ton petroleum, promising great potential in the applications of oil spill and pollution treatments [7].

It is well known that the pore size and its distribution are important factors determining the adsorption properties of different adsorbents. It is of interest to relate the adsorption properties of the GS to its morphological structure and to elucidate the possibilities of changing this structure during the preparation of the GS.

2. EXPERIMENTAL

To reveal the nature of GS adsorption capacity, its specific surface and pore size distribution (PSD), the authors of the research studied the adsorption of nitrogen at 77K using Autosorb-1 device (*Quantachrome Instruments Co*., Florida, USA). The methods of measurements were standard (see the previous article about adsorption properties of thermochemically exfoliated graphite (TEG) [8]). The level of liquid nitrogen was supported automatically. During measurement, the substance was placed into a quartz ampoule 9 mm in diameter. To reduce the empty volume, a glass rod was used.

The samples for adsorption measurements were small pieces of GS manufactured by the authors of the research [1].

The substance weight was 1–5 mg in each case. Before measuring adsorption, the GS was heated in vacuum at 300 °C for not less than 24 h, before the leak rate became lower than 10–15 micron/min. To process and present the results, ASWin v1.55 and home-made software were used.

All investigated GS samples were analysed by means of SEM (Hitachi M3000), high resolution SEM LYRA3 XMU (Tescan, Czech Republic), transmission electron microscope (TEM) Tecnai G20 (FEI) and XRD (Japan Rigaku ULTIMA IV, Cu–Ka radiation $\lambda = 0.154184$ nm).

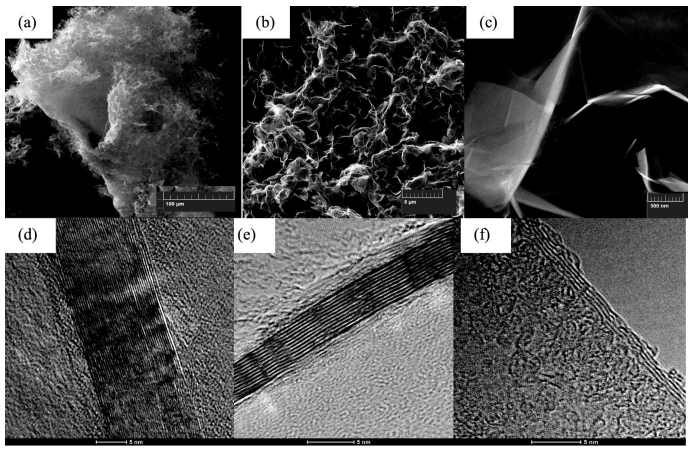

Fig. 1. High resolution SEM images (a), (b), (c) – typical GS samples, (d), (e), (f) – high resolution TEM image of the same samples after dispersion in the isopropanol by ultrasound.

3. RESULTS AND DISCUSSION

Figure 1 demonstrates typical GS images with different magnifications. It can be clearly seen that the GS consists of graphene sheets that are well-developed in the base plane (002), entangled and partly interconnected, with folds and wrinkles. The thickness of these sheets was determined from the XRD spectra by the width of the (002) peak [1]. The values obtained for the GS sheet thickness were in the range of 6–16 nm. The individual graphene sheets of GS were examined using TEM [9]. The GS material was placed in isopropanol and dispersed by ultrasound and then a drop of isoprapanol with suspended graphene sheets was applied to the grid for electronic microscopy. For TEM, a copper grid with a holey carbon film (Agar Scientific, UK) was used.

In all the GS samples studied, sheets with a different number of layers from 2 to 40 were found in approximate correspondence with the thickness obtained from the XRD data. A similar range of values of the graphene layers was shown on the multilayer graphene obtained on transition-metal foams by the chemical vapour deposition (CVD) method [10]. The dissolution of carbon in the metal takes place using CVD process [10] and Ni – carbon powder annealing methods [1]. When a carbon atom precipitates on the metal, at the cooling stage, the formation of multilayer graphene sheets occurs. The authors of the research attempted to control the number of layers in multilayer sheets of graphene by controlling carbon weight in the Ni – carbon mix [1].

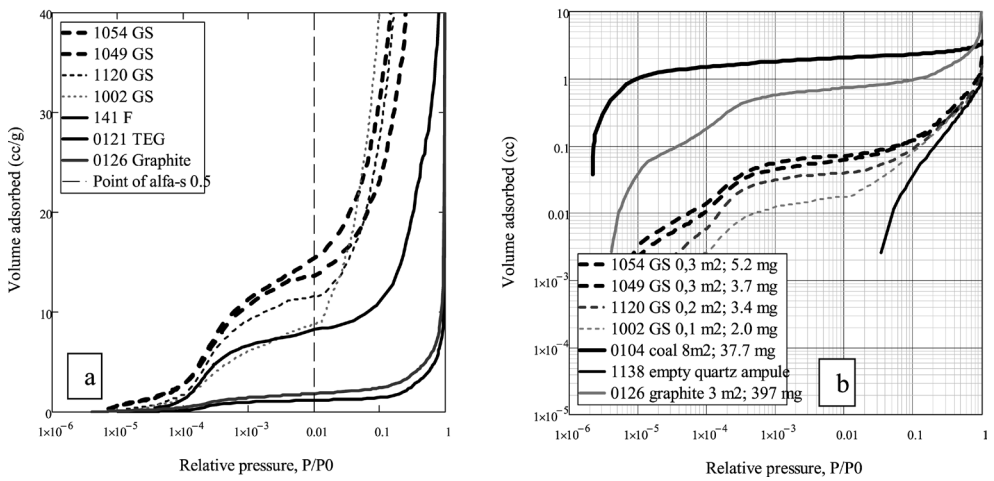

Fig. 2. N2 adsorption by grafitized carbon: graphene sponges (1054, 1049, 1120, 1002), graphitized carbon black Carbopack F (141), milled graphite (0126). a – specific volume of adsorption for different samples, b – adsorbed volume for these adsorption processes, on the inset the areas and weights of the samples are indicated.

On the multilayer graphene sheets (Fig. 1e, f), a non-uniform surface of graphene sheets can be observed; these inhomogeneities could possibly serve as the basis for the formation of micropores (<2 nm). Investigation of adsorption for the GS samples showed that it was well-graphitized carbon material.

Objects of this type are well studied on powder samples of graphitized carbon blacks [11], [12]. They are characterised by II or IV type isotherms (IUPAC [13]) depending on the absence or presence of micro and mesopores.

The authors of the research examined the isotherms of GS samples in comparison with the isotherms of other graphitized carbon samples performed by the authors earlier [8], and also during the present research (Fig. 2a). According to the characteristic form of adsorption isotherms at low pressures (smaller as ~ 0.01 P/P_0), it was clear that they referred to adsorption on a graphite surface. Further increase in adsorption observed for the GS samples at P/P_0~0.01–0.15 should not occur because the adsorption of the second monolayer N2 onto the graphene surface began only at P/P_0>0.15 [14]. This increase in adsorption could formally be associated with an increase in the capillary condensation in the presence of pores ~2 nm [15]. However, the authors of the research prefer another explanation.

The upward deviation of adsorption can be explained as follows: at pressures greater than 0.01 P/P_0, the adsorbed volume on the GS becomes smaller than the volume adsorbed on the ampoule walls, which is explained by the fact that the total amount of adsorbed volume ceases to depend on the mass of the GS and adsorption lines for different GS samples become approximately equal to the empty ampoule adsorption (Fig. 2b).

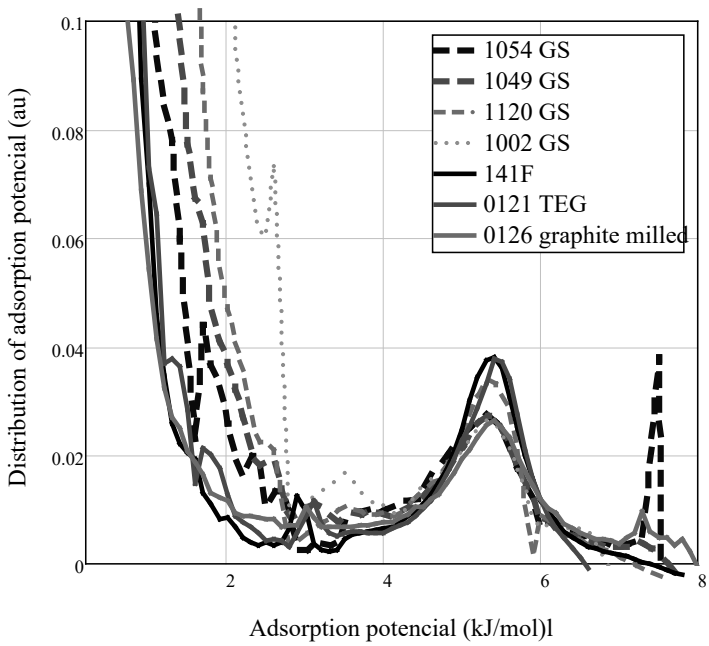

Fig. 3. Adsorption potential distribution for N2 adsorption by grafitized carbon: milled graphite, graphene sponges (GS), thermoexpholiated graphite plates (TEG) [11], graphitized carbon black Carbopack F.

It should be taken into account that in the instructions of the device manufacturer (Autosorb-1) it is explicitly stated that the area of the measured adsorbent should be 10–15 m^2. The area and weight of the measured samples are shown in Fig. 2b. The reason for working with such small samples of GS is related to the equipment on which the samples were obtained [1].

In further research, we believed that the growth of adsorption at pressure above ~ 0.01 P/P_0 was associated with adsorption on the ampoule walls. Fortunately, adsorption at low pressures was associated only with GS, which allowed obtaining positive results.

The distribution of the adsorption potential (APD) for all the samples studied in the research was calculated from isotherms (see Fig. 3). The adsorption potential is the energy that is released upon adsorption of N2 molecules on the adsorbing surface. On a homogeneous surface, all places have the same energy, so the filling of the surface with the first layer of molecules occurs in a narrow pressure range. The APD can be regarded as the negative derivative of the adsorption isotherm [3]. Note that the frequency curve of the distribution of APD is normalized to the volume of the monolayer of adsorbate.

The APD of various carbon black adsorbents was considered in [11], [12] in accordance with the degree of their crystallinity. The APD of highly graphitized samples of Carbopack F with high crystallinity showed three peaks at approximately 5.5, 3.0, and 0.7 kJ/mol. These signals were attributed to the formation of the nitrogen monolayer, to a two-dimensional fluid-solid transition and to the second layer formation, respectively. For the Carbopac X sample with the lowest degree of crystallinity, only the high-energy peak of the formation of the first monolayer at 5 kJ/mol was manifested. The authors [12] noted that the Carbopack samples with high SSA exhibited lower crystallinity, and they suggested that it might be difficult to obtain highly graphitized carbons with large SSA.

In our case, it may be noted that the closer the width and position of the APD peak for the GS samples to the peak for Carbopac F, the more perfect the structure of the adsorbing surface. For our GS samples in Fig. 3, only the first peak corresponding to the filling of the first monolayer is clearly manifested, the second peak corresponding to the phase transition is manifested as “noise” due to a small amount of matter in the sample (dashed curves in Fig. 3). For large samples of the TEG, the peaks at 5.5 and 3.0 kJ/mol are clearly visible. Note, in Fig. 3, the “ampoule effect” manifests itself in a faster rise in the frequency curve for GS samples that are smaller in weight and area.

One of the main parameters for adsorbents is the specific surface area (SSA). The definition of SSA BET [16] method is recommended and universally accepted [2], [17]. However, the choice of the isotherm points for the BET approximation in our case for a graphitized surface ($P/P_0<0.12$ [9]) is not sufficiently defined [8].

The possible range of the obtained SSA values is quite large, even within a high correlation coefficient. In the paper, the authors analysed the use of BET as an approximation for different isotherm sections with a correlation coefficient of at least 0.997 (Fig. 4).

From the physical point of view, for the application of the BET method, it is necessary to select an isotherm section for which adsorption proceeds only through a multilayer mechanism and processes of volume absorption in micropores or capillary condensation do not increase adsorption.

Another method for determining the SSA described by K.S.V. Sing is a comparative method of “alpha-s” [17].

The method consists in comparing the investigated isotherm with the reduced reference isotherm (alfa-s) for a nonporous sample. Reduction of the reference isotherm occurs by dividing the values of the isotherm by the value at pressure P/P_0=0.4. The investigated isotherm is compared with a reference isotherm for a related adsorbent for which a complete absence of pores is asserted and, hence, adsorption proceeds along a multilayer mechanism. At the same time, K.S.V. Sing indicated that in the case of similarity isotherms, SSA can be determined using a simple relation (1):

$$A_x/A_{ref} = S_x/S_{ref} \quad (1)$$

Moreover, the adsorption values A_x and A_{ref} were proposed to be used for the value of the relative pressure 0.4:

$$S_x = A_{x,0.4} \cdot S_{ref}/A_{ref,0.4} \quad (2)$$

In other words, if there are no other reasons, the difference in adsorption is due to the difference in specific areas.

The selection of another part of the isotherm for the determination of SSA was proposed and substantiated by K. Kaneko [15], [18] – the subtraction pore effect method (SPE).

The method is based on the fact that at low pressure, at which "alpha-s"<0.5, the pore filling swing occurs, and at higher pressure, when the "alpha-s">0.5 for graphitized materials an increase in adsorption occurs due to beginning of cooperative processes such as capillary condensation.

Therefore, the application of relation (1) occurs at the point "alpha-s"=0.5 or in a small rectilinear section near 0.5 (Fig. 5). For clarity, it is proposed to connect the origin with the isotherm point for "alfa-s"=0.5 and determine the SSA by the slope angle of the segment. The value "alpha-s"=0.5 corresponds to the relative pressure around P/P_0=0.01. To plot the curves in Fig. 5, the volume values on the required isotherm were recalculated to the pressure values on the reference isotherm by the method of linear interpolation.

Determination of the desired area with respect to the angle of the slope is the application of the same relation (2), only to the other point on the scale of pressure:

$$S_{x(Alfa=0,5)} = A_{x(Alfa=0,5)} \cdot S_{ref}/A_{ref(Alfa=0.5)} \quad (3)$$

To verify the performance of a multilayer process, one can construct the ratio $A_x \cdot S_{ref}/S_x \cdot A_{ref}$ as a function of pressure (Fig. 6). The multilayer process – P/P0 ranges from 0.1 to 0.4 – is clearly visible for the non-porous sample "KON" [18], in which the ratio is approximately equal to 1.

For GS samples, the ratio approaches unity within the range of 0.9–1.1 in the pressure region near P/P_0=0.01.

It is seen from Fig. 6 that the curves for GS, unlike the curves for a nonporous

sample and highly graphitized Carbopack F, raise sharply after a minimum at $P/P_0 \approx 0.1$.

This behaviour could be explained by the presence of a significant number of pores with a size of 2 nm and higher, but in our particular case, the rise is caused by adsorption on the walls of the ampoule.

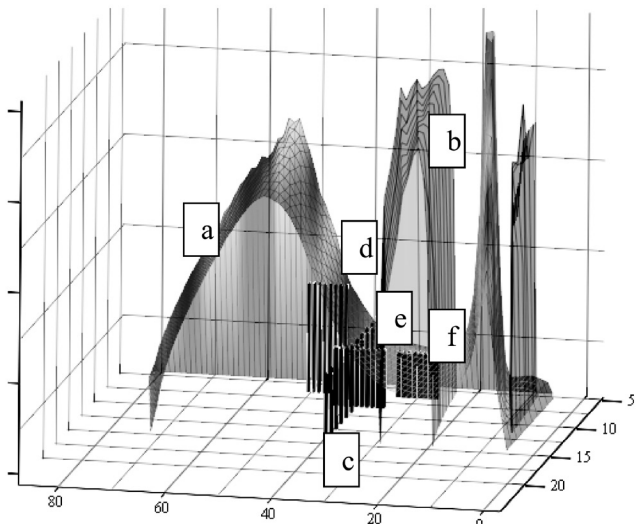

Fig. 4. BET surface calculated (a) for adsorption isotherms of the sample GS 1049. The horizontal axes represent: number start point (0 to 80) and the number of points (5 to 15) at which the SSA was calculated and located on the vertical axis. Surface (b) corresponds to a portion of the correlation coefficient that exceeds 0.997. Vertical segments (c, d, e, f,) are the bar plots which correspond to the places of SSA determination and height of the bars equal to the determined SSA. Segment (c) – points with pressure near 0.01 for SPE method; (d) – points for relative pressure 0.05–0.12; (e) – points with pressure near to 0.01 and correlation coefficient near 0.997; (f) – points for maximal correlation coefficient which corresponds to relative pressure of 0.0004–0.002.

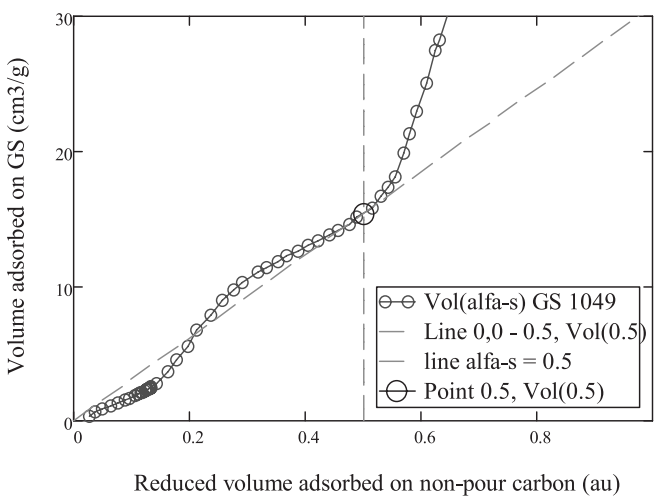

Fig. 5. Alfa–s plot. Volume adsorbed by GS sample (1049 Ni10mix069 1000rapidH2400) vs reduced volume adsorbed on reference non-porous carbon [19].

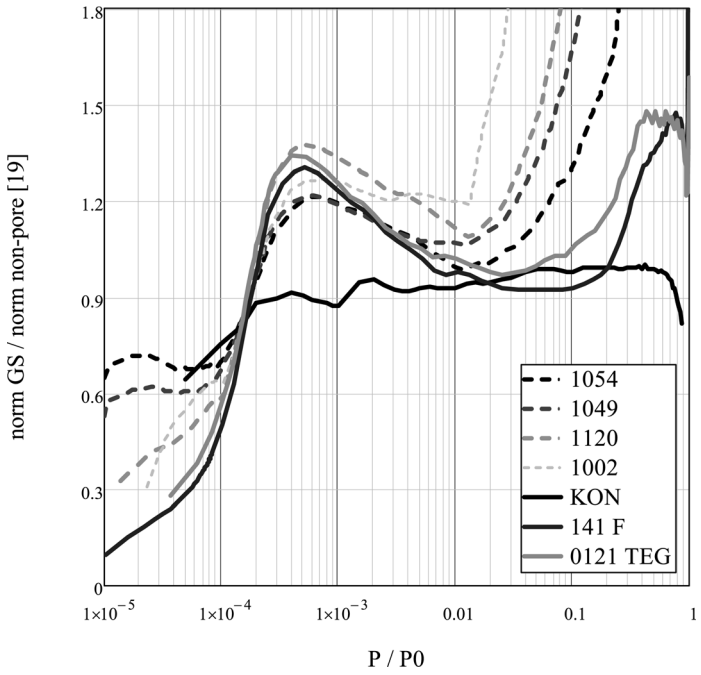

Fig. 6. Relationship $A_x \cdot S_{ref}/S_x \cdot A_{ref}$ between adsorption for some GS samples vs relative pressure. GS samples 1054, 1049, 1120; Sample 1141 F measured on highly graphitized Carbopack F (Aldrich); non-porous samples KON [18] and reference non-porous carbon [19].

Table 1 and Fig. 7 show the results of determination of SSA for a number of GS samples by BET methods in accordance with Fig. 4 and SPE in accordance with Fig. 5.

Table 1

The Results of Determination of SSA for GS Samples

SSA	GS №	**1069**	**1040**	**1049**	**1110**	**1107**	**1054**	**1119**	**1002**	**1120**
S BET, m^2/g	0.0004 – 0.002	84.5	66.9	61	43.9	120.1	60.8	43.6	34	49.1
S BET, m^2/g	P/P0=0.01	111.6	87.8	79.2	62.3	156.6	75.2	54	46.3	57.4
S SPE, m^2/g	P/P0=0.01	116.8	93.8	84	70.3	157.5	74.7	56.2	47.4	63.1
S BET, m^2/g	0.025–0.12	230.4	522.6	150.4	333.6	260.8	104	153.9	374.9	158.7
Thickness, Å	RTG “t”	85	104	83	107	38	88	116	91	111
GS weight from balance,g		0.0019	0.0012	0.0037	0.0015	0.0027	0.0052	0.0028	0.002	0.0034
Bulk density * of GS, mg/cm^3		13.3	13.6	14.8	no	no	17.9	9.8	12.6	10
Area ** GS, m^2	0.0004 – 0.002	0.16	0.08	0.22	0.06	0.32	0.31	0.12	0.07	0.17

* The density of GS samples was determined from the ratio of the weight in a dry state with respect to the wet weight (after boiling in water).

** The area of GS samples was determined from the multiplication of the weight of GS onto the SSA determined by the BET method in the range of P/P_0~0.0004–0.002

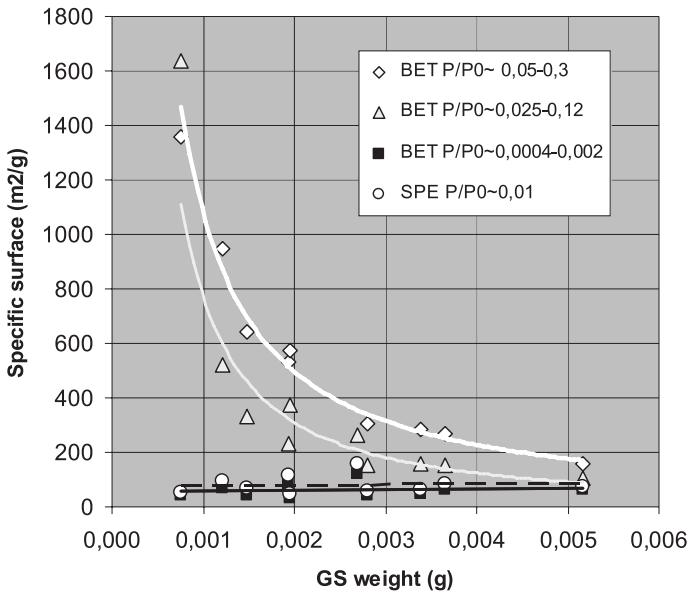

Fig. 7. SSA of GS samples determined with different ways by BET and SPE methodes and P/P0 regions. Lines - trendlines for SSA points. SSA determined at points of P/P0 0.0004 – 0.002 had a maximal correlation coefficient 0.9999. These points laid around of maximum at Fig. 8 or around knee at Fig. 2.

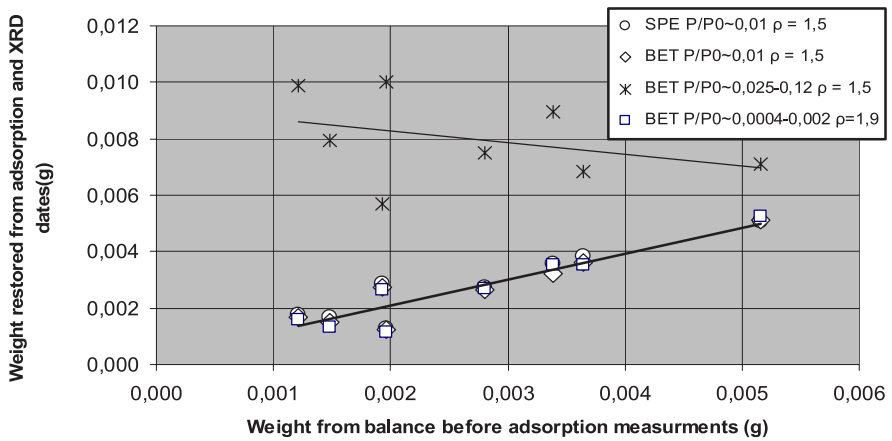

Fig. 8. Weight of GS samples restored from the data of N2 adsorption and XRD measurement. All symbols – weight restored from experimental data for different ways of SSA determination; BET and SPE; P/P0 regions and density ρ values. Lines – trendlines for calculated weight points.

It follows from Fig. 7 that the SSA values for different P/P_0 ranges have different dependencies on the weight of the GS samples. For low P/P_0 pressure less than or equal to 0.01, the SSA values are independent of weight, and for pressure greater than 0.01, the SSA values increase with a decrease in sample weight. The analysis shows that this is due to the fact that the adsorption value for such pressure is

determined not by the GS sample but also by the ampoule walls as indicated above (Fig. 2b).

The GS samples investigated in the first approximation can be represented as a set of multilayer graphene plates (Fig. 1c) with approximately the same thickness and density. The sample weight can be determined from adsorption data and XRD. Using SSA for each sample and its thickness (according to XRD), it is possible to calculate its weight by a simple ratio:

$$W = SSA \cdot w \cdot t \cdot \rho, \tag{5}$$

where w is the true (by weight) weight of the sample, t is the thickness, ρ is the density. At the same time, it becomes possible to compare different methods for determining SSA and to estimate the density of the objects – multilayer graphene plates based on the fact that the true weight is known. The results of the calculations are presented in Fig. 8. Figure 8 shows the weight points of the GS samples calculated from relation (5) for the SSA values obtained by the BET method from the pressure range of 0.025–0.12. A large scatter and complete lack of proportionality to the true weight indicate that these SSA values are erroneous and the isotherm path at this pressure range is associated with adsorption on the ampoule walls.

It follows from Fig. 8 that the weight values calculated for smaller P/P_0 values can be equated to the weight of the GS samples under the assumption that the density of multilayer graphene plates is either ρ=1.5 g/cm^3 for SSA in the P/P_0~0.01 region, or ρ=1.9 g/cm^3 for SSA values determined in the area of the maximum correlation of BET approximation for P/P_0~0.0004–0.002.

The value of the density of volumetric graphite is 2.3 g/cm^3 and the values from 1.5 to 1.9 g/cm^3 for a multilayer graphene plate are possible. Note that in this case it should be assumed that graphene plates have pores inaccessible to adsorption of nitrogen molecules.

On the other hand, based on the assumption that GS is a collection of multilayer graphene plates with approximately the same thickness, the formula for SSA is as follows:

$$SSA_{calc} = 1/(t \cdot \rho), \tag{6}$$

where t is the thickness, ρ is the density of the graphene plate. This formula is equivalent to formula (5) and is needed to check the correlation with another independent parameter – the thickness t obtained from the XRD data.

For each GS sample with specified thickness of the graphene layer, in Fig. 9 the SSA values were obtained by different methods (Fig. 4 and Fig. 5) and SSA calculated from the hyperbola formula (6) for two density values ρ=1.5 g/cc and ρ =1.9 g/cm^3 of a multilayer graphene plate. Figure 9 shows that the hyperbolas at such values of the density approximately correspond to the scatter of the experimental values of SSA.

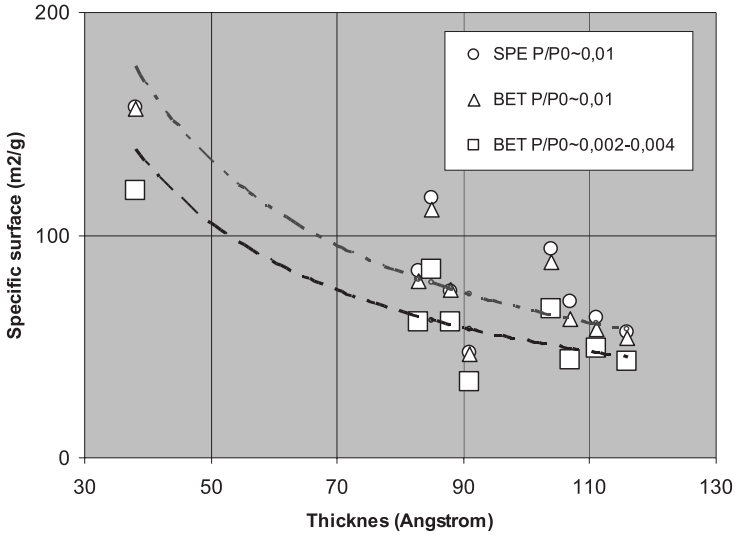

Fig. 9. SSA of GS samples vs thickness of multilayered graphene plates from XRD measurement. Circles, triangles, squares – experimental data for SSA determined in different ways; circles – by SPE metode; triangles – by BET method for P/P0 ~ 0.01; squares – by BET method for points at which BET approximations had a maximal correlation coefficient larger than 0.9999. These points had a range of P/P0 0.0002–0.004. Hyperbolic lines were calculated by formula (6) with density values ρ = 1.5 (upper) and ρ =1.9 g/cm^3 (lower).

Comparison of the initial section of adsorption isotherms for GS and well-graphitized objects – Carbopac F, graphite milled, TEG – has led to the conclusion that the surface of multilayer graphene plates in the GS is of good quality. The representation of our GS as a set of multilayer graphene plates (Fig. 1c) with approximately the same thickness and density made it possible to calculate the weight of the GS samples with a reasonable assumption of the graphene plate density ρ=1.9 g/cm^3. Note that the calculation did not take into account the adsorption at the edges of multilayer graphene plates, which was possible for large graphene sheets.

The longitudinal dimension of the La crystallite can be estimated from the width of the XRD peak (100), the obtained value La~10–12 nm [1]. The longitudinal size of the crystallites can also be estimated from the Raman scattering [20]; the values obtained are from one to several tens of nanometres. Note that the outer dimensions of multilayer graphene plates range from 0.1 to 1 μm. Under the assumptions outlined above, it is possible to evaluate the methods for determining SSA.

4. CONCLUSIONS

The research has demonstrated the difficulties of measuring the adsorption of nitrogen on ultralight GS samples with a mass of 1 to 5 mg and a bulk density of 10–15 mg/cm^3. The reason can be explained by the small area of the adsorbing surface of the samples of GS 0.1–0.3 m^2, which made it possible to obtain an adsorption isotherm for GS only for low relative pressure P/ P_0<0.01-0.015 due to the fact that within this pressure range adsorption on the walls of the ampoule does not practically occur (Fig. 2b). Note that the representation of adsorption data from small

objects shown in Fig. 2b is of methodological significance since it has allowed correctly estimating the size of the sample area relative to the effect of adsorption on the surface of the ampoule.

To obtain the SSA value corresponding to its geometric meaning, BET approximation in the range of 0.0004–0.002 P/P_0 should be used for our samples. This range corresponds to the best correlation coefficient of BET approximation and gives the lowest SSA values. From another point of view, this range corresponds to the primary filling of a well-crystallized graphite (or graphene) surface.

Further refinement of the true value of SSA requires additional experiments with GS samples with an adsorbing surface of 5–10 m^2 and independent estimates of the density of the graphene layer.

ACKNOWLEDGEMENTS

The present research has been supported by the National Research Programme for 2014–2017 "Multifunctional Materials and Composites, Photonics and Nanotechnologies".

REFERENCES

1. Grehov, V., Kalnacs, J., Mishnev, A., & Kundzins, K. (2016). Synthesis of graphenic carbon materials on nickel particles with controlled quantity of carbon. *Latvian Journal of Physics and Technical Sciences, 53*, 56–12.
2. Schiith, F., Sing, K., & Weitkamp, J. (eds.) (2002). *Handbook of Porous Solids*. Weinheim: Wiley-VCH Verlag GmbH.
3. Bottani, E.J., & Tascon, J.M.D. (eds.) (2008). *Adsorption by Carbons*. Elsevier Ltd.
4. Inagaki, M., Qiu, J., & Guo, Q. (2015). Carbon foam: Preparation and application. *Carbon*, *87*,128–152.
5. Wu, R., Yu, B., Liu, X., Li, H., Wang, W., Chen, L., … Yang, S.T. (2016). One-pot hydrothermal preparation of graphene sponge for the removal of oils and organic solvents. *Appl. Surf. Sci., 362*, 56–63.
6. Novoselov, K.S., Geim, A.K., Morozov, S.V., Jiang, D., Zhang, Y, Dubonos, S.V., Firsov, A.A. (2004). Electric field effect in atomically thin carbon films. *Science*, *306*, 666–669.
7. Sun, H., Zhen Xu Z., & Gao, Ch. (2013). Multifunctional, ultra-flyweight, synergistically assembled carbon aerogels. *Advanced Materials, 25*, 2554-2560.
8. Grehov, V., Kalnacs, J., Matzui, L., Knite, M., Murashov, A., & Vilken, A. (2013). Nitrogen adsorption by thermoexfoliated graphite. *Latvian Journal of Physics and Technical Sciences*, *50*, 58-66.
9. Grehov, V., Kalnacs, J., Vilken, A., Mishnev, A., Knite, M., & Kundzins, K. (2015). Structural investigation of graphenic carbon materials obtained on nickel particles. *FM&NT-2015 Functional Materials and Nanotechnologies*, 115–115.
10. Tynan, M.K., Johnson, D.W., Dobson, B.P., & Coleman, K.S. (2016). Formation of 3D graphene foams on soft templated metal monoliths. *Nanoscale, 8*, 13303-13310.
11. Darmstadt, H., & Roy, C. (2001). Comparative investigation of defects on carbon black surfaces by nitrogen adsorption and SIMS. *Carbon, 39*, 841–849.
12. Kruk, M., Li, Z., Jaroniec, M., & Betz, W.R. (1999). Nitrogen adsorption study of sur-

face properties of graphitized carbon blacks. *Langmuir*, *15*, 1435–1441.

13. Sing, K.S.W., Everett, D.H., Haul, R.A.W., Moscou, L., Pierotti, A., Rouquerol, J., & Siemieniewska, T. (1985). Reporting physisorption data for gas/solid systems. *Pure & App Chem*, *57*(4), 603–619.
14. Ohba, T., Takase, A., Ohyama, Y., & Kanoh, H. (2013). Grand canonical Monte Carlo simulations of nitrogen adsorption on graphene materials with varying layer number. *Carbon, 61*, 40–47.
15. Setoyama, N., Suzuki, T., & Kaneko, K. (1998). Simulation study on the relationship between a high resolution a-s plot and pore size distribution for activated carbon. *Carbon, 36*, 1459–1467.
16. Brunauer, S., Emmett, P., & Teller, E. (1938). Adsorption of gases in multimolecular layers. *J. Amer. Chem. Soc., 60*, 309–319.
17. Грег, С., & Синг, К. (1984). Адсорбция, удельная поверхность, пористость. Москва: МИР.
18. Kaneko, K., Ishii, C., Ruike, M., & Kuwabara, H. (1992). Origin of superhigh surface area and microcrystalline graphitic structures of activated carbons. *Carbon*, *30*, 1075–1088.
19. Silvestre-Albero, A., Silvestre-Albero, J., Martı´nez-Escandell, M., Futamura, R., Itoh, T., Kaneko, K., & Rodrı´guez-Reinoso, F. (2014). Non-porous reference carbon for N2 (77.4 K) and Ar (87.3 K) adsorption. *Carbon*, *66*, 699–794.
20. Grehov, V., Kalnacs, J., Vilken, A., Mishnev, A., Chikvaidze, G., Knite, M., & Saharov, D. (2014). Graphene Nanosheets Grown on Ni Particles. *RCBJSF-2014-FM&NT*, 303-303.

SLĀPEKĻA ADSORBCIJA UZ GRAFĒNA SŪKĻIEM, TOS SINTEZĒJOT NIĶEĻA UN OGLEKĻA MAISĪJUMA IZKARSĒŠANAS UN ATLAIDINĀŠANAS REZULTĀTĀ.

V. Grehovs, J. Kalnačs, A. Mišņevs, K.Kundziņš

K o p s a v i l k u m s

Pētīta grafēna sūkļu sorbcijas spēja, to raksturojot ar īpatnējo absorbcijas virsmas laukumu. Nosakot īpatnējā virsmas laukuma lielumu izmantota Brunauera, Emmeta, Tellera (BET) metode izotermu aproksimācijai spiedienu diapazonā 0.025-0.12. Parādīts, ka BET metode šajā diapazonā uzrāda lielas kļūdas, jo gadījumos, kad īpatnējais laukums relatīvi mazs 0,1 līdz 0,3 m^2 netiek ņemta vērā adsorbcija uz ampulas sienām, kura ir salīdzināma vai lielāka nekā absorbcija uz pētāmā objekta.

Reāli dati par grafēna sūkļu īpatnējo absorbcijas virsmu iegūstami ar poru efekta atskaitīšanas metodi (angļu – subtracting por effect - SPE method), vai tad, ja BET aproksimāciju izmanto mazu relatīvo spiedienu P/P_0 diapazonā 0,0004 – 0,002.

21.05.2017.

LATVIAN JOURNAL OF PHYSICS AND TECHNICAL SCIENCES
2017, N 4

DOI: 10.1515/lpts-2017-0026

STABILITY AND THE ELECTRONIC STRUCTURE OF XB_2 (X = Pt, Ir, Pd, Rh, Os) DIBORIDES

A.I. Popoola, A.Y. Odusote, O.E. Ayo-Ojo
Department of Physics,
Federal University of Technology, Akure, NIGERIA.
Email: ispopoola71@gmail.com

First-principle calculations have been performed to investigate the structural and electronic properties of platinum group metal diborides in the stoichiometry XB_2 (X = Pt, Ir, Pd, Rh, Os). All investigated compounds have shown to belong to the orthorhombic *P*mmn space group rather than the *C*2/m previously predicted in some of the compositions. Compressibility will reduce with boron addition in Pt, Pd and Rh, but will increase with boron addition into Ir and Os. The electronic density of states show that all the compounds are metals, with PtB_2, PdB_2 and OsB_2 being potentially incompressible and superhard materials.

Keywords: *bulk modulus, hardness, machinability, metallic diborides, thermodynamic stability*.

1. INTRODUCTION

Hard materials with high bulk modulus are materials of choice in a wide variety of industrial applications. They are used as abrasives, cutting tools and coatings where wear prevention or scratch resistance is important. Apart from hardness, they have demonstrated exceptional thermal conductivity, refractive index and chemical stability [1], [2]. The development of a new class of hard materials is of prime importance. High valence electron density and bond covalence are required in the creation of ultra-incompressible, hard materials. The valence electron density for diamond, the hardest known substance, is 0.705 electrons/Å^3. It has an exceptionally high bulk modulus B_0 of442 GPa. Covalent bonding dominates in hard materials. Unlike covalent materials, the electrostatic interactions in ionic materials are omni-directional, leading to low bond-bending forces and automatically, to low shear modulus [3], [4]. Hard materials are often plagued by intrinsic brittleness, poor thermal shock resistance and the difficulty of machining into sharp edge/complex shapes.

For platinum group metal related materials, pure Osmium (Os) has exceptionally high (395-462 GPa) bulk modulus, while its hardness is 400 kg/mm^2 [5]. The high bulk modulus of Os can mainly be attributed to its high valence electron density, while its low hardness is related to the metallic bonds and its hexagonal close-packed (HCP) crystal structure. OsB_2 has been synthesized [6], [7]. It is a

highly incompressible (365-395 GPa) and hard (≥2000 kg/mm^2) material [8]. Two different structures, the *P*mmn orthorhombic [9] and the *C*2/m monoclinic [10] have been reported in IrB_2 through *ab initio* density-functional theory calculations. The structure of RhB_2 has also been proposed to be monoclinic at ambient pressure [11].

Platinum, iridium, rhodium and palladium are all neighbours to Os, with high valence electron density. Specifically, the stoichiometry-property data on platinum and palladium borides are scanty. Some of the impressive properties of Pt, Pd, Ir and Rh are: high corrosion resistance, high melting points and good ductility [12]. These impressive properties could predispose them to good compositional design of new metallic borides. It should be noted that, Pt (3.5MPa), Pd (4.75MPa), Rh (6.0MPa) and Ir (6.5MPa) are softer compared to Os (7.0MPa). Evidence has shown that pure but soft transition metals will become hard materials when combined with small covalent bond-forming atoms such as boron, carbon, oxygen, or nitrogen [13], [14], [15]. It should therefore be a worthy adventure to investigate the effect of boron on Pt, Ir, Rh and Pd. The structure of Pt, Rh, Ir and Pd is cubic. Application benefits are expected from these materials and the results could perhaps help predict new phases in Pt, Ir, Os, Rh and Pd diborides. The goal of the present research is to carry out density functional calculations on the electronic properties and the bulk modulus of XB_2 (X = Ir, Os, Pt, Rh, Pd). Where necessary, clarity will be provided between competing structures and new materials will be predicted.

1.1 CRYSTAL STRUCTURE OF METAL DIBORIDES

The widely reported structures for metallic diborides are the AlB_2 (P6/mmm) structure, the monoclinic (*C*2/*m*) structure and the orthorhombic (*P*mmn) structure (Fig. 1). The metals locate at (0,0,0) and boron at (and (Wyckoff positions in the AlB_2 structure, while in the monoclinic structure, metal atoms are at (0.409; 0.00; 0.836) with boron atoms at (0.669; 0.00; 0.488) and (0.708; 0.50; 0.264), respectively. In the orthorhombic structure, the metal atoms locate at (0.25; 0.25; 0.1545) and boron at (0.0557; 0.25; 0.6325) and (0.444; 0.25 0.6325) Wyckoff positions. Our investigation covers all these three structures. However, similarity in atomic packing exists between hexagonal and cubic structures - they both have closed packed planes. Only one plane exists in hexagonal structures, while there are four in cubic structures. Close packed planes predisposes a material to slip, a phenomenon that can be of immense benefits for the mechanical properties of such material. Therefore, a hypothetical cubic phase of the diborides is considered. The adopted cubic structure has slight modification from the hexagonal type, wherein same Wyckoff atomic positions are assumed.

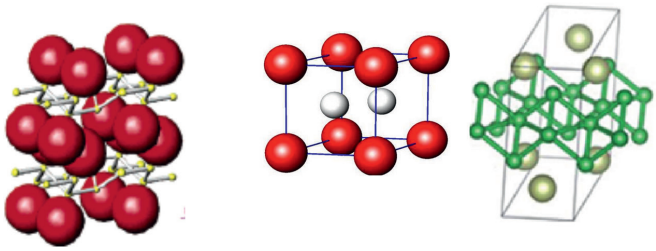

Fig.1. Different structure types in metallic diboride – left: *P*mmn; middle: AlB_2 and right: *C*2/m.

2. CALCULATION METHODS

All numerical calculations were performed using the QUANTUM ESPRESSO (QE) code [16]. QE is a DFT code that uses plane waves as a basis for the wavefunctions and a pseudopotential to treat core electron interactions. The Generalized Gradient Approximation of Perdew-Burke-Ernzerhof [17] was used for the exchange and correlation functional. The following: Ir ($3d^74s^2$), Pt ($4s^24p^1$), Rh ($4d^{10}5s^25p^1$), Pd ($3s^2$ $3p^2$), Os($5s^2$ $5p^2$) and B ($5s^2$ $5p^3$) respectively were treated as valence by the pseudopotentials. The smearing was fixed at 0.06 with the Marzari-Vanderbilt smearing scheme. The k-point sampling in the Brillouin zone (BZ) was performed using the Monkhorst–Pack scheme [18]. The energy-cutoff for the plane-wave basis sets was 75 Ry with 8×5×6, 6×8×7 and Γ-centered Monkhorst–Pack grids conducted for the electronic BZ integrations for the orthorhombic, C2/m and the hexagonal structures, respectively.

Each crystal structure relaxation was carried out with the Broyden-Fletcher-Goldfarb-Shanno (BFGS) minimisation technique. The criteria for convergence in optimising the atomic internal degrees of freedoms were as follows: difference on total energy within 1×10^{-8} Ry/atom, ionic Hellmann-Feynman forces within 0.001 Ry/a.u. Each structure and its internal coordinates were first optimised to get a relaxed structure. The total energy per unit cell as a function of volume was calculated and the results were fitted using the Birch-Murnaghan equation of state (eq. 1) to get the bulk modulus [19]. The step size for volume contraction/expansion was 0.2. About 10 data points, evenly distributed around the equilibrium lattice constant were used.

$$P(V) = \frac{3B_0}{2}\left[\left(\frac{V_0}{V}\right)^{\frac{7}{3}} - \left(\frac{V_0}{V}\right)^{\frac{5}{3}}\right]\left\{1 + \frac{3}{4}\left(B_0' - 4\right)\left[\left(\frac{V_0}{V}\right)^{\frac{2}{3}} - 1\right]\right\} \quad (1)$$

with

$$B_0 = -V\left(\frac{\partial P}{\partial V}\right), \quad (2)$$

where is the isothermal volume, is the isothermal bulk modulus, is the derivative of the bulk modulus with respect to pressure and is the energy of the material which is found by integrating (1) and given as:

$$E(V) = E_0 + \frac{9V_0B_0}{16}\left\{\left[\left(\frac{V_0}{V}\right)^{\frac{2}{3}} - 1\right]^3 B_0' + \left[\left(\frac{V_0}{V}\right)^{\frac{2}{3}} - 1\right]^2\left[6 - 4\left(\frac{V_0}{V}\right)^{\frac{2}{3}}\right]\right\} \quad (3)$$

The formation energy ($\Delta E^{\ominus}$), is traditionally used to gauge if a substance can be made by conventional means. $\Delta E^{\ominus}$ is the energy of XB_2 relative to pure X and isolated B atoms in their equilibrium crystal structures [20] and it was evaluated according to (4).

$$\Delta E^{\Theta}(\mathrm{XB_2}) = \frac{1}{3}E^{\Theta}_{\mathrm{XB_2}} - \left[\frac{1}{3}E^{\Phi}_{X} + \frac{2}{3}E^{\psi}_{B}\right], \quad (4)$$

where $\Delta E^{\Theta}_{XB_2}$ is the total energy of XB_2 with Θ structure, E^{Φ}_{X} is the total energy per atom of X with Φ structure and E^{ψ}_{B} is the total energy per atom of B with ψ structure. Negative formation energy indicates a thermodynamically stable material, while a positive one indicates an unstable or metastable material.

3. RESULTS AND DISCUSSION

Calculations were carried out on four different crystal structures – the traditional AlB_2 structure, the monoclinic *C*2/m, the orthorhombic *P*mmn and a cubic structure with the same composition and atomic positions as the AlB_2 structure. Since the cubic structure is hypothetical, three possible atomic position arrangements were investigated. The results are shown in Fig. 2. The celd1 curve is for the arrangement that has X atoms at the (0; 0; 0) positions, celd2 is for the arrangement where X atoms are at $(\frac{1}{3};\frac{1}{6};\frac{1}{2})$ and celd3 is for the arrangement in which X atoms locate at $(\frac{2}{3};\frac{1}{3};\frac{1}{2})$. It is evident from the curves that the most stable arrangement is the ones in which X (metal) atoms locate at the (0; 0; 0) position. Therefore, for both the hexagonal and the cubic noble metal XB_2 (X = Pt, Ir, Rh, Pd) diborides, the X atoms will prefer the (0, 0, 0) position while the two boron atoms will prefer the $(\frac{1}{3};\frac{1}{6};\frac{1}{2})$ and $(\frac{2}{3};\frac{1}{3};\frac{1}{2})$ positions.

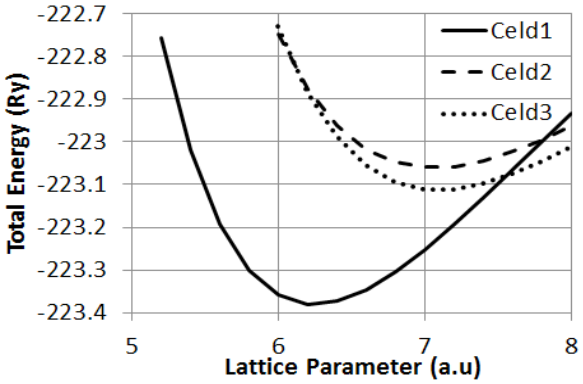

Fig.2. Energy curve for different atomic configuration in the cubic structures of XB_2 (Pt, Ir, Rh, Os, Pd)

The relative energy (E_0) among the phases is given in Table 1. XB_2 (X = Ir, Os, Pt, Rh, Pd) has the lowest energy in the orthorhombic *P*mmn phase. The ground state structure of OsB_2, IrB_2, PtB_2, RhB_2 and PdB_2 is therefore, predicted to be orthorhombic and not cubic, monoclinic or hexagonal. This result agrees with the previous result on OsB_2 [8]. Our result on IrB_2 agrees with the work of Chen et al. [9] but not with that of Binchua et al. [10]. Our result is predicting the orthorhombic *P*mmn structure in PtB_2 and PdB_2 because the E_0 for this phase is much more thermodynamically stable than other phases. Considering the bulk modulus (B_0), it

is important to note the closeness between our calculated results and experimental values for the elemental platinum group metals. The proximity between our calculated values (389.7 GPa) and the experimental values (365--395 GPa) for OsB_2 in the *P*mmn phase gives one the confidence that the bulk moduli are reliable for prediction. Hardness is one of the unique properties of metallic diborides. It is an intrinsic property, difficult to describe with a formal theoretical definition. It can be studied indirectly because it correlates with many physical properties such as ionicity, melting point, elasticity, cohesive energy, etc. The bulk modulus (i. e. material resistance to uniform compression) scales roughly with hardness [20] and it has been used with success to determine hard materials. Based on the bulk modulus results in Table 1, the hardness of the materials are predicted in the order of $RhB_2 > OsB_2 > PdB_2 > IrB_2 > PtB_2$. All values in this range are exceptionally high, exceeding or matching other hard materials, including boron carbide (200 GPa), silicon carbide (248 GPa), sapphire (252 GPa), and c-BN (367 GPa), and almost approaching that of diamond (442 GPa). It is evident from the B_0 results that incompressibility would increase by about 116% when boron (B) is added to Pd, by about 27% when B is added to Pt and about 5.36% when B is added to Rh. Adding boron into Ir and Os would reduce their compressibility by 4.53% and 18.3% respectively.

With regard to the formation energy, ΔE^{Θ}, all the compounds in the *P*mmn structure have negative but lower ΔE^{Θ} compared to the other phases and are predicted to be more thermodynamically stable. Solid solution should be readily formed between boron and Pt, followed by Pd, Ir, Os, and Rh. The electronic density of states (DOS) and the atom resolved partial density of states (PDOS) are crucial to the understanding of physical properties of materials. The DOS and PDOS for the *P*mmn phases of XB_2 (X = Ir, Pt, Os, Rh, Pd) at 0 GPa are shown in Fig. 3. The finite electronic DOS at the Fermi level (zero point on the x-axis) indicates that all the compounds are metallic. The DOS and the atom resolved PDOS for OsB_2, PtB_2 and PdB_2 are similar. Much overlap is seen between the d-electron of Pt, Pd, Os and the p-electron states of boron. Strong covalent bond is predicted in these compounds. No clear overlap is seen between the d- and f-electron states of IrB_2 and RhB_2. For engineering applications, the ability of a material to be machined into sharp edge or complex shapes is important. Borides with low hardness (i.e., hexagonal Boron Nitride and MAX phases) are readily machinable. The machineability of the XB_2 diborides is therefore predicted in the reverse order to their hardness, i.e., IrB_2 and RhB_2 should be more machineable than PtB_2, PdB_2, and OsB_2.

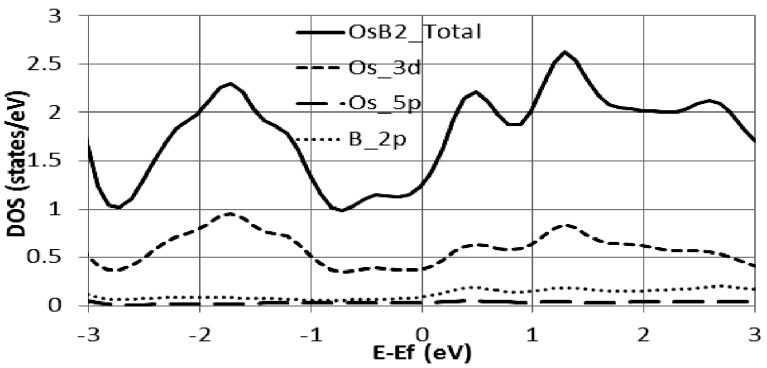

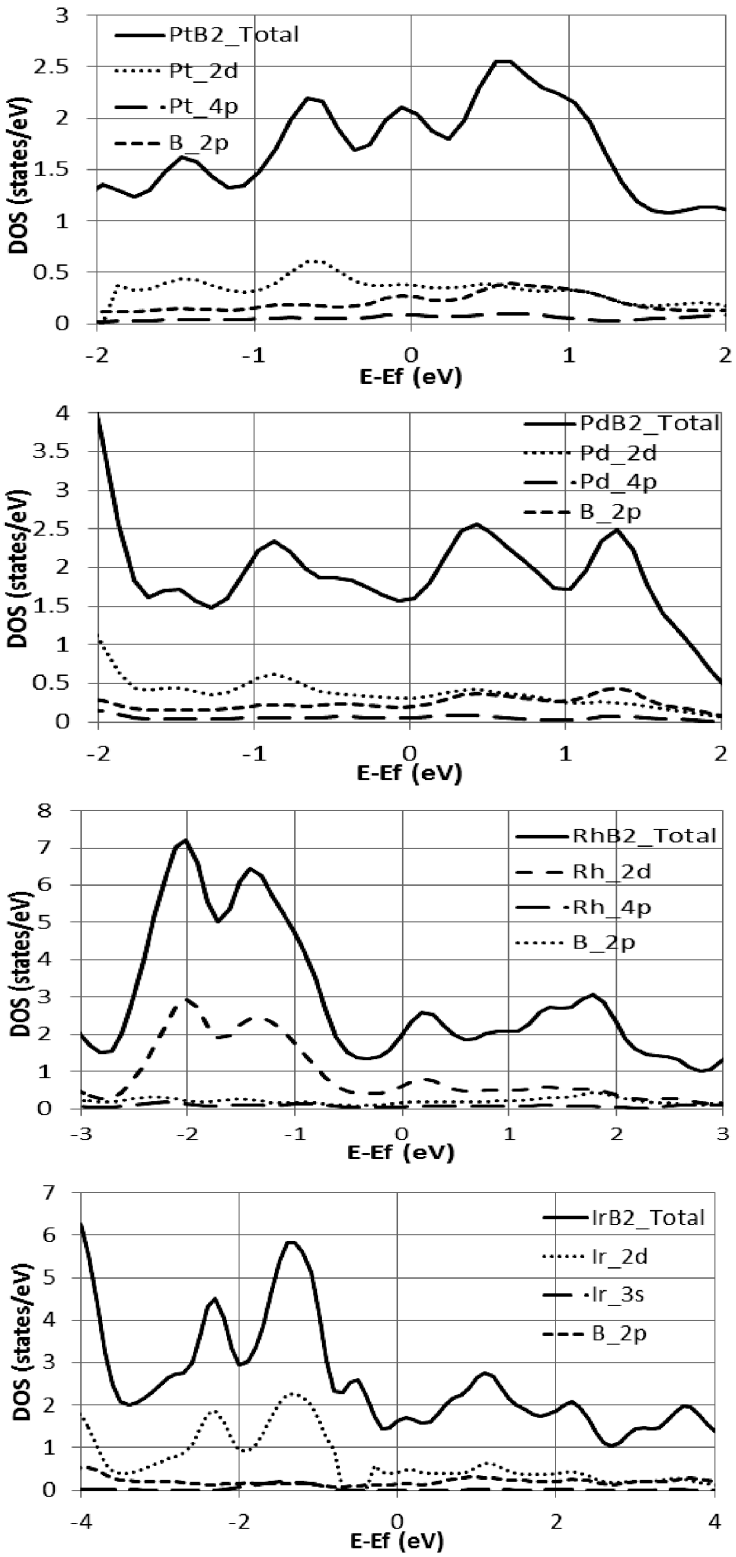

Fig. 3. The total and partial DOS for OsB_2, PtB_2, PdB_2, RhB_2 and IrB_2 in the *P*mmn structure. The Fermi level (on the x-axis) has been shifted to zero point.

Table 1

Calculated Formation Energy (ΔE^{Θ}), Equilibrium Ground State Energy (E_0) and the Bulk Modulus (B_0) for the Elemental Platinum Group Metals, the Cubicγ, Hexagonal‡, Monoclinic^{a} and the Orthorhombic$^{\$}$ Structures of XB_2 (X = Pt, Ir, Os, Pd, Rh)

Mater.	ΔE^{Θ}(Ry)	E_0(Ry)	B (GPa)
Pt	-	-	276.7 [230]
Ir	-	-	379 [320]
Rh	-	-	374 [380]
Pd	-	-	172 [180]
Os	-	-	461 [462]
RhB_2	-129.31$^{\gamma}$ -133.23‡ -129.15^{a} -313.30$^{\$}$	-183.90$^{\gamma}$ -187.76‡ -183.68^{a} -367.70$^{\$}$	160.4$^{\gamma}$ 371.4‡ 341.4^{a} 393.6$^{\$}$
IrB_2	-140.19$^{\gamma}$ -144.64‡ -140.07^{a} -334.84$^{\$}$	-194.43$^{\gamma}$ -198.78‡ -194.26^{a} -388.84$^{\$}$	180.4$^{\gamma}$ 370.2‡ **338.2**^{a} 362.5$^{\$}$
PdB_2	-152.85$^{\gamma}$ -157.53‡ -152.77^{a} -364.32$^{\$}$	-211.39$^{\gamma}$ -215.95‡ -211.16^{a} -422.69$^{\$}$	161.1$^{\gamma}$ 353.7‡ 307.1^{a} 372.1$^{\$}$
PtB_2	-172.45$^{\gamma}$ -176.43‡ -162.40^{a} -385.10$^{\$}$	-223.38$^{\gamma}$ -237.22‡ -223.15^{a} -446.72$^{\$}$	183.9$^{\gamma}$ 374.6‡ 322.8^{a} 352.5$^{\$}$
OsB_2	-103.29$^{\gamma}$ -107.44‡ -102.99^{a} -314.52$^{\$}$	-211.18$^{\gamma}$ -215.39‡ -211.02^{a} -422.33$^{\$}$	241.3 $^{\gamma}$ 396.7‡ 347.4^{a} 389.7$^{\$}$ [365-395]

Experimental data in parentheses are from references [8], [21], [22].

4. CONCLUSIONS

Using first-principle calculations based on density functional theory, an orthorhombic *P*mmn structure has been shown to be the ground-state structure for IrB_2, OsB_2, PtB_2, RhB_2, and PdB_2. PtB_2 is the most energetically favoured when compared to the other compounds. It is worth noting that boron will affect the compressibility of Pt, Rh and Pd differently to that of Os and Ir. The compressibility of elemental Os is much higher than for Rh. Surprisingly, boron addition in Rh should lead to much improvement in its compressibility than its addition into Os. According to the

calculated DOS and PDOS, it is concluded that PtB_2, PdB_2, and OsB_2 are potentially incompressible and superhard materials than IrB_2 and RhB_2.

REFERENCES

1. Thornton, A., & Wilks, G. (1978). Clean surface reactions between diamond and steel. *Nature, 274,* 792 – 793.
2. Solozhenko, V. L., Andrault, D., Fiquet, G., Mezouar, M., & Rubie, D. C. (2001). Synthesis of superhard cubic BC_2N. *Appl. Phys. Lett. 78*(10)*,* 1385 - 1387.
3. Haines, J., Léger, J. M., & Bocquillon, G. (2001). Synthesis and Design of Superhard Materials. *Annu. Rev. Mater. Res., 31*(1)*,* 1 - 23.
4. Kaner, R. B., Gilman, J. J., & Tolbert, S. H. (2005). Materials science. Designing superhard materials. *Science, 308,* 1268 - 1269.
5. Hebbache, M., & Zemzemi, M. (2004). Ab initio study of high-pressure behavior of a low compressibility metal and a hard material: Osmium and diamond. *Phys. Rev. B, 70,* 224107.
6. Roof, R. B. Jr., & Kempter, C. P. (1962). New orthorhombic phases in the Ru-B and Os-B. *J. Chem. Phys. 37*(7)*,* 1473 – 1478.
7. Stuparevic, L., & Zivkovic, D. (2004). Phase diagram investigation and thermodynamic study of OsB system. *J. Ther. Anal. Calori., 76*(3)*,* 975 - 983.
8. Cumberland, R. W., Weinberger, M. B., Gilman, J. J., Clark, S. M., Tolbert, S. H., & Kaner, R. B. (2005). Osmium diboride, an ultra-incompressible, hard material. *J. Am. Chem. Soc., 127,* 7264 – 7265.
9. Wang, D. Y., Wang, B., & Wang, Y. X. (2012). New crystal structures of IrB and IrB2: First-principles calculations. *J. Phys. Chem. C, 116,* 21961 – 21966.
10. Chu, B., Li, D., Bao, K., Tian, F., Duan, D., Sha, X., & Cui, T. (2014). The crystal structure of IrB2: A first-principle calculation. *RSC Adv., 4,* 63442 – 63446.
11. Chu, B., Li, D., Bao, K., Tian, F., Duan, D., Sha, X., Liu, Y., & Cui, T. (2015). Structural, mechanical, and electronic properties of Rh_2B and RhB_2: First-principles calculations. *Scientific Reports 5,* doi: 10.1038/srep10500.
12. Wolff, I.M., & Hill, P.J. (2002). Platinum Metals-Based Intermetallics for High-Temperature Service. *Platinum Metals Review, 44*(4)*,* 158 - 166.
13. Haines, J., Léger, J. M., & Atouf, A. (1995). Crystal Structure and Equation of State of Cotunnite-Type Zirconia. *J. Am. Ceram. Soc. 78*(2)*,* 445 - 448.
14. Teter, D.M. (1998). Computational Alchemy: The Search for New Superhard Materials. *Mater. Res. Soc. Bull., 23*(1)*,* 22 - 27.
15. Lundin, U., Fast, L., Nordstrom, L., Johansson, B., Wills, J. M., & Eriksson, O. (1998). Transition-metal dioxides with a bulk modulus comparable to diamond. *Phys. Rev. B, 57,* 4979 - 4982.
16. Giannozzi, P., Baroni, S., Bonini, N., Calandra, M., Car, R., Cavazzoni, C., & Wentzcovitch, R. M. (2009). QUANTUM ESPRESSO: A modular and open-source software project for quantum simulations of materials. *J. Phys: Cond. Matt., 21*(39)*,* 395502.
17. Perdew, J.P., Burke, K., & Ernzerhof, M. (1996). Generalized Gradient Approximation Made Simple. *Physical Review Letters, 77,* 3865.
18. Monkhorst, H.J., & Pack, J.D. (1976). Special points for Brillouin-zone integrations. *Phys. Rev. B, 13,* 5188 – 5192.
19. Birch, F. (1947). Finite Elastic Strain of Cubic Crystal. *Phys. Rev., 71,* 809 - 824.

20. Staple, C., Mannstadt, W., Asahi, R., & Freeman, A.J. (2001). Electronic structure and physical properties of early transition metal mononitrides: Density-functional theory LDA, GGA, and screened-exchange LDA FLAPW calculations. *Phys. Rev. B, 63(15),* 155106(1 - 11).
21. James, A.M. & Lord, M.P. (1992*). Macmillan's Chemical and Physical Data*, London: Macmillan.
22. Kaye, G.W.C. & Laby, T. H. (1993). *Tables of physical and chemical constants* (15th ed.), London: Longman.

XB_2 (X = PT, IR, PD, RH, OS) DIBORĪDU STABILITĀTE UN ELEKTRONISKĀ STRUKTŪRA

A.I. Popoola, A.Y. Odusote, O.E. Ayo-Ojo

Kopsavilkums

Rakstā veikti pirmo principu aprēķini, lai izpētītu platīna grupas metāla diborīdu strukturālās un elektroniskās īpašības stehiometriskā XB_2 (X = Pt, Ir, Pd, Rh, Os). Visi pētītie savienojumi pierādīja, ka tie pieder pie ortorombiskās *P*mmn telpiskās grupas, nevis pie *C2*/m, kas tika iepriekš noteikts dažās kompozīcijās. Saspiežamība samazinās ar bora pievienošanu Pt, Pd un Rh, bet palielinās ar bora pievienošanu Ir un Os. Stāvokļu elektroniskais blīvums parāda, ka visi savienojumi ir metāli, un PtB_2, PdB_2 un OsB_2 ir potenciāli nesaspiežami un supersmagie materiāli.

28.12.2016.

LATVIAN JOURNAL OF PHYSICS AND TECHNICAL SCIENCES
2017, N 4

DOI: 10.1515/lpts-2017-0027

APPLIED PHYSICS

INFLUENCE OF THE PREPARATION METHOD ON PLANAR PEROVSKITE $CH_3NH_3PBI_{3-X}CL_X$ SOLAR CELL PERFORMANCE AND HYSTERESIS

A. Ivanova[1,2], A. Tokmakov[3], K. Lebedeva[1],
M. Roze[2], I. Kaulachs[1]
[1]Institute of Physical Energetics
11 Krivu Str., Riga, LV-1006, LATVIA
email: kaulacs@edi.lv
[2]Riga Technical University
14/24 Paula Valdena Str., Riga, LV-1048, LATVIA
[3]LU Institute of Solid State Physics
8 Kengaraga Str., Riga LV-1063, LATVIA

Organometal halide perovskites are promising materials for low-cost, high-efficiency solar cells. The method of perovskite layer deposition and the interfacial layers play an important role in determining the efficiency of perovskite solar cells (PSCs). In the paper, we demonstrate inverted planar perovskite solar cells where perovskite layers are deposited by two-step modified interdiffusion and one-step methods. We also demonstrate how PSC parameters change by doping of charge transport layers (CTL). We used dimethylsupoxide (DMSO) as dopant for the hole transport layer (PEDOT:PSS) but for the electron transport layer [6,6]-phenyl C_{61} butyric acid methyl ester (PCBM)) we used N,N-dimethyl-N-octadecyl(3-aminopropyl)trimethoxysilyl chloride (DMOAP).

The highest main PSC parameters (*PCE, EQE,* V_{OC}) were obtained for cells prepared by the one-step method with fast crystallization and doped CTLs but higher fill factor (*FF*) and shunt resistance (R_{sh}) values were obtained for cells prepared by the two-step method with undoped CTLs.

Keywords: *inverted structure, mixed halide cells, perovskite solar cells, planar heterojunction*

1. INTRODUCTION

Solar energy continues to be a potential source of clean, abundant and sustainable energy. The photovoltaic process is considered an ideal energy process – photovoltaics convert solar energy directly to electrical energy. In recent years, great atten-

tion has been paid to organic-inorganic hybrid halide perovskite solar cells (ABX_3, $A=CH_3NH_3$, B=Pb, Sn, X=I, Cl, Br) [1]–[7]. Miyasaka and colleagues in 2009 incorporated perovskite semiconductor in solar cell and represented solar cell with power conversion efficiency (PCE) 3.8 % [8]. Then perovskite solar cell (PSC) efficiency increased rapidly to 22.1 % [9]. Apart from their high efficiency, perovskites have many other advantages, including low cost, light weight, mechanical flexibility, semi-transparency. Perovskites emerged as highly attractive sunlight convertors for their high charge carrier mobility, high absorption coefficient and long electron- and hole-diffusion lengths [6], [10]–[12].

Performance of PSCs is closely related to the morphology and chemical composition of the perovskite absorbers [13]. The most widely studied perovskites are methylammonium triiodide lead perovskite ($CH_3NH_3PbI_3$) [2]-[4] and its mixed analogue methylammonium chloride-iodide lead perovskite ($CH_3NH_3PbI_{3-x}Cl_x$) [13], [14]. The Cl^- in precursor solution can enhance crystallinity of the resulting perovskite films. The improved carrier transport has also been observed in $MAPbI_{3-x}Cl_x$ films with carrier diffusion length exceeding 1 μm, which is one order of magnitude larger than that of $MAPbI_3$ [15]. In addition, it has been mentioned for the first time by Snaith et al. that introducing trace quantity of chlorine can dramatically improve electrical properties of perovskite materials [16]. It should also be noted that in mixed halide perovskites the carrier lifetime can be prolonged substantially to ~1 microsecond [17].

There can be two types of perovskite solar cells – mesoporous cells [11], [18]–[20], where perovskites are grown on a mesoporous oxide layer, and planar cells [4], [21], [22]. However, mesoporous devices need high temperature sintering that increases the processing time and cost of solar cell. Planar devices through a simple, scalable and low-temperature technique can make perovskite solar cells commercially viable.

The planar devices can be divided into regular (n-i-p) and inverted (p-i-n) structures depending on the selective contact used on the bottom. The general solvents used for PSC*s*, such as N,N-dimethylformamide (DMF) and dimethylsulfoxide (DMSO), have very good solubility and can wash off the most of the underlayer of perovskites. Therefore, many conventional hole transporting materials (HTL) are difficult to apply in the p-i-n type PSCs. The most used HTL in inverted type cells is poly(3,4-ethylenedioxythiophene) polysterene sulphonate (PEDOT:PSS) [23], [24]. Many inorganic oxides are also widely used, such as NiO [25], NiO_x [26], VO_x [27], CuO_x [28]. Different fullerene derivatives, such as [6,6]-phenyl C_{61} butyric acid methyl ester (PCBM), are widely used as electron transporting material in inverted perovskite solar cells [1], [23], [29]. PCBM is the commonly used ETL material due to its solution processibility, appropriate energy levels for efficient exciton dissociation, and good electron transport and hole blocking properties [30].

In the present paper, we demonstrate inverted planar heterojunction perovskite solar cells where perovskite layers are formed by the two-step modified interdiffusion and one-step methods. We also investigate how PSC parameters change by doping ETL or both ETL and HTL.

2. EXPERIMENTAL PART

Devices were fabricated with the following structures:

- ITO/PEDOT:PSS/$CH_3NH_3PbI_{3-x}Cl_x$/PCBM/C_{60}/Ag (sample N1 and N2),
- ITO/PEDOT:PSS/$CH_3NH_3PbI_{3-x}Cl_x$/PCBM:DMOAP/Ag (sample N3)
- ITO/PEDOT:PSS:DMSO/$CH_3NH_3PbI_{3-x}Cl_x$/PCBM:DMOAP/Ag (sample N4).

Device structural illustration and energy diagram of the used layers are demonstrated in Fig. 1.

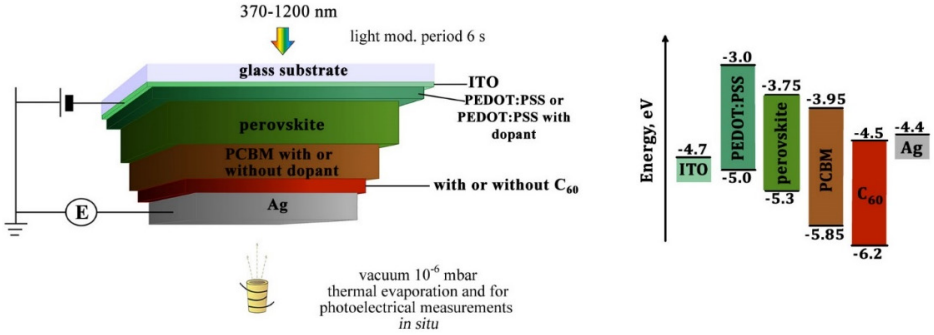

Fig. 1. Structural illustration of the studied cells and the energy level diagram of layers.

The ITO-coated glass substrates (PGO) (15 ohm/sq) were cleaned in chloroform (*Sigma Aldrich*), acetone (*Sigma Aldrich*), deionized water and isopropanol (*Sigma Aldrich*) in ultrasonic bath for 15 min in sequence and exposed to ultraviolet ozone (UVO) irradiation for 20 min. PEDOT:PSS (*Clevios Baytron AI 4083)* water solution with or without DMSO (*Sigma Aldrich*) was spin coated on ITO at a rate 5000 rpm for 60 sec at 60 °C and annealed at 145 °C for 30 min.

Then $CH_3NH_3PbI_{3-x}Cl_x$ layer was deposited by using the two methods – the two-step modified interdiffusion [31] (sample N1) and one-step [32] (samples N2, N3, N4) methods.

- Two-step modified interdiffusion method: the mixture of PbI_2 (TCI) and $PbCl_2$ (*Sigma Aldrich*) (with molar ratio 3.4) dissolved in DMF (*Sigma Aldrich*) and DMSO solvent mixture with molar ratio 3 was spin coated at a rate 6500 rpm at 65 °C for 75 s using 65 °C hot solution and was dried for 10 minutes at room temperature and for 10 minutes at 70 °C with the aim to remove remaining solvents. Methyl ammonium iodide (MAI) CH_3NH_3I (*TCI*) solution in 2-propanol (40 mg/mL) was spin coated at a rate 6000 rpm at 65 °C on top of PbI_2/$PbCl_2$ layer. The obtained bilayer system was annealed in the closed system at 100 °C for 1 h and additionally for 1 h in argon atmosphere to finish the formation of $CH_3NH_3PbI_{3-x}Cl_x$ perovskite film.
- One-step method: perovskite precursors solution in DMF was spin coated on PEDOT:PSS at a rate 6500 rpm for 60 sec at 40 °C. After a few seconds

when the spin coating process of perovskite solution was started, 200 μL anhydrous chlorobenzene (*Sigma Aldrich*) was dropped onto the centre of the substrate to induce fast crystallization [32]. The obtained film was annealed at 80 °C for 30 min and then at 100 °C for 60 min to complete the formation of $CH_3NH_3PbI_{3-x}Cl_x$ perovskite layer. After cooling down to room temperature (RT), the sample was moved into methylamine (MA) 33 wt% solution in ethanol vapours for some seconds (*Acros Organics*) to obtain smoother surface [33].

After the perovskite layer was deposited, PCBM (*Solenne*) solution in chloroform (20 mg/mL) with or without 2.5 mol% N,N-dimethyl-N-octadecyl(3-aminopropyl)trimethoxysilyl chloride (DMOAP) (*Sigma Aldrich*) was spin coated at a rate 2000 rpm for 60 sec at 40 °C and annealed at 80 °C for 30 min and then at 100 °C for 60 min. After cooling down to RT, the sample was transferred into the high vacuum chamber where C_{60} fullerene and Ag (*Kurt J. Lesker company*) electrode layers were thermally evaporated. Double fullerene layer (samples N1 and N2) was used with the aim to passivate the trap states [34]. Active cell area was 7 mm^2.

All photoelectric measurements were made in the same homemade vacuum cryostat system where C_{60} and electrode layers were thermally evaporated without breaking the vacuum and moving the cell. During the evaporation process the thickness of C_{60} and Ag electrode was controlled by a calibrated 10 MHz quartz oscillator and frequency meter. The spectral dependencies of short circuit photocurrent external quantum efficiency (EQE) were investigated in the spectral range 370–900 nm, using a synhro-detection technique and PC controlled data storage equipment [35], [36]. The samples were illuminated by chopper-modulated monochromatic light. The selected light modulation period was chosen as 6 s long and the light intensity was controlled by a calibrated Si photodiode. A constant photon flux on the sample during the measurement was achieved by a computer controlled movement of the Thorlabs linear variable optical density metallic ND filter with the correction on the Si photodiode spectral sensitivity. The dark current was checked permanently as a residual current during the end of the dark half-period of light modulation for evolution series and shunt resistances of our cells.

3. RESULTS AND DISCUSSION

Spectral dependencies of the external quantum efficiency (EQE) and optical density of photoactive layer are shown in Fig. 2. Spectral dependencies are measured at 10^{15} phot/(cm^2·s) light intensity.

EQE values grow by ~ 30 % if the preparation method of perovskite layers is changed from the two-step modified interdiffusion method to the one-step method (compare samples N1 and N2). *EQE* values grow by ~ 10 % if the electron transporting layer (ETL) PCBM is doped by DMOAP with concentration of 2.5 mol% [37]. The hydrolyzable alkoxysilane groups on DMOAP enable moisture cross-linking through the formation of stable siloxane bonds. This doped PCBM interfacial layer provides multipositive effects for the use in PSCs, including excellent film coverage on the perovskite layer, good robustness against the undersirable reaction between

the mobile iodide ions and Ag electrode, reasonable electrical conductivity, fine-tunability of WF of Ag electrode [37]. The highest *EQE* values (which exceed 90 %) can be achieved by doping both the hole transporting layer (HTL) PEDOT:PSS and ETL. DMSO as additive promotes pinhole-free perovskite layer formation. DMSO acts as a solvent of the MAPbI precursors and mediates the nucleation and crystallization at the PEDOT:PSS surface [38].

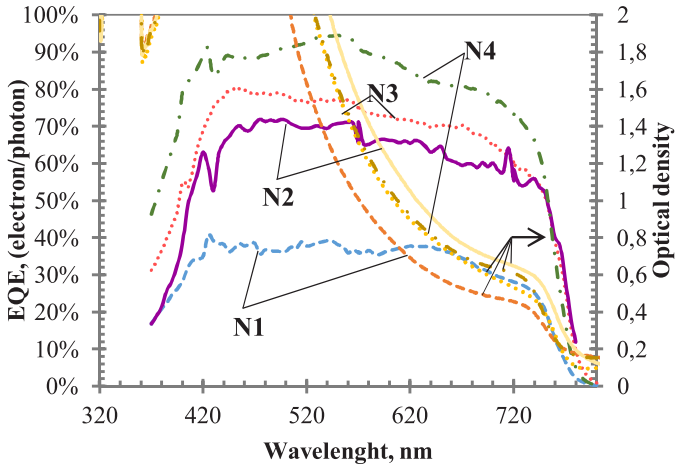

Fig 2. Spectral dependencies of the short circuit photocurrent *EQE* and optical densities of photoactive layer
(sample N1: ITO/PEDOT:PSS/perovskite (2 step method)/PCBM/C_{60}/Ag
sample N2: ITO/PEDOT:PSS/perovskite (1 step method)/PCBM/C_{60}/Ag
sample N3: ITO/PEDOT:PSS/perovskite (1 step method)/PCBM:DMOAP/Ag
sample N4: ITO/PEDOT:PSS:DMSO/perovskite (1 step method)/PCBM:DMOAP/Ag).

As it is shown in Fig. 2, samples with perovskite layers prepared by the one-step method (samples N2, N3 and N4) demonstrate higher *EQE* values than the sample with the perovskite layer prepared by the two-step modified interdiffusion method (sample N1).

The increase in *EQE* values is accompanied by the decrease in *FF* as it is shown in Fig. 3 and Table 1. Fill factor (FF) values do not exceed 0.4 for samples (N2, N3 and N4), where the perovskite layer is made by the one-step method, but for sample N1 (the perovskite layer is made by the two-step modified interdiffusion method) FF values exceed 0.58. The lowest *FF* values are observed for sample N2 (~0.3). FF values increase slightly by doping ETL (sample N3) or both *ETL* and HTL (sample N4). However, in sample N4 we observe large hysteresis, in samples N1, N2 and N3 hysteresis practically is insignificant (Fig. 3). R_{shunt} values are about an order smaller for sample N4 than in sample N2 and N3 and about two orders than in sample N1.

The highest open circuit voltage (V_{OC}) values are observed for samples where the perovskite layer is made by the one-step method (for sample N4, where both EHL and HTL are doped), V_{OC} value is 1.1 V. But for sample N1 V_{OC} value is only 0.86 V.

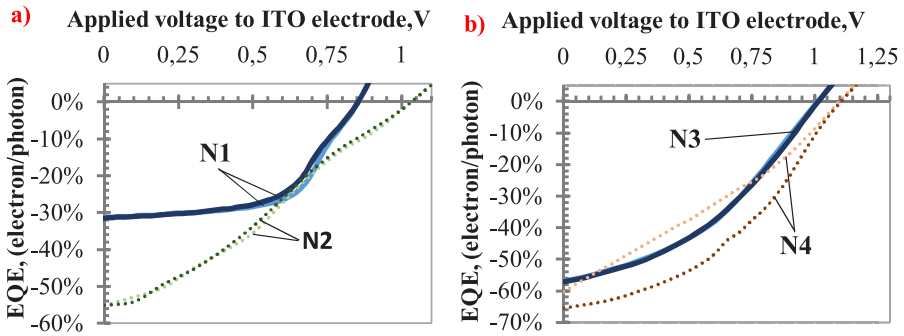

Fig. 3. Photocurrent *EQE* dependencies on the applied external voltage at 720 nm and light intensity 10^{15} phot/(cm^2·s) for:

a) samples N1 and N2;

b) samples N3 and N4.

(Lighter curves are measured at increasing voltage, darker – at decreasing voltage, "-" sign at *EQE* values denotes photocurrent direction indicating that electrons are going to upper Ag electrode.)

Table 1

Characteristics of Measured Samples at 720 nm and at Light Intensity 10^{15} phot/(cm^2·s) Obtained at Increasing Voltage (→) and Decreasing Voltage (←)

	EQE		*Voc, V*		*FF*		*PCE*	
	→	←	→	←	→	←	→	←
N1	0.279	0.282	0.856	0.859	0.583	0.534	8.10 %	7.52 %
N2	0.552	0.551	1.034	1.034	0.312	0.296	10.35 %	9.80 %
N3	0.568	0.572	1.012	1.014	0.396	0.391	13.23 %	13.16 %
N4	0.604	0.655	1.097	1.105	0.295	0.402	11.36 %	16.89 %

Table 2

Shunt and Series Resistances Measured from Residual Dark Current during Light Modulation at 720 nm and at Light Intensity 10^{15} phot/(cm^2·s) Obtained at Increasing Voltage (→) and Decreasing Voltage (←)

	R_{shunt}, Ω		R_{series}, Ω	
	→	←	→	←
N1	2.50E+07	2.38E+07	4.80E+02	4.81E+02
N2	3.46E+06	3.40E+05	5.32E+03	5.15E+03
N3	2.94E+06	3.45E+06	1.10E+03	1.11E+03
N4	3.10E+05	5.20E+05	4.34E+02	4.52E+02

The power conversion efficiency (*PCE*) is calculated according to formula 1 [35].

$$PCE = \frac{V_{OC} \cdot FF \cdot EQE}{E_{phot}}, \quad (1)$$

where V_{OC} – open circuit voltage, V;
FF – fill factor;
EQE – external quantum efficiency for short circuit photocurrent;
E_{phot} – energy of photon, eV.

PCE spectral dependencies are shown in Fig. 4. The higher *PCE* values are observed by using the one-step method for preparing the perovskite layer and they exceed 10 % even for undoped *CTLs* (Fig. 4a). When the ETL is doped, *PCE* increases to 12–14 %. If both HTL and ETL are doped, *PCE* increases up to 16–17 % (Fig. 4b), but in this case we observe very strong hysteresis (sample N4 in Fig. 4b), possibly by trap states which are formed in the layers when *ETL* and HTL are doped.

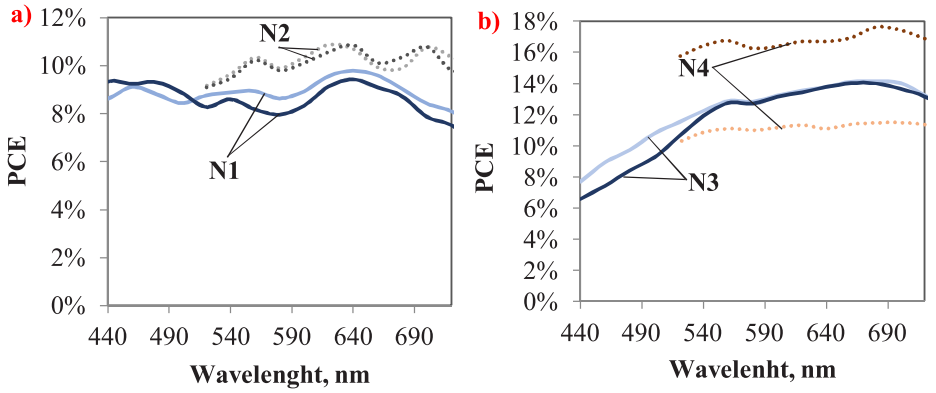

Fig. 4. Spectral dependencies of power conversion efficiency (*PCE*) at light intensity 10^{15} phot/(cm^2·s) for:
a) samples N1 and N2;
b) samples N3 and N4.
(Lighter curves are measured at increasing voltage, darker – at decreasing voltage.)

4. CONCLUSIONS

We have reported on four planar heterojunction systems, where perovskite layers are formed by using the two-step modified interdiffusion and one-step methods and where ETL or both ETL and HTL are doped. We have found that

- higher *EQE*, V_{OC} and *PCE* values are observed, when the perovskite layer is formed by using the one-step method employing fast crystallization;
- higher *FF* and R_{sh} values are observed, when the perovskite layer is formed by using the two-step modified interdiffusion method without doping *CTLs*;
- when both ETL and HTL are doped, strong hysteresis is observed in current-voltage and *PCE* spectral dependencies possibly by too high carrier trap concentration.

ACKNOWLEDGEMENTS

The present research has been supported by the State Research Programme "LATENERGI" and National Research Programme "Multifunctional Materials and Composites, Photonics and Nanotechnology (IMIS2)".

REFERENCES

1. Bretschneider, S. A., Weickert, J., Dorman, J. A., & Schmidt-Mende, L. (2014). Research update: physical and electrical characteristics of lead halide perovskites for solar cell applications. *APL Mater.*, 2(5), 40701. DOI: 10.1063/1.4871795.
2. Burschka, J., Pellet, N., Moon, S.-J., Humphry-Baker, R., Gao, P., Nazeeruddin, M. K., & Grätzel, M. (2013). Sequential deposition as a route to high-performance perovskite-sensitized solar cells. *Nature*, 499(7458), 316–320. DOI: 10.1038/nature12340.
3. Heo, J. H., Im, S. H., Noh, J. H., Mandal, T. N., Lim, C.-S., Chang, J. A., Lee, Y. H., Kim, H., Sarkar, A., Nazeeruddin, M. K., Gratzel, M., & Il Seok, S. (2013). Efficient inorganic-organic hybrid heterojunction solar cells containing perovskite compound and polymeric hole conductors. *Nat. Photonics*, 7(6), 486–491. DOI: 10.1038/nphoton.2013.80 efficient.
4. Liu, D., & Kelly, T. L. (2013). Perovskite solar cells with a planar heterojunction structure prepared using room-temperature solution processing techniques. *Nat. Photonics*, 8(2), 133–138. DOI: 10.1038/nphoton.2013.342.
5. Lotsch, B. V. (2014). New light on an old story: perovskites go solar. *Angew. Chemie - Int. Ed.*, 53(3), 635–637. DOI: 10.1002/anie.201309368.
6. Niu, G., Guo, X., & Wang, L. (2015). Review of recent progress in chemical stability of perovskite solar cells. *J. Mater. Chem. A*, 3(17), 8970–8980. DOI: 10.1039/c4ta04994b.
7. Ibn-Mohammed, T., Koh, S.C.L., Reaney, I.M, Acquaye, A., Schileo, G., Mustapha, K.B., &Greenough, R. (2017). Perovskite solar cells: an integrated hybrid lifecycle assessment and review in comparison with other photovoltaic technologies. *Renew. Sus. Energy Rev.*, 80, 1321-1344. DOI: 10.1016/j.rser.2017.05.095
8. Kojima, A., Teshima, K., Shirai, Y., & Miyasaka, T. (2009). Organometal halide perovskites as visible-light sensitizers for photovoltaic cells. *J. Am. Chem. Soc.*, 131(17), 6050–6051. DOI: 10.1021/ja809598r.
9. NREL, "Efficiency Chart," *Nrel*. p. 1, 2017.
10. Mehmood, U., Al-Ahmed, A., Afzaal, M., Al-Sulaiman, F. A., & Daud, M. (2017). Recent progress and remaining challenges in organometallic halides based perovskite solar cells. *Renew. Sustain. Energy Rev.*, 78, 1–14. DOI: 10.1016/j.rser.2017.04.105.
11. Mei, A., Li, X., Liu, L., Ku, Z., Liu, T., Rong, Y., Xu, M., Hu, M., Chen, J., Yang, Y., Grätzel, M., & Han, H. (2014). A hole-conductor–free, fully printable mesoscopic perovskite solar cell with high stability. *Science*, 345(6194), 295–298. DOI: 10.1126/science.1254763.
12. Yang, W. S., Noh, J. H., Jeon, N. J., Kim, Y. C., Ryu, S., Seo, J., & Il Seok, S. (2015). High-performance photovoltaic perovskite layers fabricated through intramolecular exchange. *Science*, 348(6240), 1234–1237. DOI: 10.1126/science.aaa9272.
13. Eperon, G. E., Burlakov, V. M., Docampo, P., Goriely, A., & Snaith, H. J. (2014). Morphological control for high performance, solution-processed planar heterojunction perovskite solar cells. *Adv. Funct. Mater.*, 24(1), 151–157. DOI: 10.1002/adfm.201302090.

14. Heo, J. H., & Im, S. H. (2016). Highly reproducible, efficient hysteresis-less $CH_3NH_3PbI_{3-x}Cl_x$ planar hybrid solar cells without requiring heat-treatment. *Nanoscale*, 8(2554–2560). DOI: 10.1039/c5nr08458j.
15. Qing, J., Chandran, H. T., Cheng, Y., Liu, K., Li, H.-W., Tsang, S. W., Lo, M.-F., & Lee, C.-S. (2015). Chlorine incorporation for enhanced performance of planar perovskite solar cell based on lead acetate precursor. *ACS Appl. Mater. Interfaces*, 7(41), 23110–23116. DOI: 10.1021/acsami.5b06819.
16. 16. Quilettes, D. W., Vorpahl, S. M., Stranks, S. D., Nagaoka, H., Eperon, G. E., Ziffer, M. E., Snaith, H. J., & Ginger, D. S. (2015). Impact of microstructure on local carrier lifetime in perovskite solar cells. *Science*, 348(6235), 683–686. DOI: 10.1126/science.aaa5333
17. Fan, L., Ding, Y., Luo, J., Shi, B., Yao, X., Wei, C., Zhang, D., Wang, G., Sheng, Y., Chen, Y., Hagfeldt, A., Zhao, Y., & Zhang, X. (2017). Elucidating the role of chlorine in perovskite solar cells. *J. Mater. Chem. A*, 5, 7423–7432. DOI: 10.1039/c7ta00973a.
18. Lee, M. M., Teuscher, J., Miyasaka, T., Murakami, T. N., & Snaith, H. J. (2012). Efficient hybrid solar cells based on meso-superstructured organometal halide perovskites. *Science*, 338(6107), 643–647. DOI: 10.1126/science.1228604 [doi].
19. Zhao, Y., Nardes, A. M., & Zhu, K. (2014). Mesoporous perovskite solar cells: material composition, charge-carrier dynamics, and device characteristics. *Faraday Discuss.*, 176, 301–312. DOI: 10.1039/c4fd00128a.
20. Di Giacomo, F., Zardetto, V., Lucarelli, G., Cinà, L., Di Carlo, A., Creatore, M., & Brown, T. M. (2016). Mesoporous perovskie solar cells and the role of nanoscale compact layers for remarkable all-round high efficiency under both indoor and outdoor illummination. *Nano Energy*, 30, 460–469. DOI: 10.1016/j.nanoen.2016.10.030.
21. Liu, M., Johnston, M. B., & Snaith, H. J. (2013). Efficient planar heterojunction perovskite solar cells by vapour deposition. *Nature*, 501, 395–398. DOI: 10.1038/nature12509.
22. Tan, H., Jain, A., Voznyy, O., Lan, X., Yuan, M., Zhang, B., Zhao, Y., Fan, F., Li, P., Quan, L. N., Zhao, Y., Lu, Z., Yang, Z., Hoogland, S., & Sargent, E. H. (2017). Efficient and stable solution-processed planar perovskite solar cells via contact passivation. *Science*, 355, 722–726. DOI: 10.1126/science.aai9081
23. Seo, J., Park, S., Kim, Y. C., Jeon, N. J., Noh, J. H., Yoon, S. C., & Il Seok, S. (2014). Benefits of very thin PCBM and LiF layers for solution-processed p-i-n perovskite solar cells. *Energy Environ. Sci.*, 7(8), 2642–2646. DOI: 10.1039/c4ee01216j.
24. Docampo, P., Ball, J. M., Darwich, M., Eperon, G. E., & Snaith, H. J. (2013). Efficient organometal trihalide perovskite planar-heterojunction solar cells on flexible polymer substrates. *Nat. Commun.*, 4, 2761. DOI: 10.1038/ncomms3761.
25. Seo, S., Park, I. J., Kim, M., Lee, S., Bae, C., Jung, H. S., Park, N. G., Kim, J. Y., & Shin, H. (2016). An ultra-thin, un-doped NiO hole transporting layer of highly efficient (16.4%) organic-inorganic hybrid perovskite solar cells. *Nanoscale*, 8(22), 11403–11412. DOI: 10.1039/c6nr01601d.
26. Yin, X., Que, M., Xing, Y., & Que, W. (2015). High efficiency hysteresis-less inverted planar heterojunction perovskite solar cells with a solution-derived NiO_x hole contact layer. *J. Mater. Chem. A*, 3(48), 24495–24503. DOI: 10.1039/c5ta08193a.
27. Xiao, M., Gao, M., Huang, F., Pascoe, A. R., Qin, T., Cheng, B., Bach, U., & Spiccia, L. (2016). Efficient perovskite solar cells employing inorganic interlayers. *ChemNanoMat*, 2(3), 182–188. DOI: 10.1002/cnma.201500223.
28. Rao, H., Ye, S., Sun, W., Yan, W., Li, Y., Peng, H., Liu, Z., Bian, Z., Li, Y.,& Huang, C. (2016). A 19.0 % efficiency achieved in CuO_x-based inverted $CH_3NH_3PbI_{3-x}Cl_x$ solar

cells by an effective Cl doping method. *Nano Energy*, 27, 51–57. DOI: 10.1016/j.nanoen.2016.06.044.

29. Li, M., Shen, P., Wang, K., Guo, T., & Chen, P. (2015). Inorganic p-type contact materials for perovskite-based solar cells. *J. Mater. Chem. A.*, 3(17), 9011–9019. DOI: 10.1039/c4ta06425a.
30. Gao, P., Gratzel, M., & Nazeeruddin, M. K. (2014). Organohalide lead perovskites for photovoltaic applications. *Energy Environ. Sci.*, 7, 2448–2463. DOI: 10.1039/c4ee00942h.
31. Xiao, Z., Bi, C., Shao, Y., Dong, Q., Wang, Q., Yuan, Y., Wang, C., Gao, Y., & Huang, J. (2014). Efficient, high yield perovskite photovoltaic devices grown by interdiffusion of solution-processed precursor stacking layers. *Energy Environ. Sci.*, 7(8), 2619. DOI: 10.1039/c4ee01138d.
32. Ye, S., Rao, H., Yan, W., Li, Y., Sun, W., Peng, H., Liu, Z., Bian, Z., Li, Y., & Huang, C. (2016). A strategy to simplify the preparation process of perovskite solar cells by co-deposition of a hole-conductor and a perovskite layer. *Adv. Mater.*, 28(43), 9648–9654. DOI: 10.1002/adma.201603850.
33. Zhou, Z., Wang, Z., Zhou, Y., Pang, S., Wang, D., Xu, H., Liu, Z., Padture, N. P., & Cui, G. (2015). Methylamine-gas-induced defect-healing behavior of $CH_3NH_3PbI_3$ thin films for perovskite solar cells. *Angew. Chemie Int. Ed.*, 54(33), 9705–9709. DOI: 10.1002/anie.201504379.
34. Wang, Q., Yuan, Y., & Huang, J. (2014). Large fill-factor bilayer iodine perovskite solar cells fabricated by a low-temperature solution-process. *Energy Environ. Sci.*, 7, 359–2365. DOI: 10.1039/c4ee00233d.
35. Kaulachs, I., Muzikante, I., Gerca, L., Shlihta, G., Shipkovs, P., Grehovs, V., Kalnachs, J., Roze, M., Rozite, G., & Ivanova, A. (2013). Electrodes for GaOHPc:PCBM/P3HT:PCBM bulk heterojunction solar cell. *Chem. Phys.*, 405, 46–51. DOI: 10.1016/j.chemphys.2012.06.007.
36. Kaulachs, I., & Silinsh, E. (1994). Molecular triplet exciton generation via optical charge transfer states in a-metalfree phthalocyanine, studied by magnetic field effects. *Latv. J. Phys. Tech. Sci.*, 5, 12–22, 1994.
37. Chang, C., Huang, W., & Chang, Y. (2016). Highly-efficient and long-term stable perovsite solar cells enabled by a cross-linkable n-doped cathode interfacial layer. *Chem. Mater.*, 28, 6305–6312. DOI: 10.1021/acs.chemmater.6b02583.
38. Kaltenbrunner, M., Adam, G., Głowacki, E. D., Drack, M., Schwödiauer, R., Leonat, L., Apaydin, D. H., Groiss, H., Scharber, M. C., White, M. S., Sariciftci, N. S., & Bauer, S. (2015). Flexible high power-per-weight perovskite solar cells with chromium oxide-metal contacts for improved stability in air. *Nat. Mater.*, 14, 1032–1039. DOI: 10.1038/nmat4388.

IZGATAVOŠANAS METODES IETEKME UZ PLĀNĀRO PEROVSKĪTA $CH_3NH_3PBI_{3-X}CL_X$ SAULES ELEMENTU PARAMETRIEM UN HISTERĒZI

A. Ivanova, A. Tokmakov, K. Ļebedeva, M. Roze, I. Kaulačs

K o p s a v i l k u m s

Organometāliskie halogenīdu perovskīti ir daudzsološs materiāls lētu augsti efektīvu saules elementu izveidei. Perovskīta slāņa uznešanas metode un starpslāņu izvēle stipri ietekmē perovskīta saules elementu efektivitāti. Šajā darbā mēs demonstrējam inversās planārās perovskīta saules šūnas, kurās perovskīta slānis tiek veidots, izmantojot modificētu interdifūzijas divpakāpju vai vienpakāpes metodes. Ka arī mēs parādam, kā perovskīta saules elementu parametri mainās atkarībā no lādiņa transportslāņu dopēšanas. Caurumu transportslānim (PEDOT:PSS) kā dopantu mēs izmantojām dimetilsulfoksīdu (DMSO), bet elektronu transportslānim ([6,6]-fenil C_{61} sviestskābes metilesterim (PCBM)) N,N-dimetil-N-oktadecil(3-aminopropil)trimetoksisilil hlorīdu (DMOAP).

Augstākas *PCE*, *EQE* un V_{OC} vērtības tika sasniegtas šūnām, kurās perovskīta slānis tika veidots, izmantojot vienpakāpes metodi ar paātrināto kristalizāciju un dopētiem lādiņa transporta slāņiem, bet augstākas *FF* un R_{sh} vērtības – šūnām, kurās perovskīta slānis veidots, izmantojot divpakāpju metodi, un ar nedopētiem lādiņa transporta slāņiem.

15.07.2017.

LATVIAN JOURNAL OF PHYSICS AND TECHNICAL SCIENCES
2017, N 4

DOI: 10.1515/lpts-2017-0028

ELECTRONICS

ANALYSIS OF CHARACTERISTICS AND REQUIREMENTS FOR 5G MOBILE COMMUNICATION SYSTEMS

G.Ancans[1], A.Stafecka[1], V.Bobrovs[1], A.Ancans[2], J.Caiko[3]
[1]Institute of Telecommunications, Riga Technical University,
[2]Department of Transport Electronics and Telematics, Riga Technical University,
12 Azenes Str., Riga, LV-1048, LATVIA
[3]Electrical Engineering and Computer Science Department, Kazakh–British Technical University,
59 Tole Bi Str., Almaty 050000, KAZAKHSTAN
guntis.ancans@rtu.lv

One of the main objectives of the fifth generation (5G) mobile communication systems, also known as IMT-2020, is to increase the current data rates up to several gigabits per second (Gbit/s) or even up to 10 Gbit/s and higher. One of the possibilities to consider is the use of higher frequencies in order to enlarge the available bandwidth. Wider bandwidth is necessary to achieve much higher data rates. It should be noted that wireless broadband transmission technologies require frequencies for their development.

The main goal of the research is to investigate the characteristics and requirements of 5G mobile communication systems. The paper provides an insight into deployment scenario and radio wave propagation in frequencies above 24 GHz of IMT-2020.

Keywords: *4G mobile communication, 5G, IMT, mobile service, M2M, radio wave propagation, WRC-19*

1. INTRODUCTION

Mobile broadband traffic is ever increasing, driven by consumer demand for mobile data, improved performance and quality of mobile networks, new technologies, devices, applications and services that introduce advanced ways of usage of mobile service frequencies [1]. In the present paper, the authors investigate the characteristics and requirements of 5G mobile communication systems, also known as IMT-2020. The paper provides an overview of possible architecture, deployment scenario and radio wave propagation in frequencies above 24 GHz.

The paper is organised as follows. The second chapter is devoted to the mobile spectrum estimation for terrestrial International Mobile Telecommunications (IMT).

The third chapter describes the main characteristics and requirements of IMT-2020. The fourth chapter is dedicated to the possible architecture and deployment scenario of IMT-2020. The fifth chapter is devoted to the radio wave propagation in frequencies above 24 GHz. In the last chapter conclusions are drawn.

2. MOBILE SPECTRUM ESTIMATE FOR IMT

It can be estimated that more spectrum resources will be necessary for the future mobile broadband communication systems to support an increasing demand for mobile data traffic. The Report ITU-R M.2290-0 [2] procures a global perspective on the future spectrum requirement approximation for terrestrial IMT in the year 2020. The total predicted spectrum demand for both low and high user density scenarios was calculated to be 1340 MHz and 1960 MHz, respectively, (embracing the spectrum already in use, or planned to be used) at least by the year 2020. The national spectrum demand in some countries can be lower than the estimate derived by lower user density settings and in some other countries national spectrum demand can be higher than the estimate derived by higher user density scenarios. Further estimates [3] expect that global IMT traffic will grow in the range of 10 to 100 times from 2020 to 2030.

To satisfy an increasing demand on mobile data traffic, especially in dense populated areas, it is necessary to develop and introduce next generation of broadband communication technologies – 5G. One of the main goals of 5G technology implementation is to increase the current data rates up to several gigabits per second (Gbit/s) or even more than 10 Gbit/s in hotspot areas. One possibility to conceive is the usage of higher frequencies in order to enlarge the available bandwidth, e.g., to get more than 500 MHz wide frequency blocks [4], which are necessary to achieve such data rate.

Within the framework of WRC-19 agenda item 1.13, in conformity with Resolution COM6/20 (WRC-15), it is planned to conceive identification of frequencies for the prospective development of IMT, including possible additional allocations to the mobile service on a primary basis [5].

3. CHARACTERISTICS AND REQUIREMENTS OF IMT-2020

A. Capabilities of IMT-2020

Goals of future 5G capability development described in Recommendation ITU-R M.2083-0 are summarised in Table 1, where the eight key capability parameters of IMT-2020 are seen [3]. Performance requirements of 5G have to be met but at the same time their execution depends on the usage scenario. The mission-critical communication demands very low latency of a few milliseconds (*ms*), though in this case the needed peak data rate may be much lower than 10–20 Gbit/s.

IMT-2020 will also conceive the Internet of Things (IoT) and M2M by connecting a wide range of smart appliances, machines and other objects without human intervention, in addition to the conventional human-to-human or human-to-machine communication.

Table 1

Capabilities of IMT-2020

Parameter	Key values for 5G
Peak data rate: maximum accomplishable data rate under ideal conditions per user/device (in Gbit/s)	10–20 Gbit/s
User experienced data rate: accomplishable data rate that is available ubiquitously in the coverage area to a mobile user/device (in Mbit/s or Gbit/s)	100 Mbit/s (for wide area coverage, e.g., in urban and sub-urban areas) and 1 Gbit/s (in hotspot cases, e.g., indoor)
Latency: the time contribution of the radio network from when the source sends a packet to when the destination receives it (in ms)	1 ms
Mobility: maximum speed at which a defined quality of service (QoS) and seamless transfer between radio nodes which may belong to different layers and/or radio access technologies can be accomplished (in km/h)	500 km/h (e.g. for high speed trains)
Connection density: total number of connected and/or accessible devices per area unit (per km^2)	10^6 devices/km^2
Energy efficiency: energy efficiency has two prospects: on the network side, energy efficiency refers to the quantity of information bits transmitted to/ received from users, per unit of energy consumption of the radio access network (in bit/Joule); on the device side, energy efficiency refers to quantity of information bits per unit of energy consumption of the communication module (in bit/Joule)	100x greater than IMT-Advanced
Spectrum efficiency: average data throughput per spectrum unit resource and per cell (bit/s/Hz)	3x greater than IMT-Advanced
Area traffic capacity: total traffic throughput served per geographic area (in Mbit/s/m^2)	10 Mbit/s/m^2

Based on the chosen use case or scenario, the importance of certain key capabilities may be significantly different, but generally all key capabilities may, to some extent, be important for most use cases. The relevance of each key capability for massive machine type communication, ultra-reliable and low latency communication, and enhanced mobile broadband usage scenarios is shown in Fig. 1 [3].

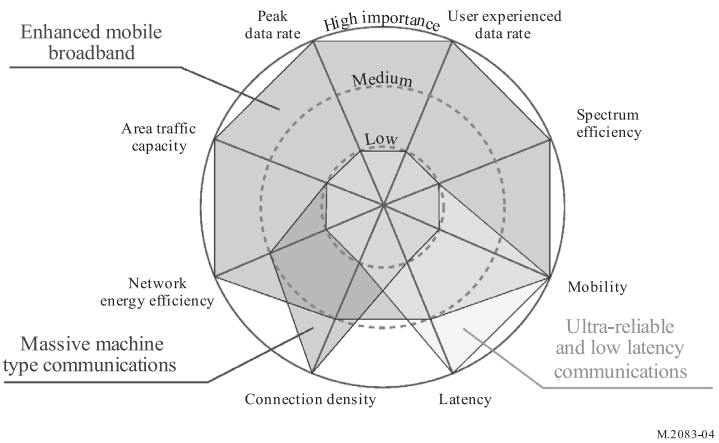

Fig.1. The relevance of key capabilities in different usage scenarios.

As a wide range of 5G requirements are defined, the single radio access configuration would not be enough to support different applications and deployment scenarios. For 5G it is planned to integrate various Radio Access Technologies (RATs) in a single system. In that way enabling a combination and cooperation of different RATs – some already existing (IEEE 802.11p etc.) and others will be designed (future releases of LTE etc.) [6].

B. Timescale for IMT-2020

To support IMT-2020 fluent development, the ITU is planning to complete work on standardisation of IMT-2020 no later than in 2020. The relevant timescale is depicted in Fig. 2 [3]. The European Commission also presented an Action Plan, mentioning plans for commercial 5G launch in 2020 and plans for joint work with industry and the Member States to identify and allocate spectrum for 5G, and organise pan-European 5G trials in 2018 [7]. It is important to specify the exact time when the standards are completed and when deployment may start, when discussing the timelines for IMT-2020.

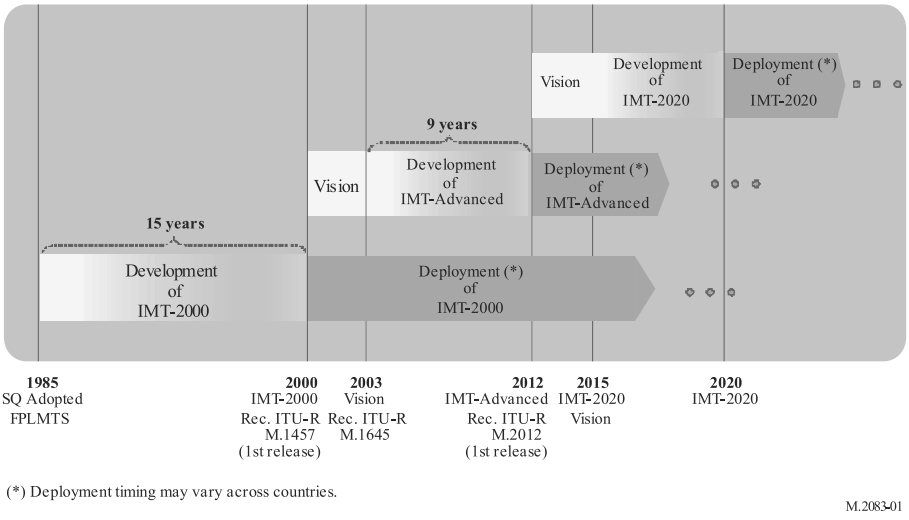

Fig. 2. Overview of timescale for IMT development and deployment.

In the authors' opinion, the 5G signal waveform could be improved, as a result, reducing the unwanted emissions, improving the coexistence in adjacent bands or channels and minimising the requirement for guard bands.

4. ARCHITECTURE AND DEPLOYMENT SCENARIO

According to Ericsson paper [8], LTE will explicate in a way of providing coverage for mobile users. 5G networks will comprise LTE access based on Orthogonal Frequency Division Multiplexing (OFDM) along with new radio interfaces using possibly new techniques, e.g., Filter Bank Multicarrier Transmission technique (FBMC).

A. Architecture of IMT-2020

Deployment architecture of IMT-2020 can be classified into two architecture types: standalone or overlay. The standalone architecture pertains to the network deployment consisting of millimeter wave (mmWave) small cells. The overlay architecture pertains to the network deployment of millimeter wave small cells developed on top of the existing macro networks. In overlay architecture case, the macro cell layer of the existing 4G mobile communication serves mainly for providing coverage, whereas the millimeter wave small cell layer should be used to provide capacity [4].

For mmWave small cells developed using cellular technologies, the typical range is expected to be around 10 m to 200 m under Non-Line-of-Sight (NLoS) circumstances, which is a lot shorter than the range of a cellular macro cell that can be several kilometres wide. Small cells can be deployed both indoors (e.g., femto cells) and outdoors. When deployed outdoors, mmWave small cells are typically deployed at a lower antenna height than a macro cell (on street lamp posts etc.) and with lower transmit power to cover a targeted area. Three categories of mmWave small cell deployment scenarios can be identified: indoor, hotspot, and outdoor [4].

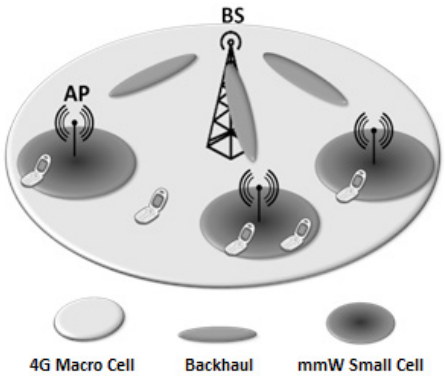

Fig. 3. System architecture proposed for 5G.

The possible system architecture intended for 5G is presented in Fig. 3 [4]. It relies on macro cellular base stations, which provide wide area coverage to mobile users using the existing RATs (e.g., LTE, UMTS) and their enhancements below 6 GHz. The reference system architecture introduces millimeter wave small cells that enable much higher throughput and traffic capacity to low mobility users employing millimeter wave radio access in the frequency bands above 24 GHz.

B. Channel Bandwidth

Maximum capacity of a radio channel for single-input single-output (SISO) scenario can be described by Shannon-Hartley formula. This equation relates the maximum capacity (transmission bit rate) that can be achieved over a given channel to certain noise characteristics and bandwidth. For an *additive white Gaussian noise* of power N the maximum capacity can be calculated by

$$C = B \cdot \log_2\left(1 + \frac{S}{N}\right), \tag{1}$$

where C – the maximum capacity of the channel (bits/s) otherwise known as *Shannon's capacity limit for the given channel*; B – the bandwidth of the channel (Hz);

S – the signal power (W); N – the noise power (W). The ratio S/N is named *Signal to Noise Ratio* (SNR) [9].

It can be recognised that the maximum transmission rate, at which the information can be transmitted without any error, is limited by the bandwidth, the signal level, and the noise level. As the bandwidth B tends to infinity, noise power also increases with the increase in bandwidth that is why the channel capacity does not become infinite.

Therefore, the authors assume that bandwidth directly affects channel throughput. For example, in LTE systems different channel bandwidths have a different number of resource blocks (*RB*) used for data transmission, some part of a channel bandwidth is also used for guard bands. It can be concluded that the wider available bandwidth, the higher channel throughput.

One of the benefits of higher frequency adaptation for mobile communications is system capability to implement wide channels. For Frequency Division Duplex (FDD) implementation, a duplex filter is needed. The current development has achieved maximum size of duplex filter to be around 3–4 % of the centre frequency of the frequency band. For better understanding, an example can be given. If the centre frequency is 12.5 GHz, a duplex filter for channel bandwidth of 500 MHz can be used. To cover bandwidth of one 1120 MHz channel or two 500 MHz channels, a duplex filter at 28 GHz can be chosen. In case the centre frequency (*Fc*) × 0.03~0.04 is smaller than the necessary channel bandwidth for specific data rate provision, carrier aggregation is needed to achieve the data rate as shown in Fig. 4 and Fig. 5 [4].

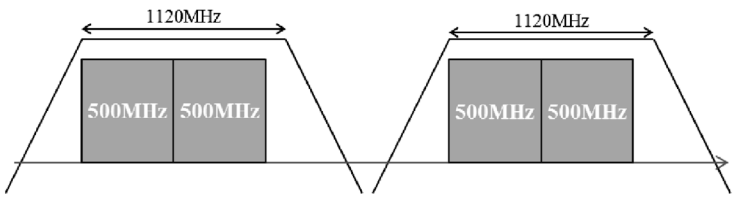

Fig. 4. The number of duplex filters to cover bandwidth to meet the needed data rate in 28 GHz band.

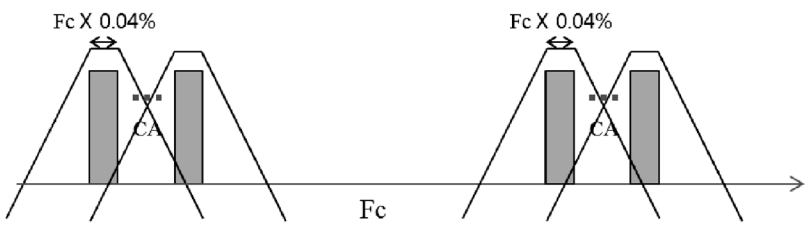

Fig. 5. The number of duplex filters to cover bandwidth to meet the required data rate. F_c where F_c x 0.03~0.04 is less than channel bandwidth to meet the needed data rate.

In the authors' opinion, to achieve objectives set for future IMT-2020 systems, it is necessary to provide contiguous, broad and harmonised frequency bands, which will minimize 5G device complexity and possible interference issues.

5. RADIO WAVE PROPAGATION IN FREQUENCIES ABOVE 24 GHZ

A. Propagation Losses

For outdoor access mobile communications in frequencies above 24 GHz, one of the expected challenges to overcome will be difficulties in propagation conditions. The most evident obstacle is the high path loss of the bands above 24 GHz compared to frequency bands below 6 GHz for traditional cellular use. The Free-Space path loss (Recommendation ITU-R P.525) [10] provides the expected loss (dB) that can be calculated by

$$L_p = 92.4 + 20 \cdot \log f + 20 \cdot \log d, \tag{2}$$

where d – distance between a transmitter and a receiver (km); f – frequency (GHz).

An example can be provided to describe one of the difficulties following higher path loss. In the frequency range from 2 GHz to 28 GHz and 70 GHz additional losses of 22.9 dB and 30.9 dB, respectively, can be anticipated to occur. To compensate these losses, additional means should be taken. For example, one possible way to compensate these losses is to use larger antenna array sizes with higher antenna power gain that uses Multiple-Input Multiple-Output (MIMO) technologies [4].

B. Atmospheric Losses

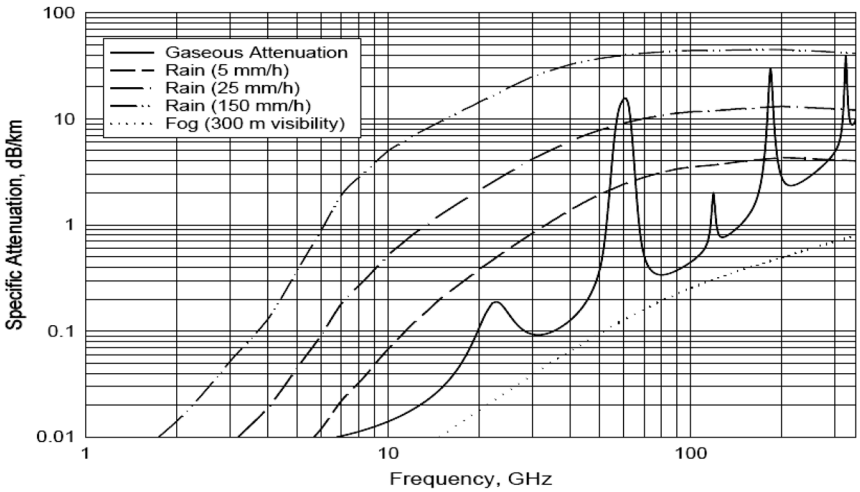

Fig. 6. Atmospheric attenuation versus frequency.

Environmental effects, e.g., gaseous (oxygen and water vapour) absorption, rain loss and foliage loss introduce some other challenges to overcome. Only in rare cases path losses that are caused by snow or fog are significant, in most cases they are only minor challenges. According to ITU-R Recommendation P.837 [11], gas loss is ubiquitous, and as for the rain attenuation, it only occurs for a short period of time. Frequencies that are represented by the peaks in Fig. 6 [4] are the ones most sensible to molecular oxygen and water vapour losses, and following these frequencies should be used where influence of atmospheric attenuation is not significant, e.g., for small cells for indoor usage. In these peak frequency ranges, the reach of interfering signals is also limited by connatural atmospheric loss, allowing for more frequent reuse of carrier frequencies.

C. Antenna Technology

Designing antennas that can operate well enough in distant frequencies at the same time, e.g., both at 700 MHz and 60 GHz is a difficult task; therefore, most likely two separate antennas, each operating at the specific frequency band, will be required. The wavelengths above 24 GHz provide a possibility to put more antenna elements in the restricted area. The antenna technology with the increased number of particular antenna elements can be used to provide high beamforming gain; thus, the incremented path loss of above 24 GHz frequency bands can be mitigated by beamforming techniques with exact pointing direction. The phased array beamforming is used to raise the received signal power by using beamforming gain. Applying narrower beams, greater antenna gains may be achieved [4].

Noticeable advantage of millimeter wave systems above 24 GHz is small size of required antennas, which can be arranged in comparatively small footprint phased arrays for high directivity and beam steering. For 5G communication systems, massive MIMO solutions would be used to compensate additional propagation loss in higher frequencies [12]. Array antennas should be integrated in the terminals or user equipment. In this case, it should be possible since the transmission wavelengths would become smaller. The millimeter wave small cell deployment with much wider bandwidth accessible can provide higher data throughput than the existing macro cell networks.

6. CONCLUSIONS

In the paper, the authors have investigated characteristics and requirements of 5G mobile communication systems. An insight into 5G system deployment architecture and scenario, radio wave propagation in frequencies above 24 GHz of IMT-2020 has also been provided in the paper.

The analysis shows that one of the ways of future IMT-2020 development would be the usage of overlay network architecture, when use of low frequencies below 6 GHz and high frequencies above 24 GHz is coordinated in a complementary manner. In this case, macro cells operating in frequency bands below 6 GHz provide baseline coverage, and capacity improvements are ensured by additional network elements that are to be developed, operating in higher frequency bands above 24 GHz.

The results of the present study have shown that implementation of high frequency bands, even above 24 GHz, remains necessary to ensure that all the performance targets of 5G, e.g., multigigabit per second data rates, are met. Frequencies below 6 GHz are very valuable, especially frequencies below 1 GHz due to their optimal radio wave propagation. IMT technologies produced for deployment in frequency bands above 24 GHz would be rational to use mainly in dense urban environments enabling provision of high data rate services. In the authors' opinion, for the deliberative development of IMT systems it is necessary to timely provide wide and contiguous spectrum resources for implementation of new technologies and services.

The results obtained within the framework of the research can be used by National Regulatory Authorities (NRAs), equipment manufacturers, mobile operators, researchers and other interested parties when planning 4G and 5G mobile services.

REFERENCES

1. Ancans, G., Bobrovs, V., & Ivanovs, G. (2013). Spectrum usage in mobile broadband communication systems. *Latvian Journal of Physics and Technical Sciences*, *50*(3), 49–58.
2. Report ITU-R M.2290-0. (2013). *Future Spectrum Requirements Estimate for Terrestrial IMT*. International Telecommunications Union. Available at http://www.itu.int/dms_pub/itu-r/opb/rep/R-REP-M.2290-2014-PDF-E.pdf.
3. Recommendation ITU-R M.2083-0. (2015). *IMT Vision – Framework and Overall Objectives of the Future Development of IMT for 2020 and Beyond*. International Telecommunications Union. Available at https://www.itu.int/dms_pubrec/itu-r/rec/m/R-REC-M.2083-0-201509-I!!PDF-E.pdf.
4. Report ITU-R M.2376-0. (2015). *Technical Feasibility of IMT in Bands above 6 GHz*. International Telecommunications Union. Available at https://www.itu.int/dms_pub/itu-r/opb/rep/R-REP-M.2376-2015-PDF-E.pdf.
5. Resolution COM6/20 (WRC-15). (2015). *Studies on Frequency-related Matters for International Mobile Telecommunications Identification Including Possible Additional Allocations to the Mobile Services on a Primary Basis in Portion(s) of the Frequency Range between 24.25 and 86 GHz for the Future Development of International Mobile Telecommunications for 2020 and beyond*. International Telecommunications Union. Switzerland, Geneva.
6. *5G Automotive Vision*. (2015). Available at https://5g-ppp.eu/wp-content/uploads/2014/02/5G-PPP-White-Paper-on-Automotive-Vertical-Sectors.pdf.
7. European Commission. (2016). *State of the Union 2016: Commission Paves the Way for More and Better Internet Connectivity for All Citizens and Businesses. An Action Plan for 5G*. Strasbourg. Available at http://europa.eu/rapid/press-release_IP-16-3008_en.htm.
8. Ericsson. (2016). *5G Radio Access*. White paper. Available at https://www.ericsson.com/res/docs/whitepapers/wp-5g.pdf.
9. Saunders, S.R., & Zavala, A.A. (2007). *Antennas and Propagation for Wireless Communication Systems* (2nd ed.). John Wiley & Sons Ltd.
10. Recommendation ITU-R P.525-2. (1994). *Calculation of Free-Space Attenuation*. International Telecommunications Union. Available at https://www.itu.int/dms_pubrec/itu-r/rec/p/R-REC-P.525-2-199408-I!!PDF-E.pdf.

11. Recommendation ITU-R P.837-6. (2012). *Characteristics of Precipitation for Propagation Modelling*. International Telecommunications Union. Available at https://www.itu.int/rec/R-REC-P.837-6-201202-I/en.
12. Ancans, G., Bobrovs, V., Ancans, A., & Kalibatiene, D. (2016). Spectrum considerations for 5G mobile communication systems. *Procedia Computer Science*, *104*, 509–516.

5G MOBILO SAKARU SISTĒMU PRASĪBU UN RAKSTURĪGO PARAMETRU ANALĪZE

G.Ancāns, A.Stafecka, V.Bobrovs, A.Ancāns, J.Čaiko

K o p s a v i l k u m s

Viens no piektās paaudzes (5G) mobilo sakaru sistēmu, zināmu arī kā IMT-2020, galvenajiem mērķiem ir palielināt datu pārraides ātrumus līdz vairākiem gigabitiem sekundē (Gbit/s) un pat virs 10 Gbit/s. Lielākus datu pārraides ātrumus var sasniegt, izmantojot radiokanālus ar lielāku frekvenču joslas platumu. Nākamās paaudzes mobilo sakaru sistēmu izmantošana ar platākiem radiokanāliem iespējama augstākās frekvenču joslās. Platjoslas bezvadu pārraides sistēmu attīstībai ir nepieciešami papildu radiofrekvenču spektra resursi.

Pētījuma mērķis ir apskatīt IMT-2020 sistēmu galvenās prasības un to raksturīgākos parametrus. Rakstā apskatīts arī IMT-2020 sistēmu iespējamais izmantošanas scenārijs, kā arī analizēta radioviļņu izplatīšanās virs 24 GHz.

20.04.2017.